NUREG/CR-3262
PNL-4710
Vol. 1

COBRA-NC: A Thermal-Hydraulic Code for Transient Analysis of Nuclear Reactor Components

Equations and Constitutive Models

Prepared by C. L. Wheeler, M. J. Thurgood, T. E. Guidotti, D. E. DeBellis

Pacific Northwest Laboratory
Operated by
Battelle Memorial Institute

Prepared for
U.S. Nuclear Regulatory Commission

NUREG/CR-3262
PNL-4710
Vol. 1
R4

COBRA-NC: A Thermal-Hydraulic Code for Transient Analysis of Nuclear Reactor Components

Equations and Constitutive Models

Manuscript Completed: March 1986
Date Published: May 1986

Prepared by
C. L. Wheeler, M. J. Thurgood, T. E. Guidotti, D. E. DeBellis

Pacific Northwest Laboratory
Richland, WA 99352

Prepared for
Division of Accident Evaluation
Office of Nuclear Regulatory Research
U.S. Nuclear Regulatory Commission
Washington, D.C. 20555
NRC FIN B2466

ABSTRACT

COBRA-NC is a digital computer program written in FORTRAN IV that simulates the response of nuclear reactor components and systems to thermal-hydraulic transients. The code solves the multicomponent, compressible, three-dimensional, two-fluid, three-field equations for two-phase flow. The three velocity fields are the vapor/gas field, the continuous liquid field, and the liquid drop field. The code has been used to model flow and heat transfer within the reactor core, the reactor vessel, the steam generators, and in the nuclear containment. The conservation equations, equations of state, and physical models that are common to all applications are presented in this volume of the code documentation.

CONTENTS

1.0 INTRODUCTION 1

2.0 CONSERVATION EQUATIONS FOR THE THREE-FIELD MODEL OF TWO-PHASE FLOW 4

2.1 Two-Fluid Phasic Conservation Equations 5

2.2 Three-Field Conservation Equations 7

2.2.1 Three-Field Model Notation 7

2.2.2 Three-Field Model Assumptions 9

2.2.3 Three-Field Equations 11

2.3 Three-Field Conservation Equations in Component Form 14

2.3.1 Cartesian Coordinates 15

2.3.2 Subchannel Coordinates 16

2.3.3 Comparison of Cartesian and Subchannel Equations . . . 18

2.4 Lumped Parameter Equations 20

3.0 PHYSICAL MODELS 23

3.1 Computational Cell Structure 23

3.2 Flow Regime Selection 23

3.2.1 Normal Flow Regimes 25

3.2.2 Hot Wall Flow Regimes 30

3.3 Interfacial Mass Transfer 33

3.4 Interfacial Drag Force 41

3.5 Wall Drag Force 47

3.6 Viscous Stress and Turbulence Models 49

3.7 Entrainment Rate 53

3.7.1 Entrainment in Film Flow 53

3.7.2 De-Entrainment in Film Flow 56

3.7.3 Entrainment During Reflood 56
3.7.5 De-Entrainment on Structure 58
3.7.6 De-Entrainment at Area Changes 59
3.7.7 De-Entrainment on Solid Surfaces and Liquid Pools . . . 59
3.8 Fluid Thermodynamic Properties 59
3.8.1 Steam/Gas Transport Properties 59
3.8.2 Thermodynamic Properties 65
4.0 HEAT TRANSFER MODELS 77
4.1 Conduction Models 77
4.1.1 Conductor Geometry 77
4.1.2 Unheated Conductor Model 80
4.1.3 Conduction Equation 80
4.2 Heat Transfer Package 86
4.2.1 Single-Phase Vapor 86
4.2.2 Single-Phase Liquid 89
4.2.3 Nucleate Boiling 90
4.2.4 Subcooled Nucleate Boiling 92
4.2.5 Critical Heat Flux and Transition Boiling Regime . . . 96
4.2.6 Dispersed Flow and Inverted Annular Film Boiling . . . 101
4.3 Quench Front Model 104
4.4 Gap Conductance Model 107
4.4.1 Radiant Heat Transfer 109
4.4.2 Conduction Heat Transfer in the Fill Gas 109
4.4.3 Fuel/Cladding Contact Conductance 113
4.4.4 Deformation Model 114

4.5 Cladding Oxidation Model 123

5.0 REFERENCES 129

FIGURES

1 Control volume for Cartesian coordinates 18
2 Mass/energy cell 24
3 Vertical and transverse momentum cells 24
4 Normal two-phase flow regimes 26
5 Normal flow regime selection logic 26
6 Hot wall flow regimes 32
7 Hot wall flow regime selection logic 32
8 Single-bubble drag coefficient 43
9 Nuclear fuel rod geometry 78
10 Heater rod geometry (example of a fuel pin simulator) 79
11 Tube and wall conductor geometries 79
12 Heat balance control volume 81
13 Conduction node positioning 82
14 Schematic representation of the boiling curve 87
15 Heat transfer regime selection logic 87
16 Reynolds number factor, F, for Chen correlation 93
17 Suppression factor, S, for Chen correlation 93
18 Schematic of CHF regime selection logic 96
19 Example of COBRA-TF axial noding scheme 106
20 Example of node insertion 106
21 Fine mesh renoding: cladding temperature profile 108
22 Fine mesh renoding: surface heat flux 108
23 Temperature jump distances for an ideal gap 111
24 Illustration of fuel relocation 122

TABLES

1 Interfacial Heat Transfer Coefficients 34

2 Interfacial Heat Transfer Area Per Unit Volume 37

3 Lennard-Jones Force Constants 62

ACKNOWLEDGMENTS

COBRA-NC is the result of the efforts of a number of people. We wish to acknowledge the main contributors and to express our appreciation to those who have offered their advice and suggestions.

The main contributors to the program are listed below.

Fluid Dynamics:	M. J. Thurgood, T. L. George, and T. E. Guidotti
Heat Transfer:	J. M. Kelly and R. J. Kohrt
Turbulence Model:	K. R. Crowell
Graphics and Programming:	A. S. Koontz
Simulations:	D. E. DeBellis

We wish to thank Dr. T. Lee and Dr. R. Lee of the U.S. Nuclear Regulatory Commission for their patience, support, and suggestions during this large undertaking. We also wish to thank Drs. Tong, Shotkin, Han, and Zuber of the U.S. Nuclear Regulatory Commission and members of the Advanced Code Review Group for their many helpful suggestions. We also express our gratitude to our manager, Dr. D. S. Trent, for his support, and Cathy Darby for typing this report.

NOMENCLATURE

A	flow area
A_H	heat transfer surface area
A_I	intercell friction area
A_I'''	interfacial area per unit volume
A_K	transverse flow area
a	absorption coefficient
b	phase mobility
C_D	drag coefficient
C_p	specific heat capacity
$\underline{\underline{D}}$	deformation tensor
$\underline{\underline{D}}^*$	deleted deformation tensor
D_H	hydraulic diameter
$\underline{\underline{F}}$	turbulence anisotropy tensor
$\underline{F}_I$	intercell drag force
F	gray body factor
f	friction factor
G	mass flux
g_c	gravitational conversion constant
g	gravitational acceleration
$\underline{g}$	gravitational acceleration vector
H	heat transfer coefficient
h	enthalpy
h_{fg}	enthalpy of vaporization
j	superficial velocity
K	loss coefficient
K_I	interfacial friction coefficient
k	thermal conductivity
k_s	equivalent sand roughness
k_σ	mass transfer coefficient
L	transverse coordinate

ℓ_h energy mixing length

ℓ_m momentum mixing length

M^d interfacial drag force

M_i mass of heat transfer node i

M^Γ interfacial momentum exchange due to mass transfer

$\dot{m}$ mass flow rate

N number density

N_μ viscosity number

P pressure

P^T turbulent pressure

Pr Prandtl number

Pr^t turbulent Prandtl number

P_w wetted perimeter

Q conduction heat flux

Q'''_w wall heat flux per unit fluid volume

q fluid-fluid conduction heat flux

q" surface heat flux

q_I''' interfacial heat flux per unit volume

q^T turbulent heat flux

R internode resistance

Re Reynolds number

r radius

S source

S net rate of entrainment

S_{DE} rate of de-entrainment

S_E rate of entrainment

S_k gap width of gap k

S_u entrainment correlation parameter

S_Γ rate of interfacial area concentration change due to phase change

S'_{nk} orthogonal gap width

S''' net rate of entrainment per unit volume

$(S'''\underline{U})$ momentum exchange due to entrainment

T temperature

$\underline{\underline{I}}$ stress tensor

$\underline{\underline{I}}^T$ Reynolds stress tensor

t time

Δt averaging time interval

$\underline{U}$ fluid velocity

$\underline{U}_{vj}$ drift velocity

u velocity component in vertical (x) direction

V volume

v velocity component in transverse (y) direction

We Weber number

w velocity component in transverse (z) direction

x vertical direction

y transverse direction

z transverse direction

Greek Symbols

α void fraction

β thermal expansion coefficient

Γ net rate of mass transfer per unit volume

Γ''' net rate of vapor generation per unit volume

$(\Gamma'''\underline{U})$ momentum exchange due to vapor generation

δ film thickness

δ_{ij} Kronecker delta

ϵ_T thermal diffusivity

ϵ turbulent thermal diffusivity

ϵ_D turbulent mass diffusivity

η fraction of vapor generation coming from entrained liquid

η_{NR} de-entrainment efficiency

μ_T viscosity

μ turbulent viscosity

ρ	density
$\underline{\underline{g}}$	fluid-fluid stress tensor
σ	surface tension
$\underline{\underline{\tau}}$	viscous stress tensor (stress deviator)
$\underline{\tau}_I'''$	interfacial drag force per unit volume
λ	characteristic wavelength
σ_β	Boltzman constant

Subscripts

B	bulk
BR	bubble rise
b	bubble
CHF	critical heat flux
ce	droplet mass source
cg	noncondensable gas mass source
cℓ	continuous liquid mass source
cv	vapor mass source
DE	de-entrainment
d	drop
E	entrainment
e	entrained field
eℓ	drop/liquid energy source
ev	vapor/gas mixture energy source
f	saturated liquid film
g	saturated vapor
I	interfacial
i, j	heat transfer nodes

k phase k

ℓ liquid field

MIN minimum film boiling point

m mixture

me drop momentum source

mℓ liquid momentum source

mv vapor/gas mixture momentum source

mg noncondensable gas mixture

R relative

SHL superheated liquid

SCL subcooled liquid

SHV superheated vapor

SCV subcooled vapor

SP single phase

S surface

s drop formation

V vapor phase (Vapor properties used in heat transfer correlations are evaluated at the film temperature.)

v vapor field

vg vapor/gas mixture

vℓ between vapor and liquid fields

ve between vapor and entrained fields

W-D wall to drop

W-V wall to vapor

x, y, z directions

2ϕ two phase

Superscripts

i interfacial surface average

n old time level

n+1 new time level

s surface average

T turbulent

t transpose

SUMMARY

COBRA-NC is a digital thermal-hydraulic computer program that simulates the response of nuclear reactor components and systems to loss-of-coolant accidents. It utilizes a multicomponent, two-fluid, three-field representation of two-phase flow. Conservation equations are solved for water and its vapor, and for a noncondensable gas mixture comprised of n species. The flow field may be modeled using a lumped parameter approach or a multidimensional finite-difference approach.

This volume contains a description of the conservation equations, equations of state, and physical models that are solved in the code to describe the flow of heat and fluid through reactor components. The code is capable of simulating single- or two-phase flows within a variety of geometries. It has been used to model reactor fuel bundles, cores, vessels, steam generators, and various types of nuclear containments. Therefore, it has heat transfer models for nuclear of nuclear containments. Therefore, it has heat transfer models for nuclear fuel rods as well as unheated structures, and has a flexible mesh so that various geometries may be easily treated from input. It has been used to model such diverse phenomena as blowdown and reflood in the primary system and steam/water blowdown and hydrogen distribution in nuclear containments.

COBRA-NC: A THERMAL-HYDRAULIC CODE FOR TRANSIENT ANALYSIS OF NUCLEAR REACTOR COMPONENTS

VOLUME 1: EQUATIONS AND CONSTITUTIVE MODELS

1.0 INTRODUCTION

The COBRA-NC computer code has been developed by the Pacific Northwest Laboratory for the United States Nuclear Regulatory Commission. The Pacific Northwest Laboratory is operated for the Department of Energy by Battelle Memorial Institute.

COBRA-NC has been developed to perform analyses of thermal-hydraulic transients in various components of light water reactors including the reactor core, reactor vessel, steam generators, and the reactor containment building. It has also been merged with a system code to provide a primary coolant system analysis capability (Ref. 1). The documentation for the code is subdivided up into several volumes because of its wide range of application. Volume 1, Equations and Constitutive Models, contains a description of the basic conservation equations and constitutive models used in the code. Volume 2 contains the finite-difference equations and a description of the procedures used for their numerical solution. Volumes 3 through 5 are the Users' Manuals. They contain line-by-line input instructions for COBRA-NC and user guidance for application of the code. Volume 3 is the Users' Manual for General Two-Phase Thermal Hydraulics. This volume contains an explanation for all of the input data required for general application of the code. Volume 4 is the Users' Manual for Containment Analysis. This volume contains an explanation of the input data required for containment analysis only. It also provides examples of containment modeling procedures. Volume 5 is the Users' Manual for Flow Blockage and Hot Bundle Analysis and describes the input required for performing such analysis.

Volumes 6, 7, and 8 are the Assessment Manuals. They contain the results of simulations run to assess the performance of the code in each of the areas discussed above. Volume 9 is the Programmers' Manual. It explains the details of COBRA-NC's working parts from a programmer's viewpoint. The structure of the code is described, as are the major variables and subroutines used in the code.

The COBRA-NC code provides a two-component, two-fluid, three-field representation of two-phase flow. It is a two-component model to allow the modeling of water and its vapor as well as a noncondensable gas mixture. The gas mixture may consist of any number of gas species. The properties of eight gases are currently coded.

Three momentum, four mass, and two energy equations are solved for the fluid. Momentum equations are solved for the vapor-gas mixture, the continuous liquid and the liquid-drop fields. Thus, each of these may travel at different velocities. A liquid film flowing down walls with vapor flowing across it

can be modeled. The vapor may also contain drops that travel at yet a different velocity than the vapor.

Mass equations are solved for the noncondensable gas, the vapor, the continuous liquid, and the liquid drops. Thus, the mass of each phase can be accounted for. In addition, a mass-transport equation is solved for each species of the noncondensable gas mixture, so that the concentration of each species can be determined. Energy equations are solved for the vapor-gas mixture and for the continuous liquid- drop mixture. It is therefore assumed that both the vapor and gas in a given computational cell will have the same temperature, and that the liquid film and liquid drops within a given mesh cell will be at the same temperature. These two mixtures, however, can have different temperatures. This model permits the modeling of nonsaturated air (air with a relative humidity of less than 100%), superheated vapor in the presence of subcooled liquid, and liquid superheating.

The code is a three-dimensional, compressible-flow, finite-difference code formulated in Cartesian coordinates. However, it features an extremely flexible noding scheme that allows it to be run in a lumped parameter, one-dimensional, two-dimensional, or three-dimensional mode. It has a finite-difference slab conduction model for structural heat transfer. Any number of materials may be used in each slab, and the number of heat transfer nodes through the thickness of the slab may be specified by the user.

A rod model designed to calculate the heat transfer for nuclear fuel rods, heater rods, and heated tubes and walls is also included. The nuclear fuel rod requires minimal user input. Material properties for zirconium clad and uranium dioxide fuel are assumed as the default values. A dynamic gap conductance model based on the GAPCON and FRAP computer codes is available for use with the nuclear fuel rod model. The Baker-Just and Cathcart cladding oxidation models are available as options. These models are used to calculate the heat and hydrogen sources and the steam sink resulting from the metal/water reaction.

A mixing-length turbulence model has also been included to allow the user to model turbulent shear flows and the turbulent diffusion of gas species due to concentration gradients. A general set of boundary conditions has been included to allow flow or pressure and enthalpy to be specified anywhere on the computational mesh.

This volume, Equations and Constitutive Models, describes the conservation equations and physical models solved in the code that are basic to all of the applications of the code. The constitutive relations in COBRA-NC include state-of-the-art physical models for the interfacial mass transfer, the interfacial drag forces, the liquid and vapor wall drag, the wall and interfacial heat transfer, the rate of entrainment and de-entrainment, fuel rod cladding oxidation heat and hydrogen sources, dynamic gap conductance, and the equations of state for water and for a steam and noncondensable gas mixture. In addition, a mixing length turbulence model has been included as an option. Section 2 presents the two-component, two-fluid phasic conservation

equations and their extension to the three-field model. The physical models used in the hydrodynamic solution are discussed in Section 3. The physical models for the heat transfer solution are given in Section 4. Appendix A to this volume provides the derivation of the two-fluid phasic conservation equations. Appendix B lists the nuclear material properties used by the nuclear rod model. Appendix C describes the logic for calculating thermal connectors for the conduction solution in the heat transfer model.

2.0 CONSERVATION EQUATIONS FOR THE THREE-FIELD MODEL OF TWO-PHASE FLOW

Multiphase flows consist of two or more fluids separated by moving phase interfaces. Material properties are assumed to change discontinuously across these interfaces. In general, the phases present can be any combination of liquid, solid, or gas. The flow pattern can take any one of a wide variety of forms, such as bubbly flow, droplet flow, gas-particle flow, and stratified flow. Exact conservation equations can be derived for each phase, and jump conditions relating variables on each side of the phase interface can be formulated, much as in single-phase shock wave theory. With appropriate initial and boundary conditions, these equations could theoretically be solved for the exact motion of each phase and the phase interfaces. Except in a few simple cases, however, an exact analysis of multiphase flow is impossible because of its complex and essentially chaotic nature. Fortunately, one is generally not interested in the exact motion of each droplet or bubble but, instead, wants to learn something about the average behavior of each phase. Thus, most work in multiphase flow is done with some kind of average equations.

The average conservation equations used in COBRA-NC are derived following the methods of Ishii (Ref. 2). The average used is a simple Eulerian time average over a time interval, assumed to be long enough to smooth out the random fluctuations present in a multiphase flow but short enough to preserve any gross unsteadiness in the flow. The resulting average equations can be cast in either the mixture form or the two-fluid form. Because of its greater physical appeal and broader range of application, the two-fluid approach is used as the foundation for COBRA-NC.

The two-fluid formulation uses a separate set of conservation equations and constitutive relations for each phase. The effects of one phase on another are accounted for by interaction terms appearing in the equations. The conservation equations have the same form for each phase; only the constitutive relations and physical properties differ. Thus, although usually derived for two-phase flow, the two- fluid model immediately generalizes to n-phase flow.

The three-field formulation used in COBRA-NC is a straightforward extension of the two-fluid model. The fields included are gas/vapor mixture, continuous liquid, and entrained liquid. Dividing the liquid phase into two fields is the most convenient and physically reasonable way of handling flows where the liquid can appear in both film and droplet form. In such flows the motion of the droplets can be quite different from the motion of the film, so a single set of average liquid phase equations cannot adequately describe the liquid flow or the interaction between liquid and vapor.

This section describes the development of the two-component, two-fluid, three-field conservation equations solved in COBRA-NC. The two-fluid phasic conservation equations are presented in Section 2.1, along with the assumptions necessary to obtain them. (The derivation of these equations can be found in Appendix A of this volume.) In Section 2.2 the additional assumptions and notation for the three-field model are presented, and the two-component,

three-field conservation equations are derived. The equations are written out in component form in Section 2.3, and the classical subchannel form is compared with the Cartesian coordinate equations.

2.1 Two-Fluid Phasic Conservation Equations

The phasic conservation equations given in this section describe the time-averaged behavior of phase k, which can be any phase in a multiphase flow. All fluid variables appearing in these equations are time-averaged quantities. The averaging process used is described in Appendix A, where precise definitions of all the average variables are given. The phasic conservation equations are general within the assumptions listed below.

Assumptions

1. Gravity is the only body force.
2. There is no volumetric heat generation in the fluid.
3. Radiation heat transfer is limited to rod to drop and rod to steam.
4. The pressure is the same in all phases.
5. The dissipation can be neglected in the enthalpy formulation of the energy equation.

Although assumptions 3 and 4 considerably simplify the conservation equations, especially the energy equation, they also somewhat limit their applicability. However, for situations typically encountered in reactor safety analysis, these assumptions are usually justified. (Further discussion of these assumptions is given in Appendix A.)

Conservation of Mass

$$\frac{\partial}{\partial t}(\alpha_k \rho_k) + \nabla \cdot (\alpha_k \rho_k U_k) = \Gamma_k + \nabla \cdot \alpha_k \rho_m \epsilon_D \nabla W_k \qquad (1)$$

Rate of change of mass	+	Mass flux	=	Rate of mass transfer to phase k from the other phases	+	Mass flux due to turbulent diffusion

Conservation of Momentum

$$\frac{\partial}{\partial t}(\alpha_k \rho_k \underline{U}_k) + \nabla \cdot (\alpha_k \rho_k \underline{U}_k \underline{U}_k) = \alpha_k \rho_k \underline{g} - \alpha_k \nabla P$$

$$+ \nabla \cdot [\alpha_k (\underline{\underline{\tau}}_k + \underline{\underline{I}}_k^T)] + \underline{M}_k^{\Gamma} + \underline{M}_k^{d} \qquad (2)$$

	Rate of change of momentum	+	Momentum flux	=	Gravity force	+ Pressure gradient force
+	Viscous and turbulent forces	+	Momentum exchange due to mass transfer to phase k	+	Interfacial drag force	

Conservation of Energy

$$\frac{\partial}{\partial t}(\alpha_k \rho_k h_k) + \nabla \cdot (\alpha_k \rho_k h_k \underline{U}_k) = -\nabla \cdot [\alpha_k (Q_k + q_k^T)] + \Gamma_k h_k^i + q_{I_k}''' + \alpha_k \frac{\partial P}{\partial t} \qquad (3)$$

	Rate of change of enthalpy	+	Enthalpy flux	=	Conduction and turbulent heat flux
+	Energy exchange due to mass transfer to phase k	+	Interfacial heat transfer	+	Pressure derivative

The following definitions have been used in the above equations:

α_k = average k-phase void fraction

ϵ_D = k phase turbulent mass diffusivity

ρ_k = average k-phase density

ρ_m = average vapor/gas mixture density

$\underline{U}_k$ = average k-phase velocity

Γ_k = average rate of mass transfer to phase k from the other phases

$\underline{g}$ = acceleration of gravity

P = average pressure

$\underline{\underline{\tau}}_k$ = average k-phase viscous stress tensor (stress deviator)

$\underline{\underline{T}}$ = k-phase turbulent (Reynolds) stress tensor

$\underline{M}^{\Gamma}$ = average supply of momentum to phase k due to mass transfer to phase k

$\underline{M}_k^d$ = average drag force on phase k by the other phases

h_k = average k-phase enthalpy

Q_k = average k- phase conduction vector

q_k^T = k-phase turbulent heat flux

h_k^i = surface average enthalpy of phase k

W_k = k-phase mass concentration.

2.2 Three-Field Conservation Equations

In the two-component, three- field formulation there are four continuity equations, three momentum equations, and two energy equations. (The two liquid fields and the vapor/gas mixture are assumed to be in thermal equilibrium and the vapor and 2.3 noncondensable gas mixture are assumed to move at the same velocity.) These equations are obtained from Equations 1 through 3 by introducing the appropriate three-field notation and a few simplifying assumptions.

2.2.1 Three-Field Model Notation

In general, the subscripts v, mg, ℓ, and e refer to the vapor, noncondensable gas mixture, continuous liquid, and entrained liquid fields, respectively. The subscript vg refers to the vapor/gas mixture. The term describing mass transfer between phases is, however, handled somewhat differently. Let

Γ''' = average rate of vapor generation per unit volume

Because both liquid fields can contribute to the vapor generation rate, let

η = the fraction of the total vapor generation coming from the entrained liquid

Γ_e''' = average rate of vapor generation per unit volume coming from the entrained liquid, $\Gamma_e''' = \eta\Gamma'''$

Γ_ℓ''' = average rate of vapor generation per unit volume coming from the continuous liquid, $\Gamma_\ell''' = (1 - \eta)\Gamma'''$

The two liquid fields can exchange mass by entrainment as well as by phase change. For notation let

S''' = average net rate of entrainment per unit volume.

With the above definitions the mass transfer terms can be written as

$$\Gamma_v = \Gamma'''$$

$$\Gamma_\ell = -\Gamma_\ell''' - S''' = -(1 - \eta)\Gamma''' - S''' \tag{4}$$

$$\Gamma_e = -\Gamma_e''' + S''' = -\eta\Gamma''' + S'''$$

The interfacial momentum exchange terms can be expressed as

$$M_v^d = - \mathcal{I}_{I_{v\ell}}''' - \mathcal{I}_{I_{ve}}'''$$

$$M_\ell^d = \mathcal{I}_{I_{v\ell}}''' \tag{5}$$

$$M_e^d = \mathcal{I}_{I_{ve}}'''$$

where

$\mathcal{I}_{J_{v\ell}}^{"'}$ = average drag force per unit volume by the vapor/gas mixture on the continuous liquid

$\mathcal{I}_{I_{ve}}^{"'}$ = average drag force per unit volume by the vapor/gas mixture on the entrained liquid.

The momentum exchange due to mass transfer between the three fields can be written as

$$\underline{M}_v^{\Gamma} = (\Gamma"'\underline{U})$$

$$\underline{M}_{\ell}^{\Gamma} = -(\Gamma"'\underline{U}) - (S"'\underline{U}) \qquad (6)$$

$$\underline{M}_e^{\Gamma} = -(\Gamma_e"'\underline{U}) + (S"'\underline{U})$$

This notation was chosen to emphasize the fact that $\underline{M}_v^{\Gamma}$ is due only to vapor generation, but $\underline{M}_{\ell}^{\Gamma}$ and $\underline{M}_e^{\Gamma}$ are affected by both vapor generation and entrainment.

2.2.2 Three-Field Model Assumptions

To obtain the three-field model from Equations 1 through 3, the following assumptions are needed:

1. The turbulent stresses and turbulent heat flux of the entrained phase can be neglected, so

$$\underline{\underline{T}}_e^{T} = 0$$

$$\underline{q}_e^{T} = 0 \qquad (7)$$

2. When the equations are solved on a finite-difference grid, the viscous stresses can be partitioned into wall shear and fluid-fluid shear. The fluid-fluid shear can be neglected in the entrained liquid phase. The notation for this is given below.

$$\nabla \cdot (\alpha_e \underline{\underline{\tau}}_e) = \tau''' _{we}$$

$$\nabla \cdot (\alpha_v \underline{\underline{\tau}}_v) = \tau''' _{wv} + \nabla \cdot (\alpha_v \underline{\underline{\sigma}}_{vg}) \qquad (8)$$

$$\nabla \cdot (\alpha_\ell \underline{\underline{\tau}}_\ell) = \tau''' _{w\ell} + \nabla \cdot (\alpha_\ell \underline{\underline{\sigma}}_\ell)$$

In Equation 8, τ'''_{wv}, τ'''_{we}, and $\tau'''_{w\ell}$ are the forces exerted by the wall on the vapor/gas mixture, the entrained liquid and the continuous liquid, respectively; $\underline{\underline{\sigma}}_{vg}$ $\underline{\underline{\sigma}}_\ell$ are the fluid-fluid viscous stress tensors for the vapor/gas mixture and the liquid.

3. The conduction heat flux can be partitioned into a wall term and a fluid-fluid conduction term. The latter is assumed negligible in the entrained liquid. Thus,

$$-\nabla \cdot (\alpha_v Q_{vg}) = -\nabla \cdot (\alpha_v q_{vg}) + Q'''_{wv}$$

$$-\nabla \cdot (\alpha_e Q_e) = -\nabla \cdot (\alpha_\ell q_\ell) + Q'''_{w\ell} \qquad (9)$$

where Q'''_{wv} and $Q'''_{w\ell}$ are the wall heat transfer rates per unit volume to the vapor/gas mixture and liquid, respectively; q_ℓ is the fluid-fluid conduction vector for the continuous liquid; and q_{vg} is the fluid-fluid conduction vector for the vapor/gas mixture.

4. All mass entering a phase is at saturation. Therefore,

$$h_v^i = h_g \text{ (evaporation)}$$

$$h_\ell^i = h_f \text{ (condensation)} \tag{10}$$

All mass leaving a phase is at the phase enthalpy. Therefore

$$h_v^i = h_v \text{ (condensation)}$$

$$h_\ell^i = h_\ell \text{ (evaporation)}$$

2.2.3 Three-Field Equations

Substituting Equations 4 through 10 into Equations 1 through 3 and including separate mass equations for the noncondensable gas mixture and the vapor yields the three-field conservation equations used in COBRA-NC.

Conservation of Mass (four equations)

$$\frac{\partial}{\partial t}(\alpha_v \rho_v) + \nabla \cdot (\alpha_v \rho \underline{U}_{vg}) = \Gamma''' + \nabla \cdot \alpha_v \rho_{vg}\, \epsilon_D \nabla W_v + S'''_{cv}$$

$$\frac{\partial}{\partial t}(\alpha_\ell \rho_\ell) + \nabla \cdot (\alpha_\ell \rho_\ell \underline{U}_\ell) = -\Gamma'''_\ell - S''' + S'''_{c\ell}$$

$$\frac{\partial}{\partial t}(\alpha_e \rho_\ell) + \nabla \cdot (\alpha_e \rho_\ell \underline{U}_e) = -\Gamma'''_e + S''' + S'''_{ce}$$

$$\frac{\partial}{\partial t}(\alpha_v \rho_{mg}) + \nabla \cdot (\alpha_v \rho_{mg} \underline{U}_{vg}) = \nabla \cdot \alpha_v \rho_{vg}\, \epsilon_D \nabla W_g + S'''_{cg} \qquad (11)$$

Conservation of Momentum (three equations)

$$\frac{\partial}{\partial t}(\alpha_v \rho_{vg} \underline{U}_{vg}) + \nabla \cdot (\alpha_v \rho_{vg} \underline{U}_{vg} \underline{U}_{vg}) = -\alpha_v \Delta P + \alpha_v \rho_{vg} \underline{g}$$

$$+ \nabla \cdot [\alpha_v (\underline{\underline{\tau}}_{vg} + \underline{\underline{I}}^T_{vg})] + \tau'''_{wv} - \tau'''_{I_{v\ell}} - \tau'''_{I_{ve}} + (\Gamma''' \underline{U}) + S'''_{mv}$$

$$\frac{\partial}{\partial t}(\alpha_\ell \rho_\ell \underline{U}_\ell + \nabla \cdot (\alpha_\ell \rho_\ell \underline{U}_\ell \underline{U}_\ell) = -\alpha_\ell \Delta P + \alpha_\ell \rho_\ell \underline{g}$$

$$+ \nabla \cdot [\alpha_\ell (\underline{\underline{\tau}}_\ell + \underline{\underline{I}}^T_\ell)] + \tau'''_{I_{v\ell}} - (\Gamma'''_\ell \underline{U}) - (S''' \underline{U}) + S'''_{m\ell}$$

$$\frac{\partial}{\partial t}(\alpha_e \rho_\ell \underline{U}_e) + \nabla \cdot (\alpha_e \rho_\ell \underline{U}_e \underline{U}_e) = -\alpha_e \Delta P + \alpha_e \rho_\ell \underline{g} + \tau'''_{we} + \tau'''_{I_{ve}}$$

$$- (\Gamma'''_e \underline{U}) + (S''' \underline{U}) + S'''_{me} \qquad (12)$$

Conservation of Energy (two equations)

$$\frac{\partial}{\partial t}\left[\alpha_v(\rho_v h_v + \rho_g h_g)\right] + \nabla \cdot \left[\alpha_v(\rho_v h_v + \rho_g h_g)\underline{U}_{vg}\right] - - \nabla \cdot \left[\alpha_v(q''^T_{vg})\right]$$

$$+ \Gamma'''h^i_v + q'''_{I_v} + Q'''_{wv} + \alpha_v \frac{\partial P}{\partial t} + S'''_{ev}$$

$$\frac{\partial}{\partial t}\left[(\alpha_\ell + \alpha_e)\rho_\ell h_\ell\right] + \nabla \cdot (\alpha_\ell \rho_\ell h_\ell \underline{U}_\ell) + \nabla \cdot (\alpha_e \rho_\ell h_\ell \underline{U}_e)$$

$$= - \nabla \cdot \left[\alpha_\ell(q''_\ell + q''^T_\ell)\right] - \Gamma'''h^i_\ell + q'''_{I_\ell} + Q'''_{w\ell} + (\alpha_\ell + \alpha_e)\frac{\partial P}{\partial t} + S'''_{e\ell} \qquad (13)$$

The following terms have been added to the equations to account for sources of mass, momentum, and energy as a result of chemical reaction or source boundary conditions:

S'''_{ce} = entrained drop mass source per unit volume

S'''_{cg} = noncondensable mass source per unit volume

$S'''_{c\ell}$ = continuous liquid mass source per unit volume

S'''_{cv} = vapor mass source per unit volume

$S'''_{e\ell}$ = combined liquid energy source per unit volume

S'''_{ev} = vapor/gas mixture energy source per unit volume

S'''_{me} = entrained drop momentum source per unit volume

$S'''_{m\ell}$ = continuous liquid momentum source per unit volume

S'''_{mv} = vapor/gas mixture momentum source per unit volume.

The use of a single energy equation for the combined continuous liquid and liquid droplet fields means that both fields are assumed to be at the same temperature. In regions where both liquid droplets and liquid films are present, this can be justified in view of the large rate of mass transfer

between the two fields, which will tend to draw both to the same temperature. The use of a single momentum and energy equation for the vapor/gas mixture means that the vapor and the noncondensable gas mixture travel at the same velocity and have the same temperature within each computation cell. These assumptions lead to a great simplification in the numerical solution of the equations, resulting in a reduced computing cost. The user is cautioned to carefully review results for problems where temperature differences between the droplet field and continuous liquid within a single mesh cell may be significant.

Additional mass transport equations are solved to determine the mass of each gas species in the noncondensable gas mixture. If the gas mixture is composed of N species, then N-1 equations are solved for the mass concentration of N-1 species of the gas mixture. The mass concentration of the Nth species is determined from the expression:

$$\rho_N^{n+1} = \rho_{mg}^{n+1} - \sum_{i=1}^{N-1} \rho_i^{n+1} \tag{14}$$

The N-1 mass transport equations have the same form as the vapor and noncondensable gas mixture mass conservation equations:

$$\frac{\partial(\alpha_v \rho_i)}{\partial t} + \nabla \cdot (\alpha_v \rho_i \underline{U}_{vg}) = S_{cg_i} + \nabla \cdot \alpha_v \rho_{vg} \epsilon_D \nabla W_i \tag{15}$$

Rate of change of mass for gas component i	Mass flux for gas component i	Rate of mass creation for gas component i due to chemical reaction, etc.	Mass flux for gas component i due to turbulent diffusion

2.3 Three-Field Conservation Equations in Component Form

COBRA-NC has been developed for use with either rectangular Cartesian or subchannel coordinates. This allows a fully three-dimensional treatment in geometries amenable to description in a Cartesian coordinate system. For more complex or irregular geometries the user may select the subchannel formulation (which neglects some of the convective terms in the above equations) or a mixture of the two. The subchannel approach has been used by the COBRA (Ref. 3) codes for bundle thermal-hydraulic analysis. To illustrate the difference between the two formulations, the vapor momentum equation is written

out in component form for each case in the paragraphs below. (The momentum equations for the continuous and entrained liquid fields are treated analogously but are not shown.)

2.3.1 Cartesian Coordinates

Let u, v, and w denote the x, y, and z components of velocity with x being the vertical coordinate. The Cartesian components of the vapor/gas mixture momentum equation are:

x-component (vertical)

$$\frac{\partial}{\partial t}\left(\alpha_v \rho_{vg} u_{vg}\right) + \frac{\partial}{\partial x}\left(\alpha_v \rho_{vg} u_{vg} u_{vg}\right) + \frac{\partial}{\partial y}\left(\alpha_v \rho_{vg} u_{vg} v_{vg}\right) + \frac{\partial}{\partial z}\left(\alpha_v \rho_{vg} u_{vg} w_{vg}\right)$$

$$= -\alpha_v \frac{\partial P}{\partial x} - \alpha_v \rho_{vg} g + \tau'''_{wv_x} - \tau'''_{I_{v\ell_x}} - \tau'''_{I_{ve_x}} + \left(\Gamma'''U\right)_x \qquad (16)$$

y-component

$$\frac{\partial}{\partial t}\left(\alpha_v \rho_{vg} v_{vg}\right) + \frac{\partial}{\partial x}\left(\alpha_v \rho_{vg} v_{vg} u_{vg}\right) + \frac{\partial}{\partial y}\left(\alpha_v \rho_{vg} v_{vg} v_{vg}\right) + \frac{\partial}{\partial z}\left(\alpha_v \rho_{vg} v_{vg} w_{vg}\right)$$

$$= -\alpha_v \frac{\partial P}{\partial x} + \tau'''_{wv_y} - \tau'''_{I_{v\ell_y}} - \tau'''_{I_{ve_y}} + \left(\Gamma'''U\right)_y \qquad (17)$$

z-component

$$\frac{\partial}{\partial t}\left(\alpha_v \rho_{vg} w_{vg}\right) + \frac{\partial}{\partial x}\left(\alpha_v \rho_{vg} w_{vg} u_{vg}\right) + \frac{\partial}{\partial y}\left(\alpha_v \rho_{vg} w_{vg} v_{vg}\right) + \frac{\partial}{\partial z}\left(\alpha_v \rho_{vg} w_{vg} w_{vg}\right)$$

$$= -\alpha_v \frac{\partial P}{\partial z} + \tau'''_{wv_z} - \tau'''_{I_{v\ell_z}} - \tau'''_{I_{ve_z}} + \left(\Gamma'''U\right)_z \qquad (18)$$

2.3.2 Subchannel Coordinates

Fixed transverse coordinates are not used in the subchannel formulation. Instead, all transverse flows are assumed to occur through gaps (e.g., between fuel rods). Thus, one transverse momentum equation applies to all gaps regardless of the gap orientation. This reduces the number of component momentum equations to only two: vertical and transverse.

Vertical Momentum

$$\frac{\partial}{\partial t}\left(\alpha_v \rho_{vg} u_{vg} A\right) + \frac{\partial}{\partial x}\left(\alpha_v \rho_{vg} u_{vg} u_{vg} A\right) + \sum_k \left(\alpha_v \rho_{vg} u_{vg} v_{vg} S\right)_k$$

$$= -\alpha_v A \frac{\partial P}{\partial x} - \alpha_v \rho_{vg} A g + \tau'''_{wv_x} A - \tau'''_{I_{v\ell_x}} A + \left(\Gamma'''U\right)_x A \qquad (19)$$

Rate of change of vertical momentum	+	Vertical momentum flux by axial convection	+	Vertical momentum flux by transverse convection

=	Vertical pressure gradient force	+	Gravity force	+	Vertical wall shear	+	Vertical interfacial drag between vapor and continuous liquid	+	Vertical interfacial drag between vapor and entrained liquid	+	Vertical momentum exchange due to mass transfer to vapor

Transverse Momentum

$$\frac{\partial}{\partial t}(\alpha_v \rho_{vg} v_{vg} A_k) + \frac{\partial}{\partial L}(\alpha_v \rho_{vg} v_{vg} v_{vg} A_k) + \frac{\partial}{\partial x}(\alpha_v \rho_{vg} v_{vg} u_{vg} A) + \sum_{nk}(\alpha_v \rho_{vg} v_{vg} v_{vg_{nk}} S'_{nk})$$

$$= -\alpha_v A_k \frac{\partial P}{\partial L} + \tau'''_{wv_k} A_k \quad \tau'''_{I_{v\ell_k}} A_k + (\Gamma'''U)_k A_k \qquad (20)$$

Rate of change of transverse momentum	+ Transverse momentum flux by transverse convection	+ Transverse momentum flux by vertical convection	+ Transverse momentum flux by orthogonal transverse convection

= Transverse pressure gradient force	+ Transverse wall shear	+ Transverse interfacial drag between vapor and continuous liquid	+ Transverse interfacial drag between vapor and entrained liquid	+ Transverse momentum exchange due to mass transfer to vapor

The following notation has been used in the subchannel equations:

u = vertical velocity

v = transverse velocity

A = vertical flow area of subchannel

A_k = transverse flow area of gap k

S = gap width

S' = orthogonal gap width

L = transverse coordinate

Subscript k refers to gap k.

Subscript nk refers to orthogonal gap nk.

2.3.3 Comparison of Cartesian and Subchannel Equations

The subchannel vertical momentum equation, Equation 19, contains derivatives only with respect to x and t, and is already partially finite-difference. The corresponding Cartesian component equation, Equation 2.16, is still completely in differential form. To compare the two, the Cartesian equation must be put in a form compatible with the subchannel equation.

Figure 1 shows a rectangular control volume of length Δx taken from a single subchannel. Expressing Equation 16 in partially finite-difference form for this control volume yields

$$\frac{\partial}{\partial t}(\alpha_v \rho_{vg} u_{vg})A + \frac{\partial}{\partial x}(\alpha_v \rho_{vg} u_{vg} u_{vg})A$$

$$+ [(\alpha_v \rho_{vg} u_{vg} v_{vg})_{y_o+\Delta y} - (\alpha_v \rho_{vg} u_{vg} v_{vg})_{y_o}]\Delta z$$

$$+ [\alpha_v \rho_{vg} u_{vg} w_{vg})_{z_o+\Delta z} - (\alpha_v \rho_{vg} u_{vg} w_{vg})_{z_o}]\Delta y$$

$$= -\alpha_v \frac{\partial P}{\partial x} A - \alpha_v \rho_{vg} g A + \tau'''_{wv_x} A - \tau'''_{I_{v\ell_x}} A - \tau''_{I_{ve_x}} A + (\Gamma''')_x A \qquad (21)$$

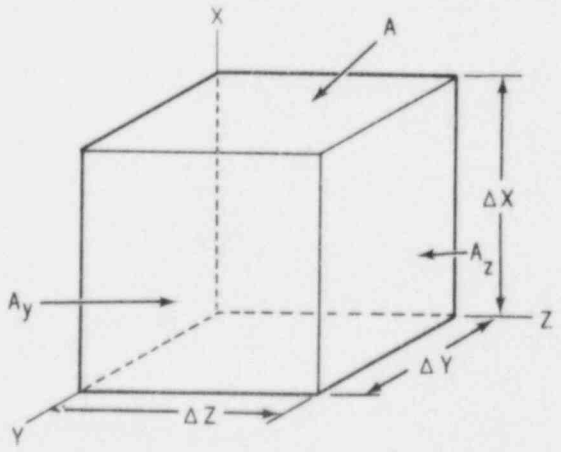

Figure 1 Control volume for Cartesian coordinates

The y- and z-direction vapor momentum equations can be created in the same fashion. Equation 17 becomes

$$\frac{\partial}{\partial t}(\alpha_v \rho_{vg} v_{vg}) A_y + \frac{\partial}{\partial y}(\alpha_v \rho_{vg} v_{vg} v_{vg}) A_y$$

$$+ [(\alpha_v \rho_{vg} v_{vg} u_{vg})_{x_o+\Delta\xi y} - (\alpha_v \rho_{vg} v_{vg} u_{vg})_{x_o}] \Delta z$$

$$+ [(\alpha_v \rho_{vg} v_{vg} w_{vg})_{z_o+\Delta z} - (\alpha_v \rho_{vg} v_{vg} w_{vg})_{z_o}] \Delta x$$

$$= - \alpha_v \frac{\partial P}{\partial x} A_y + \tau'''_{wv_y} A_y - \tau'''_{I_{v\ell_y}} A_y - \tau''_{I_{ve_y}} A_y + (\Gamma''')_y A_y \qquad (22)$$

and Equation 2.18 becomes

$$\frac{\partial}{\partial t}(\alpha_v \rho_{vg} w_{vg}) A_z + \frac{\partial}{\partial z}(\alpha_v \rho_{vg} w_{vg} w_{vg}) A_z$$

$$+ [(\alpha_v \rho_{vg} w_{vg} u_{vg})_{x_o+\Delta x} - (\alpha_v \rho_{vg} w_{vg} u_{vg})_{x_o}] \Delta y$$

$$+ [(\alpha_v \rho_{vg} w_{vg} v_{vg})_{y_o+\Delta y} - (\alpha_v \rho_{vg} w_{vg} v_{vg})_{y_o}] \Delta x$$

$$= - \alpha_v \frac{\partial P}{\partial x} A_z + \tau'''_{wv_z} A_z - \tau'''_{I_{v\ell_z}} A_z - \tau''_{I_{ve_z}} A_z + (\Gamma''')_z A_z \qquad (23)$$

The conditions for equivalence between the subchannel and Cartesian momentum equations can be demonstrated with the above equations. Assuming the subchannels are arranged in a rectangular array, equivalence requires

$$\sum_k (\alpha_v \rho_{vg} u_v v_v S)_k = [\alpha_v \rho_{vg} u_{vg} v_{vg})_{y_o+\Delta y} - (\alpha_v \rho_{vg} u_{vg} v_{vg})_{y_o}]\Delta z$$

$$+ [(\alpha_v \rho_{vg} u_{vg} w_{vg})_{z_o+\Delta z} - (\alpha_v \rho_{vg} u_{vg} w_{vg})_{z_o}]\Delta y \qquad (24)$$

In addition gaps with unit vectors in the y-direction must have

$$\sum_{nk} (\alpha_v \rho_{vg} v_{vg} v_{vg_{nk}} S'_{nk}) = [\alpha_v \rho_{vg} v_{vg} w_{vg})_{z_o+\Delta z} - (\alpha_v \rho_{vg} v_{vg} w_{vg})_{z_o}]\Delta x \qquad (25)$$

while gaps with unit vectors in the z-direction must have

$$\sum_{nk} (\alpha_v \rho_{vg} v_{vg} v_{vg_{nk}} S'_{nk}) = [\alpha_v \rho_{vg} w_{vg} v_{vg})_{y_o+\Delta y} - (\alpha_v \rho_{vg} w_{vg} v_{vg})_{y_o}]\Delta x \qquad (26)$$

The user selects either the three-dimensional Cartesian equations or the subchannel formulation by input. When the subchannel formulation is chosen, the second and fourth terms on the left side of the transverse momentum equation (Equation 20) are not specified, yielding the historical form of the subchannel transverse momentum equation. The corresponding components of viscous and turbulent shear stresses are also neglected in the subchannel formulation.

2.4 Lumped Parameter Equations

The conservation equations can also be solved in lumped parameter form in COBRA-NC. This formulation is most often useful for modeling nuclear containments that contain several large rooms. The lumped parameter form of the conservation equations is derived by eliminating the momentum efflux and turbulent and viscous shear stresses from the momentum equations and the turbulent diffusion term from the mass and energy equations. All other terms remain the same as in the finite-difference equations. The lumped parameter equations are:

Conservation of Mass (four equations)

$$\frac{\partial}{\partial t}(\sim_{*}\rho_v) + \nabla \cdot (\alpha_v \rho_v U_{vg}) = \Gamma''' S'''_{cv}$$

$$\frac{\partial}{\partial t}(\alpha_\ell \rho_\ell) + \nabla \cdot (\alpha_\ell \rho_\ell U_\ell) = -\Gamma'''_\ell - S''' + S'''_{c\ell}$$

$$\frac{\partial}{\partial t}(\alpha_e \rho_\ell) + \nabla \cdot (\alpha_e \rho_\ell U_e) = -\Gamma'''_e + S''' + S'''_{ce}$$

$$\frac{\partial}{\partial t}(\alpha_v \rho_g) + \nabla \cdot (\alpha_v \rho_g U_{vg}) = S'''_{cg} \qquad (25)$$

Flow Equations (three equations)

$$\frac{\partial}{\partial t}(\alpha_v \rho_{vg} U_{vg}) = -\alpha \Delta P + \alpha_v \rho_{vg} g + \mathcal{I}'''_{wv} - \mathcal{I}'''_{I_{v\ell}} - \mathcal{I}'''_{I_e}$$

$$\frac{\partial}{\partial t}(\alpha_\ell \rho_\ell U_\ell) = -\alpha_\ell \Delta P + \alpha_\ell \rho_\ell g + \mathcal{I}_{w\ell} + \mathcal{I}'''_{I_{v\ell}}$$

$$\frac{\partial}{\partial t}(\alpha_e \rho_\ell U_e) = -\alpha_e \Delta P + \alpha_e \rho_\ell g + \mathcal{I}'''_{we} + \mathcal{I}'''_{I_{ve}} \qquad (26)$$

Conservation of Energy Equations (two equations)

$$\frac{\partial}{\partial t}\left[\alpha_v(\rho_v h_v + \rho_g h_g)\right] + \nabla \cdot \left[\alpha_v(\rho_v h_v + \rho_g h_g)\, \underline{U}_{vg}\right]$$

$$= \Gamma''' h_v^i + q_{I_v}''' + Q_{wv}''' + \alpha_v \frac{\partial P}{\partial t} + S_{ev}'''$$

$$\frac{\partial}{\partial t}\left[(\alpha_\ell + \alpha_e)\, \rho_\ell h_\ell\right] + \nabla \cdot (\alpha_\ell \rho_\ell h_\ell \underline{U}_\ell) + \nabla \cdot (\alpha_e \rho_\ell h_\ell \underline{U}_e)$$

$$= -\Gamma''' h_\ell^i + q_{I_\ell}''' + Q_{w\ell}''' + (\alpha_\ell + \alpha_e) \frac{\partial P}{\partial t} + S_{e\ell}''' \qquad (27)$$

The lumped parameter formulation can be specified for all or part of the computational mesh.

3.0 PHYSICAL MODELS

The conservation equations presented in Section 2.0 are solved numerically on a finite-difference mesh made up of numerous computational cells. Closure of the equation set requires physical models for the mass exchange among the three fields at the phase interfaces, the exchange of momentum at the interfaces, the drag forces at solid boundaries, the viscous stress and turbulence terms in the continuous fields, and the entrainment rate. In addition, property relations for water, its vapor, and the noncondensable gas mixture are needed.

This section contains descriptions of the physical models used in COBRA-NC. To facilitate the explanation of the physical models, a brief description of the computational cell structure and variable placement is given in Section 3.1. (A more complete discussion of this topic can be found in Volume 2, Numerical Solution Methods.) To implement many of these models, the code must define the flow regime. Section 3.2 describes the flow regime map and various parameters used to characterize two- phase flow, such as bubble size and film thickness. The interfacial mass transfer model is explained in Section 3.3, and in Section 3.4 the interfacial drag force is discussed. Section 3.5 contains in wall drag force model. The viscous stress, turbulent stress, and turbulent heat flux models are described in Section 3.6. Section 3.7 describes the entrainment models. Fluid thermodynamic and transport properties are discussed in Section 3.8.

3.1 Computational Cell Structure

A typical finite-difference mesh is shown in Figure 2. The fluid volume is partitioned into a number of computational cells. The equations are solved using a staggered difference scheme in which the velocities are obtained at the mesh cell faces and the state variables, such as pressure, density, enthalpy, and void fraction are obtained at the cell center.

The mesh cell is characterized by its cross- sectional area, A; its height, Δx; and the width, S, of its connection with adjacent mesh cells. The cell depicted in Figure 2 is a mass/energy cell, so named because it is the cell used for solving the scalar continuity and energy equations. The momentum equations are solved on staggered cells that are centered on the scalar mesh cell face. The vertical and transverse momentum cells are shown in Figure 3.

3.2 Flow Regime Selection

Several flow regime maps have been proposed and used by various investigators to describe observed two-phase flow patterns (Ref. 4,5,6). While many of these maps are useful within the range of the data for which they were developed, none can be generally applied to all two-phase flow problems. For example, flow patterns observed in a test section containing hot surfaces are different from those observed in a similar test section having the same mass flux and quality but no hot surfaces. The accurate prediction of exactly

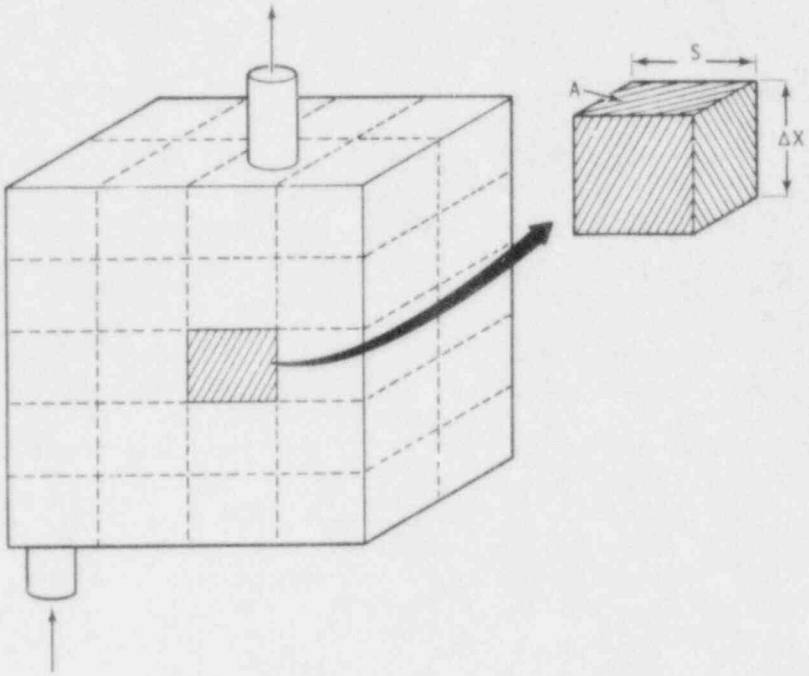

Figure 2 Mass/energy cell

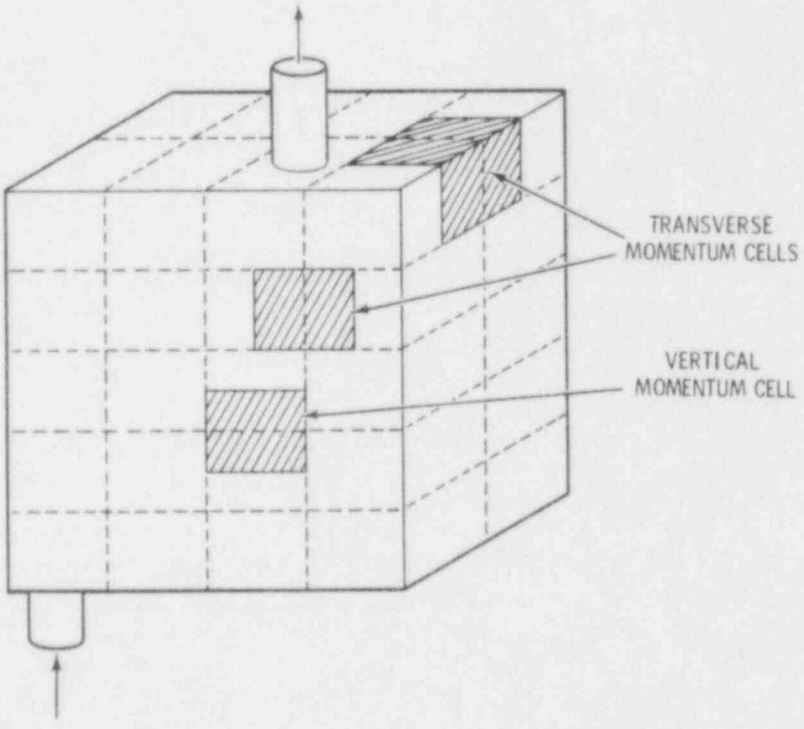

Figure 3 Vertical and transverse momentum cells

which flow regime can be expected under a given set of flow conditions is beyond the current understanding of two-phase flow. With this in mind, the physical basis of existing flow regime maps was studied to develop the most widely applicable and yet simplest flow regime map possible for use in COBRA-NC. In this regard, the work by A. E. Dukler (Ref. 6) at the University of Houston pertaining to flow regime transitions in vertical flow has been very helpful.

The flow regime map used in COBRA-NC can be divided into two main parts: 1) the logic used to select 3.1 physical models in the absence of unwetted hot surfaces (e.g., fuel rods) and 2) the logic used when hot surfaces are present. The flow regimes described by the first set of logic are referred to as "normal" flow regimes, while those described by the second set are called "hot wall" flow regimes. Because COBRA-NC was developed for vertical two-phase flow, horizontal flow regimes are not considered.

The physical models used in the numerical solution must be defined for each mesh cell. Therefore, the flow regime must be determined from fluid properties and flow conditions within each cell or in the immediate surrounding cells. When selecting a mesh size, care must be taken to ensure that the local flow regime map renders the correct global flow regime for the problem under consideration.

3.2.1 Normal Flow Regimes

The physical models are selected using the normal flow regime logic if a mesh cell does not contain any solid surface with a temperature greater than 705°F. A schematic of the normal flow regimes is shown in Figure 4. The flow regimes considered include dispersed bubbly flow, slug flow, churn-turbulent flow, film flow, and film mist flow. The logic for determining the appropriate flow regime and the transitions between flow regimes is illustrated schematically in Figure 5.

If the local void fraction is less than 0.2, a dispersed bubbly flow is assumed. The flow consists of spherical or distorted bubbles with radius r_b determined from a critical Weber number criterion as

$$r_b(\text{ft}) = \min\left(0.5\,\frac{We_b\,\sigma}{\rho_\ell |U_{v\ell}|^2}\,,\ 0.5D_H,\ 0.02\right) \tag{28}$$

where $U_{v\ell} = U_{vg} - U_\ell$. A critical Weber number of 10 is used.

Bubbles in flashing or boiling two-phase flow will grow around nucleation sites located within the fluid volume or on solid surfaces bounding the fluid volume. The number of such sites is dependent on several factors, including the nature and amount of solid surface as well as the amount of contaminants

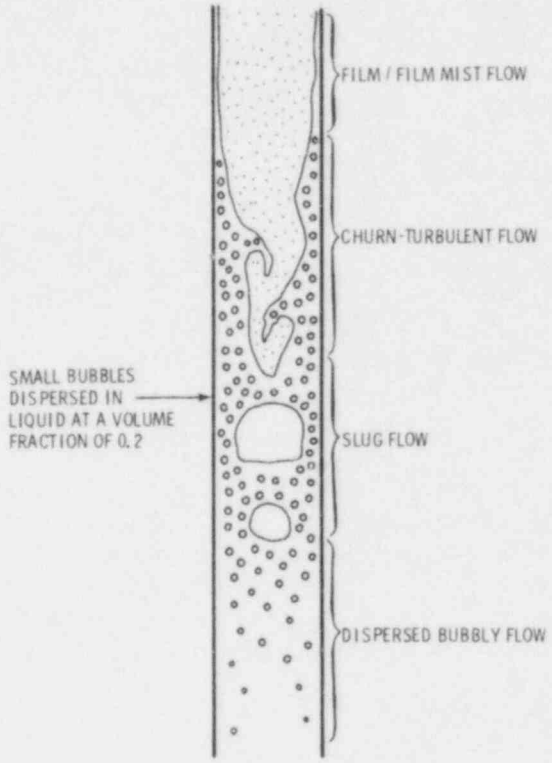

Figure 4 Normal two-phase flow regimes

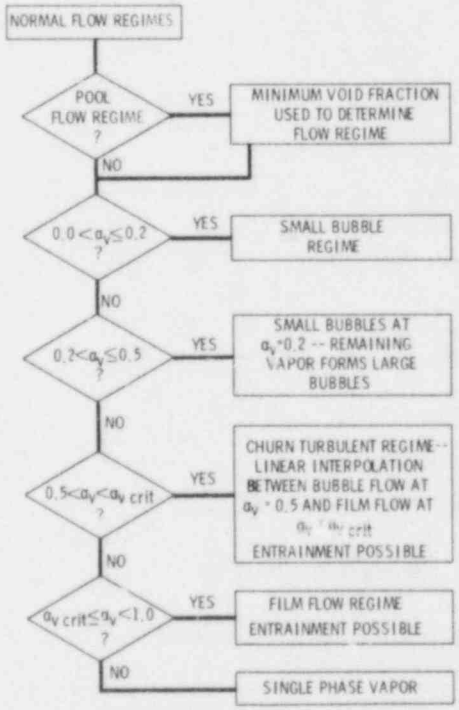

Figure 5 Normal flow regime selection logic

and noncondensable gases present in the fluid. The surface area for interfacial heat transfer between the superheated liquid and vapor phases is computed using a bubble radius that is the lesser of the two values given by Equation 28 and that obtained from a minimum bubble number density:

$$r_b = \left(\frac{3}{4}\frac{\alpha_m}{\pi N_b}\right)^{1/3} \tag{29}$$

where $N_b = 2.0 \times 10^9$ and is the larger of α_v and 0.001. N_b is in units of number of bubbles per cubic foot. The purpose of this model is to provide an interfacial area for the initiation of flashing. This value is highly dependent on the purity of the water being considered. Better models for this parameter need to be developed, and the model proposed here should be considered as only the current best estimate. The effect of solid surfaces on bubble nucleation is treated separately and will be discussed in more detail in Section 3.3. The bubble size computed from Equation 28 is always used to compute the interfacial shear on small bubbles.

It has been observed (Ref. 6) that, as the vapor content of the flow increases, a point is reached when the dispersed bubbles become so closely packed that they collide with one another and coalesce into larger bubbles. Although these larger bubbles may be unstable and tend to break up again, the collision frequency is sufficiently high to maintain larger bubbles. This is the beginning of the transition to slug flow. It is assumed that this process begins at a void fraction of 0.2. For void fractions above 0.2, the continuous liquid is assumed to contain small dispersed bubbles at a volume fraction of 0.2 (that is, the small bubbles occupy 20% of the total volume occupied by the mixture of continuous liquid and small bubbles), while the remainder of the vapor forms a larger bubble. The large bubble will grow with increasing vapor content of the flow until it reaches the maximum allowable bubble size; then another larger bubble will begin forming (see Figure 4). The radius of the large bubble is given by

$$r_b = \left[\frac{3}{4\pi}\left(\alpha_v - 0.25\,\alpha_\ell\right) \cdot (\text{Volume of cell})\right]^{1/3} \tag{30}$$

and is limited to half the hydraulic diameter of the flow channel. Once the larger bubble has grown to this size, another bubble will begin to grow.

As the vapor content of the flow increases, the large bubbles will begin to coalesce, and a transition into churn-turbulent and then film flow will occur. it is assumed that this begins to occur at a void fraction of 0.5. The churn-turbulent flow regime is assumed until a stable liquid film is achieved. The void fraction at which a stable liquid film will exist depends on the flow channel size and the vapor velocity. The critical void fraction above which a stable film can be maintained is determined from a force balance between the disruptive force of the pressure gradient over the crest of waves on the film and the restraining force of surface tension. The resulting expression for the critical film thickness is (Ref. 7)

$$\delta_{crit} = \frac{C_1 \sigma}{\rho_v |U_{v\ell}|^2} \tag{31}$$

The constant C_1 contains the effects of wave shape and amplitude on the surface tension force and pressure force, and the relationship between the wave amplitude and film thickness. If the wave amplitude is assumed to be about four times the film thickness, the value of C_1 should be about 0.5. Comparison of the model with the onset of entrainment data of Dukler (Ref. 8) indicated that a C_1 of 0.5 is a reasonable value. The film thickness in a flow channel is given by

$$\delta = \frac{\alpha_\ell D_H}{4} \tag{32}$$

Substituting this into the equation for critical film thickness gives the expression for the critical void fraction for stable film flow:

$$\alpha_{v_{crit}} = 1.0 - 4.0\, C_1 \sigma / \rho_{vg} |U_{v\ell}|^2\, D_H \tag{33}$$

The critical void fraction is limited to a minimum value of 0.8, the value at which waves can be expected to bridge across the flow channel and cause a transition to churn flow. The interfacial geometry of the churn-turbulent flow is treated as a linear interpolation between bubble flow and film flow. The flow is considered to consist entirely of bubbly flow as described above

at a void fraction of 0.5 and entirely of film flow at the critical void fraction. Entrainment of liquid from the continuous liquid field into the droplet field is allowed in this flow regime. The entrainment rate is interpolated between 0.0 at a void fraction of 0.5 to the full value given by the entrainment correlations at the critical void fraction. This provides a smooth transition into film or film mist flow. It should be noted that, so long as the vapor velocity is sufficiently high to carry liquid drops away, the film mist flow regime will be maintained. This is consistent with Dukler's explanation for the transition to film flow. This transition is predicted by the code based on the models used for the entrainment rate and interfacial drag between the vapor and drops.

Additional checks are made to ensure that the flow regimes assumed locally are consistent with the global flow pattern. This is done by checking for a large void fraction difference between two mesh cells. If the difference in void fraction between the two cells is greater than 0.4, then it is assumed that a liquid pool or froth front exists, and the smaller void fraction is used to determine the flow regime and physical models in the pool. If the difference in void fraction between a cell and the cell above it is greater than 0.4, then an inverted pool is assumed, and the lower void fraction is used to determine the flow regime and physical models. This inverted pool regime can occur in the downcomer of a pressurized water reactor during emergency core coolant injection. The size of the bubbles formed as the vapor penetrates the inverted pool interface is assumed to be the larger of the Weber-number-controlled bubble radius and an instability-controlled bubble radius given by

$$r_b = \frac{\sigma}{\rho_{vg} u_R^2} \tag{34}$$

where u_R is the vertical vapor/gas velocity below the interface minus the vertical liquid velocity at the interface.

The same kind of check is made in the transverse directions. The lower void fraction is again used to determine flow regime and physical models. In all other cases the void fraction of the staggered momentum mesh cell is used to determine flow regimes and physical models in that cell. Between a void fraction difference of 0.4 and 0.2 the void fraction is ramped from the smaller void fraction to the void fraction of the staggered momentum mesh cell. Physical models required for the continuity mesh cells (i.e., interfacial heat transfer coefficients and areas) are taken to be the average of two adjacent momentum mesh cell values.

A check is made in the bubbly flow regimes to determine if vapor is concentrated at the walls of the flow channel as a result of vapor generation due to wall heat transfer. The vertical vapor velocity resulting from vapor generation at the heat transfer surface is given by

$$u_\Gamma = \min \left(\frac{\Gamma''' \, \Delta x}{\alpha_v \rho_v}, \frac{Q'''_{w\ell} \, \Delta x}{h_{fg} \alpha_v \rho_v} \right) \tag{35}$$

where Δx is the vertical length increment of the mesh. This expression assumes that all vapor generated within the cell leaves vertically. The bubble rise velocity relative to the liquid is given by (Ref. 9)

$$U_{BR} = 1.414 \left(\sigma g \Delta \rho / \rho_\ell^2 \right)^{1/4} / (1 - \alpha_v) \tag{36}$$

If vapor is being generated at the wall at a faster rate than it can be carried away by the flow, i.e., if $(u_\Gamma - u_\ell) > u_{BR}$, then the vapor is assumed to be concentrated at the wall. The interfacial drag model computes a smaller drag coefficient than would be possible for bubbles dispersed uniformly in the liquid.

3.2.2 Hot Wall Flow Regimes

Effective cooling of the core is lost during the blowdown stage of a loss-of-coolant accident in light water reactors, and the core is subjected to a nearly adiabatic heatup. The steam environment surrounding the rods does not provide sufficient heat transfer from the cladding to remove heat being added from stored energy in the fuel pellets and from fission product decay. This temperature excursion is halted by the injection of emergency core cooling (ECC) water into the reactor vessel.

As the cooling water enters the core, it contacts the hot rods and begins to re-establish effective cooling of the core. It is during this period that the temperature excursion of the cladding is turned around. Complex hydrodynamic and heat transfer processes take place during this phase of the transient as a result of saturated or subcooled water coming into contact with the high-temperature cladding. When the cladding temperature is above the surface rewetting temperature, a film boiling heat transfer mechanism will be established. This may correspond to either a dispersed flow regime or an inverted-annular, two-phase flow regime, depending upon the liquid content of

the flow and the vapor velocity. As the cladding temperature is reduced because of the cooling provided by film boiling, the cladding will enter a transition boiling and finally a nucleate boiling regime. The temperature will fall below the surface rewet temperature, and the surface will quench. Heat transfer from the rod will then take place in the form of nucleate boiling or single-phase liquid heat transfer, depending on the subcooling and flow rate of the liquid entering the core. The rate at which liquid will enter the core during bottom reflood is limited by the available driving head provided by the liquid in the downcomer and the flow resistance through the broken hot leg. During top reflood, the rate at which liquid will enter the core is controlled by the countercurrent flow limitation.

High flow rates of superheated vapor result from the steam generated as the rods are quenched. Vapor velocities are usually high enough to entrain significant fractions of the liquid in the form of drops. This droplet entrainment is beneficial because it enhances heat transfer downstream of the quench front by desuperheating the steam and contributing to the total steam flow rate as the drops evaporate.

The "hot wall" flow regimes are used when a mesh cell contains a solid surface with a temperature greater than 705°F. These flow regimes describe the hydrodynamics of the highly nonhomogeneous, thermal nonequilibrium, two-phase flow encountered during reflood. The "hot wall" flow regimes include subcooled inverted annular flow, saturated liquid chunk flow, dispersed drop-vapor flow, falling film flow, and top deluge.

The normal direction for reflood is from the bottom of the core, but a top quench front is assumed to exist if the mesh cell above the cell with a hot wall contains no surfaces with a temperature greater than 705°F. If the void fraction is greater than 0.8, a falling film flow regime is assumed in the cell containing the top quench front; otherwise, a top deluge is assumed. In the deluge regime the flow is assumed to consist of large liquid chunks having diameters equal to the flow channel hydraulic diameter. Droplet deposition and entrainment is allowed in the falling film regime.

An inverted annular flow regime is assumed during bottom reflood if the continuous liquid phase is subcooled. This regime consists of a liquid core surrounded by a vapor film. If the liquid is saturated, then a liquid chunk flow regime is assumed in which the flow is considered as liquid drops surrounded by vapor. Entrainment of liquid into the entrained droplet field is allowed in this flow regime, permitting a transition to dispersed flow based on the physical models for the entrainment rate and droplet/vapor interfacial drag. The breakup of droplets on grid spacers is also considered. The hot wall flow regimes are illustrated in Figure 6; Figure 7 shows the selection logic.

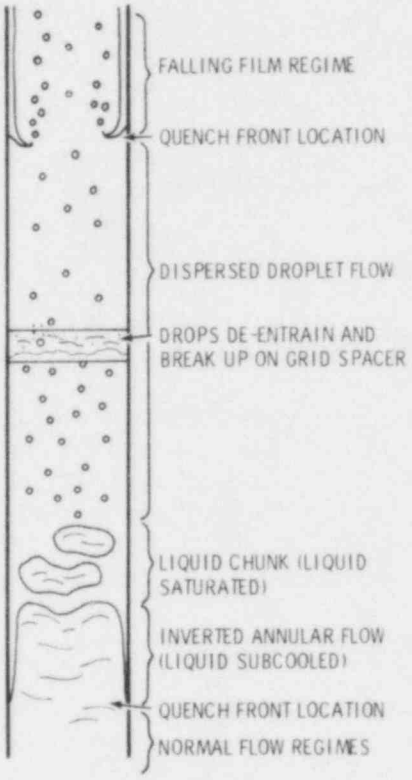

Figure 6 Hot wall flow regimes

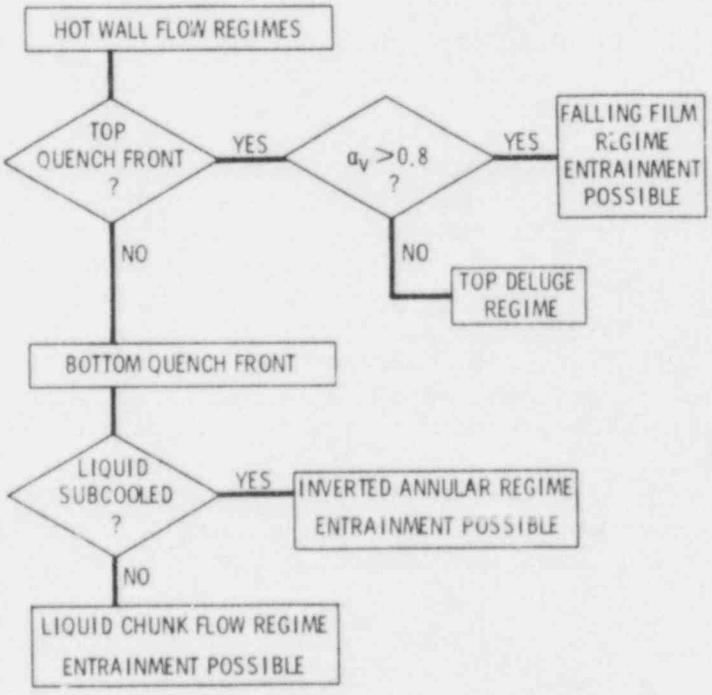

Figure 7 Hot wall flow regime selection logic

3.3 Interfacial Mass Transfer

The model for interfacial mass transfer is obtained from the energy jump condition, Equation A.37, by neglecting the mechanical terms and averaging. This yields

$$\Gamma''' = \frac{-q_{I_\ell}''' - q_{I_v}'''}{\Delta h_k^i} \tag{37}$$

where

$\Delta h_k^i = (h_g - h_\ell)$ for vaporization and

$\Delta h_k^i = (h_v - h_f)$ for condensation.

The interfacial heat transfer, q_I''' for phase k is given 3.5 by

$$q_{I_k}''' = H\, A_I'''\, (T_s - T_k) \tag{38}$$

where A_I''' is the average interfacial area per unit volume and H is a surface heat transfer coefficient. It is convenient to divide the vapor generation into four components, two for each phase, depending on whether the phase is superheated or subcooled. The total vapor generation rate is given by the sum of these components. For example, Γ_{SHL}''', the vapor generation per unit volume resulting from superheated liquid, is given by

$$\Gamma_{SHL}''' = \frac{H_{SHL} A_I'''\, (h_\ell - h_f)}{C_{p\ell}\, (h_g - h_\ell)} \tag{39}$$

Analogous relationships hold for subcooled liquid (SCL), superheated vapor (SHV), and subcooled vapor (SCV). The fraction (η) of total vapor generation coming from the entrained liquid is given by

$$\eta = \min \left[\frac{\alpha_e}{1-\alpha_v} , \left(1.0 - \frac{Q'''_{w\ell}}{\Gamma'''_{fg}}\right)\right], \text{ for vaporization}$$

The interfacial area per unit volume, A'''_I, is based on flow regime, as are the heat transfer coefficients, H. Correlations for the various heat transfer coefficients are given in Table 1, and models for interfacial area for each flow regime are given in Table 2. The various Reynolds numbers used in Table 1 are defined as follows.

Table 1 Interfacial Heat Transfer Coefficients

Mode of Heat Transfer	Correlation (Btu/hr-ft^2-°F)		Flow Regime
H_{SHV}	1.0×10^{4} (a)		Bubble
	$(2.0 + 0.74\ Re_{vg}^{0.5}\ Pr_{vg}^{1/3})\ \frac{k_v}{D_H}$	(Ref. 10)	Large Bubble
	$\frac{f_I}{2}\ \rho_v\ C_{p_{vg}}\ \lvert U_{v\ell}\rvert Pr_{vg}^{-2/3}$		Film
	$(2.0 + 0.74\ Re_d^{0.5}\ Pr_{vg}^{1/3})\ \frac{k_{vg}}{2r_d}$	(Ref. 10)	Drop
	$(2.0 + 0.74\ Re_{vg}^{0.5}\ Pr_{vg}^{1/3})\ \frac{k_{vg}}{D_H}$		Liquid chunk, inverted annular
H_{SCV}	1.0×10^{4} (a)		All regimes

(a) Constant large value used to drive phase to equilibrium

(Table 1, continued)

Mode of Heat Transfer	Correlation (Btu/hr-ft^2-°F)		Flow Regime
H_{SHL}	$\frac{1}{\sqrt{\pi}} \left(\frac{k_\ell \lvert U_{v\ell}\rvert}{r_b} \rho_\ell C_{p\ell}\right)^{1/2}$		Bubble
	1.0×10^{5}[a]		Large bubble, liquid chunk and inverted annular
	The maximum of		
	$1.925\, \rho_\ell C_{p\ell} \lvert U_\ell \rvert / (Re_f^{2/3} Pr_\ell^{2/3})$		Film[b]
	for $Re_f < 1000$		
	$0.2701 \rho_\ell C_{p_\ell} \lvert U_\ell \rvert / (Re_f^{0.38} Pr_\ell^{2/3})$		
	for $1000 \leq Re_f$		
	and:		
	$2.0 k_\ell / \delta$		
	$C \frac{\pi^2}{3} \frac{k_\ell}{r_d}$ (C = 2.7)	(Ref. 11)	Drop

(a) Constant large value used to drive phase to equilibrium

(b) From Colburn analogy using friction factors of Hughmark (Ref. 13)

(Table 1, continued)

Mode of Heat Transfer	Correlation (Btu/hr-ft^2-°F)		Flow Regime
H_{SCL}	$\frac{1}{\sqrt{\pi}} \left(\frac{k_\ell \lvert U_{v\ell} \rvert}{r_b} \rho_\ell C_{p_\ell}\right)^{1/2}$	(Ref. 12)	Bubble, large bubble
	The maximum of:		
	$\frac{2K_\ell}{\delta}$		
	and:		
	$1.925\ \rho_\ell C_{p_\ell} \lvert U_\ell \rvert / (Re_f^{2/3}\ Pr_\ell^{2/3})$ Film[(a)]		
	or: $2[\min (280.0, 79.33\ (\rho_v/\rho_{mg})^{0.8})]$	(Ref. 13)	
	for $Re_f < 1000$		
	$0.2701\ \rho_\ell C_{p_\ell} \lvert U_\ell \rvert / (Re_f^{0.29}\ Pr_\ell^{2/3})$		
	for $1000 \leq Re_f$		
	$C \frac{\pi^2}{3} \frac{k_\ell}{r_d}$ $(C = 2.7)$	(Ref. 11)	Drop, liquid chunk inverted annular

(a) From Colburn analogy using friction factors of Hughmark (Ref. 13)

Table 2 Interfacial Heat Transfer Area Per Unit Volume

Flow Regime	Interfacial Area, A_i'''
Bubble	$N_b\ 4\pi r_b^2$ (a)
Film	$\sqrt{\alpha_v}\ P_w/A$
Liquid chunk	$N_d\ \pi\ D_H^2$ (b)
Inverted annular	$\sqrt{\alpha_\ell}\ P_w/A$
Drop	Drop interfacial area transport equation (Equations 44 and 45)

(a)

$$N_b = \frac{\alpha_v}{\frac{4\pi}{3} r_b^3}$$

(b)

$$N_d = \frac{\alpha_\ell}{\frac{\pi D_H^3}{6}}$$

$$Re_{vg} = \frac{D_H \rho_{vg} |U_{v\ell}|}{\mu_{vg}}$$

$$Re_b = \frac{2r_b \rho_\ell |U_{v\ell}|}{\mu_{m_b}} \quad , \quad \mu_{m_b} = \mu_\ell (1 - \alpha_v)^{-2.5} \frac{(\mu_{vg} + 0.4\ \mu_\ell)}{(\mu_{vg} + \mu_\ell)}$$

$$Re_d = \frac{2r_d\ \rho_{vg} |U_{ve}|}{\mu_{m_d}} \quad , \quad \mu_{m_d} = \mu_{vg} \alpha_v^{-2.5} \frac{(\mu_\ell + 0.4\ \mu_{vg})}{(\mu_{vg} + \mu_\ell)}$$

$$Re_f = \frac{D_H\ \rho_\ell |U_\ell|}{\mu_\ell} \tag{40}$$

The friction factor, f_I, is given by Wallis (Ref. 14):

$$f_I = 0.005\ (1 + 75\ \alpha_\ell) \tag{41}$$

The smaller of the bubble size given by the Weber number criterion (Equation 28) and that given by the bubble number density (Equation 29) is used to compute the area for superheated liquid interfacial heat transfer. In addition, nucleation on solid surfaces is accounted for by an additional interfacial heat transfer coefficient and area given by

$$(H_{SHL} A_I''')_{WALL} = \frac{k_\ell}{D_H} (8.0 + 0.023\ Re_\ell^{0.8}\ Pr_\ell^{0.4}\ \frac{P_w}{A}) \tag{42}$$

Here the interfacial area has been assumed to be equal to the surface area of the solid structure within the mesh cell, and the interfacial heat transfer coefficient is given by the Dittus-Boelter correlation (Ref. 15). A more general correlation for nucleation on solid surfaces is needed and will replace Equation 42, should one become available.

When noncondensable gases are present, the subcooled liquid interfacial heat transfer coefficients given in Table 1 are reduced by the factor

$$F_{con} = 0.168 \left(\frac{\alpha \rho_v^2}{\rho_{mg} (1-\alpha_v) \rho_\ell}\right)^{0.1} \tag{43}$$

F_{con} is limited to a maximum value of 1.0. This model is based on Russian jet data (Ref. 75) and can dramatically reduce the condensation rate when noncondensable gases are present.

The effect of grid spacers on the superheated vapor interfacial heat transfer during reflood is added to the interfacial heat transfer between drops and vapor. Experimental data (Ref. 16) has indicated that grid spacers have a significant effect on desuperheating the vapor flowing through the grid spacer. This effect is important, as the reduced vapor temperature enhances the rod heat transfer in the upper portions of the bundle, resulting in lower peak cladding temperatures. As droplets pass through the grid spacer, a certain fraction of them will hit the grid structure. As the droplets hit the grid impact creates a splatter of smaller droplets, which rapidly evaporate. This has been accounted for by increasing the droplet interfacial area by 55% in mesh cells containing grids. (This value is based on FLECHT/SEASET data.)

When a combination of flow regimes exists within a mesh cell, the product of the total interfacial heat transfer coefficient and area is the sum of the HA_I''' for all regimes. For example, if the flow consists of small and large bubbles, the total is given as

$$H_{SHL}A_I''' = (H_{SHL}A_I''')_{\substack{\text{SMALL} \\ \text{BUBBLES}}} + (H_{SHL}A_i''')_{\substack{\text{LARGE} \\ \text{BUBBLES}}} \tag{44}$$

The same is true for liquid film and drops, etc.

The product of the interfacial area and heat transfer coefficient is ramped to zero as the volume fraction of the depleting phase approaches zero. The following ramps are applied to each of the heat transfer coefficients:

HA_{SCL}:

$$\text{RAMP} = \max(0.0, \min(1.0, (\alpha_v - 0.001)/0.0099)) * \max(0.0, \min(1.0, (P_S - 0.311)/0.7))$$

HA_{SHL} and HA_{SHV}:

$$\text{RAMP} = \max(0.0, \min(1.0, (0.99999 - \alpha_v)/0.00009))$$

HA_{SCV}:

$$\text{RAMP} = \max(0.0, \min(1.0, (\alpha_v - 0.0001)/0.0099)) * \max(0.0, \min(1.0, (P_S - 0.311)/0.7))$$

The total interfacial area of drops within a mesh cell is determined by solving an interfacial area concentration transport equation as follows:

$$\frac{\partial A'''_{I_d}}{\partial t} + \nabla \cdot (A'''_{I_d} \underline{U}_e) = \frac{3\, S'''}{\rho_\ell r_s} + S_\Gamma \qquad (45)$$

Rate of change of interfacial area concentration	+ Flux of interfacial are concentration	= Rate of interfacial area generation due to entrainment and deposition of drops	+ Rate of interfacial area concentration change due to phase change

Once a drop is formed, no further breakup is assumed to occur, and the drops change size only as a result of condensation, vaporization, or new drop formation. The drop size is easily computed from the interfacial area as

$$r_d = 3\, \alpha_e / A'''_{I_d} \qquad (46)$$

The expression for r_s, the drop formation size, is dependent on the conditions under which the drop is formed, and is discussed with the entrainment model in Section 3.7.

3.4 Interfacial Drag Force

The average interfacial drag force per unit volume between the vapor/gas mixture and continuous liquid is defined as a function of relative velocity,

$$\mathcal{I}''_{I_{v\ell}} = K_{I_{v\ell}} \underline{U}_{v\ell} \tag{47}$$

The drag force between the vapor/gas mixture and entrained liquid is also a function of the relative velocities of the two fields,

$$\mathcal{I}''_{I_{ve}} = K_{I_{ve}} \underline{U}_{ve} \tag{48}$$

The interfacial friction coefficients, K_I, are dependent on flow regime and are defined as follows:

Bubble

$$K_{I_{v\ell}} = 0.375 \frac{C_{D_b}}{r_b} \alpha_v \rho_\ell |\underline{U}_{v\ell}| \tag{49}$$

Drop

$$K_{I_{ve}} = 0.375 \frac{C_{D_d}}{r_d} \alpha_e \rho_{vg} |\underline{U}_{ve}| \tag{50}$$

Film

$$K_{I_{v\ell}} = 2.0 \frac{f_I}{D_H} \sqrt{\alpha_v}\, \rho_{vg} |U_{v\ell}| \tag{51}$$

Inverted Annular

$$K_{I_{v\ell}} = 2.0 \frac{f_I}{D_H} \sqrt{\alpha_\ell}\, \rho_{vg} |U_{v\ell}| \tag{52}$$

The relative velocity used to calculate the interfacial drag between the small bubbles and the liquid phase in the small-bubble to large-bubble flow regime transition is limited to the smaller of the relative velocities calculated by the code on the relative velocity given by the drift flux model, $V_r = [(C_o-1) j + V_{gj}]/(1.0 - \alpha_{SB})$. This is required in order to calculate the correct drag between the small bubbles and liquid phase as the flow tends more and more toward slug or churn turbulent flow because the actual slip between the phases in these flow regimes is much larger than that between bubbles and liquid.

Expressions for the bubble and drop drag coefficients, C_D and $C_{D,}$ are

discussed by Ishii (Ref. 9). The drag coefficients are Reynolds number dependent and closely related to the drag coefficients for single bubbles and drops in an infinite medium. The drag coefficient for a single bubble in an infinite liquid medium is shown in Figure 8. The bubble is considered to behave as a solid sphere in the viscous regime. At higher Reynolds numbers the bubble is characterized by a distorted shape and irregular motion. In this distorted particle regime the drag coefficient increases with Reynolds number. As the Reynolds number further increases, the bubble becomes spherical cap-shaped and the drag coefficient becomes constant.

As discussed by Ishii, in the viscous regime the drag coefficient of a single particle in a multiparticle system may be assumed to have the same functional form as that of single particle in an infinite medium, provided that the Reynolds number is computed using the appropriate mixture viscosity. Therefore, in the viscous regime the drag coefficient on a bubble is given by

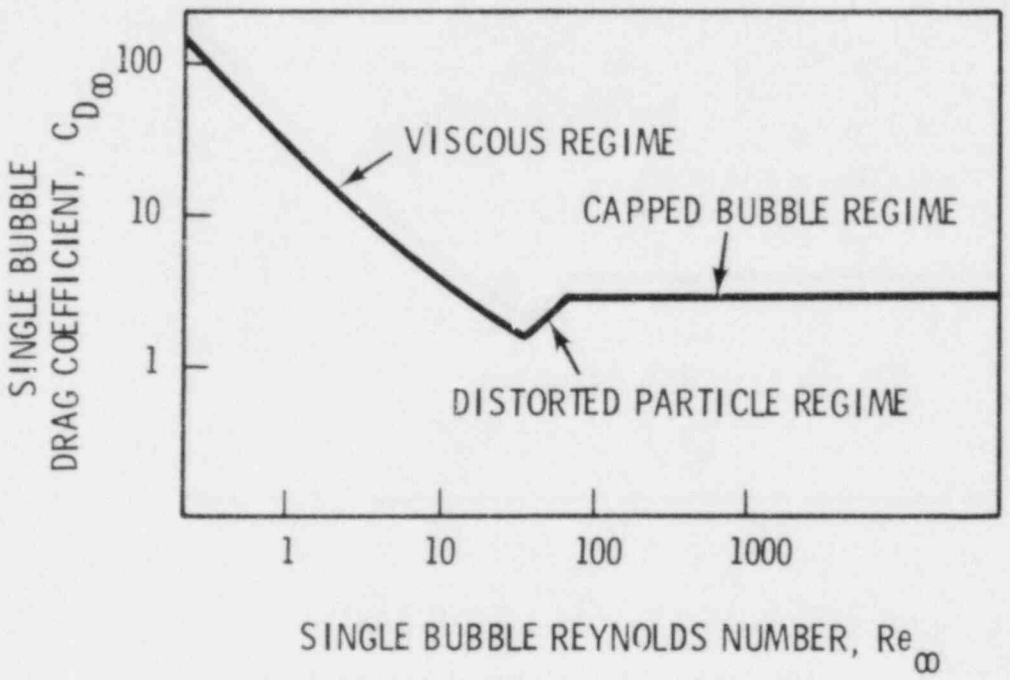

Figure 8 Single-bubble drag coefficient

$$C_{D_b} = \frac{24}{Re_b} (1.0 + 0.1\ Re_b^{0.75}) \tag{53}$$

where Re_b is defined as in Equation 40. The mixture viscosity is used in Re_b because a particle moving in a multiparticle system experiences a greater resistance than a single particle in an infinite medium. As it moves it must deform not only the fluid but the neighboring particles as well. The effect is seen by the particle as an increased viscosity.

In the distorted particle regime it is again assumed that the drag coefficient for a particle in a multiparticle system is the same as that of a single particle in an infinite medium with the Reynolds number based on a mixture viscosity. In addition, it is assumed that churn-turbulent flow always exists in the distorted particle regime. Under these conditions a particle tends to

move in the wake caused by other particles. Therefore, the velocity used in the drag coefficient and Reynolds number should be the drift velocity, $\underline{U}_{vj} = (1 - \alpha_v)\,\underline{U}_{v\ell}$. The drag coefficient in the churn-turbulent regime is then

$$C_{D_b} = \frac{\sqrt{2}}{3} N_\mu \, Re'_b \, (1 - \alpha_v)^2 \tag{54}$$

where

$$N_\mu = \frac{\mu_\ell}{\left(\rho_\ell \sigma \sqrt{\frac{\sigma}{g(\rho_\ell - \rho_{vg})}}\right)} \, 1/2 \tag{55}$$

$$Re'_b = 2\, r_b\, \rho_\ell (1 - \alpha_v) |\underline{U}_{v\ell}| \mu_m \tag{56}$$

and

$$\mu_m = \frac{\mu_\ell}{(1 - \alpha_v)} \tag{57}$$

The $(1 - \alpha_v)^2$ in the expression for the drag coefficient results from using the drift velocity to compute the drag force.

Churn-turbulent flow is also assumed for the cap bubble regime where

$$C_{D_b} = \frac{8}{3} (1 - \alpha_v)^2 \tag{58}$$

For the large-bubble flow regime, Equation 53 is assumed to apply down to the limit of Newton's regime where the drag coefficient for a single solid sphere

becomes constant at a value of 0.45. Within Newton's regime the large bubbles are assumed to move with respect to the average volumetric flux and, therefore,

$$C_{D_b} = 0.45\ (1 - \alpha_v)^2 \tag{59}$$

The viscous regime is assumed for drops, and the drag coefficient has the same form as that for bubbles except the Reynolds number is Re_d, as defined by Equation 40. The drop drag coefficient is limited to a minimum value of 0.45.

The friction factor, f_I, for film flow is dependent on whether the film is stable or unstable. It has been observed experimentally that the onset of film instability causes a sudden increase in system pressure drop. This is a result of increased roughness of the liquid film caused by large, unstable waves. Although, the film friction factor for unstable film flow in large tubes has been studied, the correlation does not extrapolate to hydraulic diameters typical of LWR fuel bundles. Henstock and Hanratty (Ref. 17) have correlated a large amount of cocurrent and countercurrent film flow data; however, their correlation does not predict the sudden increase in pressure drop at the onset of instability.

Until further information becomes available, it has been assumed that the film friction factor for stable films is given by the correlation recommended by Wallis (Ref. 14), Equation 41. This expression is also used for unstable films when solving the transverse momentum equations. When solving the vertical momentum equations, the friction factor for unstable films is taken to be the larger of either Henstock and Hanratty's correlation or five times the value of f_I given by the Wallis correlation.

Henstock and Hanratty's correlation is of the form

$$f_I = f_s \left\{1 + 1400\ F \left[1 - \exp\left(-\frac{1}{G}\,\frac{(1 + 1400\ F)^{3/2}}{13.2\ F}\right)\right]\right\} \tag{60}$$

where

$$G = \frac{\rho_\ell \, g \, D_H}{\rho_v \, u_{vg}^2 f_s}$$

$$F = \frac{m^+}{Re_v^{0.9}} \frac{\mu_\ell}{\mu_{vg}} \sqrt{\frac{\overline{\rho_v}}{\rho_\ell}}$$

$$m^+ = [(0.707 \, Re_\ell^{0.5})^{2.5} + (0.0379 \, Re_\ell^{0.9})^{2.5}]^{0.40}$$

$$f_s = 0.046 \, Re_{vg}^{-0.20} \tag{61}$$

The multiplication factor of five on the Wallis correlation was obtained from the observed difference between the pressure drop characteristics for stable films and that for unstable films (Ref. 8). This can be replaced by a more appropriate correlation, should one become available. The friction factor for inverted annular flow is assumed to be a constant,

$$f_I = 0.01 \tag{62}$$

until more information is available.

An additional interfacial drag force is calculated for interfaces that occur at mesh cell boundaries. These interfaces are detected by changes in void fraction between adjacent cells, and can occur on either horizontal or vertical cell boundaries. For two cells, i and j, connected to each other by a vertical or transverse connection, an intercell interface is assumed when $\alpha_i > 0.8$ and $\alpha_j < 0.6$, so that cell i is on the vapor side of the interface and cell j is on the liquid side. The drag force is a function of the difference between the vapor velocity in cell i and the liquid velocity in cell j, and is given by

$$F_{I_X} = f_I \frac{1}{2} \rho_{vg} |u_{vg_i} - u_{\ell_j}| (u_{vg_i} - u_{\ell_j}) A_{I_X} \quad (63)$$

for the vertical direction and

$$F_{I_y} = f_I \frac{1}{2} \rho_{vg} |V_{vg_i} - v_{\ell_j}| (v_{vg_i} - V_{\ell_j}) A_{I_Y} \quad (64)$$

for the transverse direction. In these equations A_{Ix} and A_{Iy} are the

appropriate intercell areas. A friction factor of 0.08 is assumed and has given good results. The intercell interfacial force is added to the liquid momentum equation in cell j (on the liquid side of the interface) and subtracted from the vapor momentum equation in cell i (on the vapor side). This force is necessarily added to the equations to account for the shear stress between the vapor and liquid phases when the interface between the phases is on the mesh cell face. The shear stresses previously discussed describe the momentum transfer between the phases within a mesh cell. A common example of an intercell interface would be when one mesh cell is full of water adjacent to one that is full of steam. Because each mesh cell is completely single phase, the equations previously described would predict no momentum transfer between the phases. However, the separation of the phases at the mesh cell boundary is an artificial one imposed by the numerical solution of the equations and, in reality, there would be momentum transfer between the two phases.

The interfacial shear between the continuous liquid and vapor/gas mixture is ramped to a large value as the vapor/gas volume fraction approaches zero to eliminate water packing problems. The ramp is:

$$\text{RAMP} = 1.0/(\max(1.0e^{-10}, \min((\alpha_v - 0.001)/0.009)))^3.$$

Also, the liquid flow rate and pressure derivative are ramped to zero as the donor cell liquid volume fraction approaches zero.

$$\text{RAMP} = \max(0.0, \min(1.0, (\alpha_\ell - 0.0001)/0.0009)).$$

3.5 Wall Drag Force

The wall drag forces per unit volume on each phase, $\tau''_{w\ell}$, τ''_{wv}, and τ''_{we}, are defined as functions of the phase velocities

$$\tau''_{w\ell} = - K_\ell U_\ell \tag{65}$$

$$\tau''_{wv} = - K_v U_{vg} \tag{66}$$

$$\tau''_{we} = - K_e U_e \tag{67}$$

The drag coefficients, K_ℓ, K_e, and K_v, contain both the local form loss and the friction factor, and are defined as

$$K_\ell = \left(\frac{f_\ell}{2D_H} + \alpha_\ell \frac{K}{2\Delta x}\right) \rho_\ell |U_\ell| \tag{68}$$

$$K_v = \left(\frac{f_{vg}}{2D_H} + \alpha_v \frac{K}{2\Delta x}\right) \rho_v |U_{lvg}| \tag{69}$$

$$K_e = \alpha_e \frac{K}{2\Delta x} \rho_\ell |U_e| \tag{70}$$

The friction factors for single-phase liquid flow, f_ℓ, and single-phase vapor/gas flow, f_{vg}, are computed from laminar or modified Blasius correlations based on the single-phase liquid or vapor Reynolds number.

$$f_k = \begin{cases} 64.0/Re_k & \text{laminar flow} \\ 0.0055 + 0.55\ Re_k^{-1/3} & \text{turbulent flow} \end{cases} \tag{71}$$

The vapor friction factor, f_{vg}, is set to zero for the bubbly, film, and single-phase liquid flow regimes. The liquid friction factor, f_ℓ, is set to zero for the single-phase vapor, inverted annular, and droplet (no film) flow regimes. The loss coefficient k, is the normal velocity head loss coefficient defined by the relationship $\Delta P = \frac{k}{2} \rho V^2$.

3.6 Viscous Stress and Turbulence Models

As noted in Section 2.2.2, the viscous stresses and the turbulence terms are modeled only in the continuous liquid and vapor/gas fields. For the fluid-fluid viscous stress tensor, $\underline{\underline{\tau}}_\ell$ Ishii (Ref. 2) proposes the relationhip

$$\underline{\underline{\tau}}_\ell = 2 \mu_\ell (\underline{\underline{D}}_{\ell_B} + \underline{\underline{D}}_{\ell_I}) \tag{72}$$

where

$$\underline{\underline{D}}_{\ell_B} = \frac{1}{2} [\nabla \underline{U}_\ell + (\nabla \underline{U}_\ell)^t] \tag{73}$$

and

$$\underline{\underline{D}}_{\ell_I} = - \frac{b_\ell(\alpha_\ell)}{2\alpha_\ell} [\nabla \alpha_\ell (\underline{U}_{vg} - \underline{U}_\ell) + (\underline{U}_{vg} - \underline{U}_\ell) \nabla \alpha_\ell] \tag{74}$$

The tensors $\underline{\underline{D}}_{\ell_B}$ and $\underline{\underline{D}}_{\ell_I}$ are called the bulk and interfacial deformation tensors, respectively, and $(b_\ell(\alpha_\ell)$ is called the mobility of the liquid phase.

The viscous stress model used in the code is a simplified version of the above model. The interfacial deformation and the viscous contributions to the normal stresses are neglected. Thus, the viscous stress model becomes

$$\underline{\underline{\tau}}_\ell = 2\mu_\ell \underline{\underline{D}}^*_\ell \tag{75}$$

where

$$D^{*}_{\ell_{ij}} = \frac{1}{2}\left(\frac{\partial U_{\ell_j}}{\partial x_i} + \frac{\partial U_{\ell_i}}{\partial x_i}\right)(1 - \delta_{ij}) \tag{76}$$

The simplest three-dimensional turbulence model is a generalization of Prandtl's mixing length theory. With this in mind, Ishii (Ref. 2) assumes

$$\underline{\underline{T}}^{T}_{\ell} = 2\mu^{T}_{\ell}\left(\underline{\underline{D}}_{\ell_B} + \underline{\underline{D}}_{\ell_I}\right) \tag{77}$$

where μ^{T}_{ℓ} is an eddy viscosity for the liquid and can be a function of α_{ℓ}, ρ_{ℓ}, $U_{v\ell}$, the distance to the nearest wall, and the scalar invariant of $(\underline{\underline{D}}_{\ell_B} + \underline{\underline{D}}_{\ell_I})$. Drew and Lahey (Ref. 18) point out that Equation 77 predicts zero turbulent normal stress in a simple shear flow and therefore cannot be correct. They propose a more general model involving four unknown parameters that must be determined by experiment. (Because no experimental results for these parameters have been published, their model is not usable at this time.)

A generalization of the Ishii model has been implemented in the code. The turbulent stress tensor is given by

$$\underline{\underline{T}}^{T}_{\ell} = P^{T}_{\ell}\,\underline{\underline{E}}_{\ell} + 2\mu^{T}_{\ell}\,\underline{\underline{D}}^{*}_{\ell} \tag{78}$$

The turbulent pressure, defined by

$$P^{T}_{\ell} = -\frac{1}{3}\,T^{T}_{\ell_{jj}} \tag{79}$$

is included to model the normal stresses, while the deformation term models the shear stresses. The tensor $\underline{\underline{F}}_\ell$, defined by

$$\underline{\underline{F}}_\ell = \begin{bmatrix} F_{\ell_{11}} & 0 & 0 \\ 0 & F_{\ell_{22}} & 0 \\ 0 & 0 & F_{\ell_{33}} \end{bmatrix} \tag{80}$$

is included to allow for nonisotropic normal stresses. A model for $\underline{\underline{F}}_\ell$ is still needed and is subject to the constraint

$$\sum_{j=1}^{3} F_{\ell_{jj}} = 3 \tag{81}$$

The following forms are assumed for P_ℓ^T and μ_ℓ^T:

$$P_\ell^T = \rho_\ell \ell_m^2 \left(2 \underline{\underline{D}}^*_{\ell_B} : \underline{\underline{D}}^*_{\ell_B}\right) \tag{82}$$

where ℓ_m is the momentum mixing length for the continuous liquid.

The mixing length is input by the user. In rod bundles a value equal to the hydraulic diameter is recommended. Either constant or spatially varying values for ℓ_m and F_ℓ can be used. Although these parameters will generally vary with position in the flow, constant values have given good results in rod bundles, where the scale of the turbulence is well defined by the rod geometry. (The values of ℓ_m and F_ℓ are specified by user input.)

The formulation of the turbulent heat flux consistent with the above turbulent stress treatment is

$$q_\ell^T = - \rho_\ell \epsilon_\ell^T \nabla h_\ell \tag{83}$$

where ϵ_ℓ^T is the turbulent thermal diffusivity and is given by

$$\epsilon_\ell^T = \ell_h \ell_m \sqrt{2 \overline{\underline{\underline{D}}_{\ell_B}^* : \underline{\underline{D}}_{\ell_B}^*}} \tag{84}$$

In this expression ℓ_{h_ℓ} is the energy mixing length for the liquid.

The sum of the conduction and turbulent heat flux becomes

$$q_\ell + q_\ell^T = - \rho_\ell (\epsilon_\ell + \epsilon_\ell^T) \nabla h_\ell \tag{85}$$

where $\epsilon_\ell = k_\ell / \rho_\ell C_{p\ell}$ is the liquid thermal diffusivity. With the introduction of the Prandtl number, ($Pr_\ell = C_{p\ell} \mu_\ell / k_\ell$) and the turbulent Prandtl number ($Pr_\ell^T = \mu_\ell^T / \rho_\ell \epsilon_\ell^T$), the above equation can be written as

$$q_\ell + q_\ell^T = - \left(\frac{\mu_\ell}{Pr_\ell} + \frac{\mu_\ell^T}{Pr_\ell^T} \right) \nabla h_\ell \tag{86}$$

The turbulent Prandtl number must be specified by user input and is generally equal to 1.0. The viscous stresses and turbulence terms for the vapor/gas mixture are treated in the same manner as for the liquid, but these terms are computed only for the continuous phase. The continuous phase is assumed to be the liquid for $\alpha < 0.6$, and the vapor gas mixture for $\alpha > 0.8$. A ramp between the two is used for $0.6 < \alpha < 0.8$.

3.7 Entrainment Rate

Entrainment of liquid drops from the continuous liquid phase can occur under a variety of conditions. The physical models used to determine the average net mass rate of entrainment and the drop formation size will be different for each condition. Entrainment mechanisms that may have a significant influence on reactor thermal hydraulics have been addressed in the development of entrainment models. These include entrainment from liquid films, reflood entrainment, entrainment resulting from vapor bubbling through liquid pools, and entrainment resulting from vapor flow across rod structures such as the upper plenum internals of a PWR.

The net mass entrainment rate is defined as

$$S = S''' \cdot (\text{Volume of cell}) \tag{87}$$

The net mass entrainment rate, S, has units of mass per unit time and is the net result of the opposing mechanisms of entrainment, S_E, and de-entrainment, S_{DE}. Models for entrainment rate, de-entrainment rate, and drop formation size are discussed below.

3.7.1 Entrainment in Film Flow

The entrainment of drops from the liquid film has been studied by numerous investigators (Ref. 7,8,19,20,21). Several different mechanisms for entrainment have been proposed, most of which depend upon the stability of the liquid film. As noted by Hewitt and Hall-Taylor (Ref. 19), the hydrodynamics of film flow as they relate to entrainment are extremely complex and have not been completely quantified. The simplistic approach taken here is an appropriate first attempt at describing a hydrodynamically complex process. Random perturbations in the flow cause the development of a wavy interface on the film. These waves will grow as a result of the hydrodynamic and surface tension forces acting on the wave. Eventually the amplitude of the wave becomes so large that the pressure differential over the wave exceeds the restraining force of surface tension, and the wave breaks toward the gas core. The resulting drops are then carried along with the vapor. The shape and size of the wave depends on whether the film flow is cocurrent or countercurrent. Lower-amplitude roll waves with drops being sheared off the wave crest are typical of cocurrent flow (Ref. 21). Abrupt, large-amplitude waves are typical of countercurrent flow (Ref. 7). This may be partially attributed to the fact that high vapor velocities are required to cause vertical cocurrent upflow. As a result, the film thickness and wave amplitudes are generally smaller than those found in countercurrent vertical flow, which occurs at lower vapor velocities. Also, in countercurrent flow the shear forces act in opposition to gravity, causing larger wave amplitudes.

The model used for the countercurrent case is simple. The entrainment rate (S_E) is taken to be the difference between the liquid flow rate in the film and the critical film flow rate:

$$S_E = (\alpha_\ell - \alpha_{\ell_{crit}}) \rho_\ell |u_\ell| A \tag{88}$$

The critical liquid fraction is defined as

$$\alpha_{\ell_{crit}} = (1 - \alpha_{v_{crit}}) \tag{89}$$

where $\alpha_{v_{crit}}$ is given by Equation 3.6.

It is assumed that all liquid in excess of that required for a stable film is removed from the film and enters into the entrained liquid phase, where it is treated as drops. In reality some of this liquid may be in the form of waves that travel upward while the bulk of the film flows down. The gross flow split between the amount of liquid flowing down and that flowing up in the form of drops and waves is obtained by the above assumption. This is sufficient for most applications. A similar model was used by Lovell (Ref. 7) to predict the penetration rate of liquid against an upflow of vapor.

Whalley, Hewitt and Hutchinson (Ref. 22) have correlated entrainment data for cocurrent film flow with the parameter

$$S_k = k_s \tau_I / \sigma \tag{90}$$

where k_s, the equivalent sand roughness, is used as the length scale for the containment force due to surface tension, and τ_I is the interfacial shear stress. Wurtz (Ref. 23) later modified the above correlation by multiplying it by the dimensionless velocity $|U_{vg}| \mu_\ell / \sigma$ to compare with a larger variety of data. This velocity was also used by Paleev and Filippovich (Ref. 24) to correlate air-water entrainment data. This resulting correlating parameter,

$$S_u = \frac{k_s \tau_I |U_{vg}| \mu_\ell}{\sigma^2} \tag{91}$$

was then used to obtain a relationship for the entrainment rate. This relationship is

$$S_E = 0.41\, S_u P_w\, \Delta x \tag{92}$$

where Δx is the vertical dimension of the mesh cell. This empirical correlation is used to determine the entrainment rate for cocurrent film flow. The equivalent sand roughness is given as

$$k_s = [0.57]\delta + [6625.0\ ft^{-1}]\delta^2 - [3.56 \times 10^6\ ft^{-2}]\delta^3 + [1.5736 \times 10^9\ ft^{-3}]\delta^4 \tag{93}$$

and

$$\tau_I = \frac{f_I}{2} \rho_v |u_{v\ell}|^2 \tag{94}$$

Correlations for the interfacial friction factor, f_I, have been given with the interfacial drag model in Section 3.4.

The size of drops formed by entrainment from films has been characterized by Tatterson et al. (Ref. 25). Their results are used for both cocurrent and countercurrent flow. The drop formation radius is given by

$$r_s = 0.0056 \left(\frac{D_H\, \sigma}{\frac{f_s}{2} \rho_v |u_{vg}|^2} \right)^{1/2} \tag{95}$$

where f_s is defined in Equation 61.

3.7.2 De-Entrainment in Film Flow

The deposition of drops on the liquid film occurs as a result of random turbulent motions that impart transverse velocity to the drops, bringing them into contact with the solid surfaces or liquid films within the flow channel. The rate at which this occurs has been correlated by Cousins et al. (Ref. 26) using a drop concentration gradient diffusion model in which the concentration at the wall is assumed to be zero. Cousins' model is used to determine the de-entrainment rate for film flow as

$$S_{DE} = k_\sigma \Delta C \, P_w \, \Delta x \tag{96}$$

where ΔC is the concentration gradient as given by

$$\Delta C = \frac{\alpha_e \rho_\ell}{\alpha_e + \alpha_v} \tag{97}$$

and k_σ is the mass transfer coefficient. The mass transfer coefficient has been found to be a function of surface tension (Ref. 27). This function is reasonably represented by

$$k_\sigma = \max \{3.0491 \times 10^{12} \, \sigma^{5.3054}, \, 12.491 \, \sigma^{0.8968}\} \tag{98}$$

3.7.3 Entrainment During Reflood

Several mechanisms for the formation of droplets during reflood can be postulated. The droplets may be formed by the breakup of the inverted annular liquid core because of surface instabilities if the liquid is subcooled. If the liquid is saturated, droplets may be formed by bubbles breaking through the surface of the liquid. During top reflood, droplets are formed at the sputtering front as the liquid film is disrupted by the large vaporization rates.

A model similar to one proposed for droplet entrainment by vapor bubbling through liquid pools (Ref. 28) is used for bottom reflood. The entrainment rate is given by

$$S_E = (\alpha_v u_{vg}/u_{crit})^2 \dot{m}_v \tag{99}$$

where $\dot{m}$ is the vertical vapor mass flow rate and u_{crit} is the vertical vapor velocity required to lift a droplet with radius defined by the critical Weber criterion against gravity. The critical velocity is obtained from a balance between the drag force and gravity force acting on the drop,

$$u_{crit} = \left(\frac{4\ We_d}{3C_D}\right)^{1/4} \left(\frac{\sigma g \Delta\rho}{\rho_{vg}^2}\right)^{1/4} \tag{100}$$

A Weber number of 2.7 (typical of reflood in the FLECHT tests) and a drag coefficient of 0.45 are used. The use of the vapor flow rate, $\dot{m}_v$, in Equation 99 reflects the effect of boiling at the quench front on droplet formation.

It is assumed that the entrainment rate from a falling film top quench front is equal to the liquid film flow rate, $\dot{m}_\ell$, minus the vapor generation rate at the quench front, Γ_q''', multiplied by the volume of the cell:

$$S_E = \dot{m}_\ell - \Gamma_q''' \text{ (volume of cell)} \tag{101}$$

The droplet formation size for both top and bottom reflood is assumed to be given by a critical Weber number criterion,

$$r_s = 0.5 \frac{We_d \sigma}{\rho_{vg}(u_{v\ell})^2} \quad (102)$$

with a Weber number of 2.7. The maximum droplet size for top reflood is limited to r_s = 0.003 feet. The low value for the Weber number is a result of using the superficial velocity to compute the droplet size. The vapor velocity where the drops are formed is much higher than the superficial velocity as a result of the reduced void fraction near the quench front.

3.7.5 De-Entrainment on Structure

Liquid drops may be de-entrained on structural surfaces as the drops flow around the structures such as support columns and guide tubes in reactor vessel upper plenums or various structures within containment rooms. This liquid will form a liquid film on the structure that may then flow down the structures and form a pool above the upper core plate or on the containment floor.

The model used in the code is simple, employing de-entrainment fractions obtained in the upper plenum de-entrainment experiments of Dallman and Kirchner (Ref. 29):

$$S_{DE} = \eta_{NR} \alpha_e \rho_\ell |V_e| \text{ (transverse flow area)} \quad (103)$$

The de-entrainment fraction, η_{NR}, is input. Following the recommendations of Dallman and Kirchner, the de-entrainment fraction for an array of tubes is given by

$$\eta_{NR} = 1 - (1 - \eta_R)^N$$

$$\eta_R = \eta_I (1 + 4.5 \beta^2) \quad (104)$$

where η_R = the de-entrainment fraction for a single row of tubes

N = the number of rows of tubes

β = the diameter-to-pitch ratio of the array

η_I = the de-entrainment fraction for a single tube (0.19 for cylindrical tubes and 0.27 for square tubes).

3.7.6 De-Entrainment at Area Changes

Droplets will de-entrain at restrictions in the flow path as a result of drop impingement on solid surfaces. This can be expected to occur as droplets formed during reflood flow through the upper tie plate, for example. Droplets that strike the solid portions of the tie plate de-entrain and provide the initial liquid for the top quench front. This type of de-entrainment is accounted for using a simple flow area ratio,

$$S_{DE} = (1 - A_1/A_2)\ \alpha_e \rho_\ell |u_e| A_2 \qquad (105)$$

where A_1 is the flow area in the restriction and A_2 is the flow area before the restriction.

3.7.7 De-Entrainment on Solid Surfaces and Liquid Pools

All entrained droplets flowing toward a horizontal solid surface, such as the top of the upper plenum, a containment floor or ceiling, or toward a liquid pool, are assumed to be de-entrained.

3.8 Fluid Thermodynamic Properties

Saturated and subcooled liquid viscosity, thermal conductivity, specific heat at constant pressure, Prandtl number and surface tension are obtained as functions of enthalpy from data tables. The tables are constructed in enthalpy increments of 10 Btu/lbm from results obtained with the WASP (Ref. 30) computer program. These tables are given in Appendix D.

3.8.1 Steam/Gas Transport Properties

Saturated and superheated steam viscosity and thermal conductivity for temperatures less than 815°C are computed as functions of enthalpy and density by the equations given in the 1967 ASME Steam Tables (Ref. 31). The expression for thermal conductivity is

$$k = k_1 + (103.51 + 0.4198\ T - 2.771(10)^{-5}T^2)\rho + 2.1482(10)^{14}\ \frac{\rho^2}{T^{4.2}} \qquad (106)$$

where

$$k_1 = 17.6 + 5.87(10)^{-2}\ T + 1.04(10)^{-4}\ T^2 - 4.51(10)^{-8}T^3 \qquad (107)$$

The viscosity is given by

$$\mu = \begin{cases} \mu_1 - \rho(1858 - 5.9T)\ , & \text{if } T < 340°C \\ \mu_1 + 353\ \rho + 676.5\ \rho^2 + 102.1\ \rho^3\ , & \text{if } T > 365°C \end{cases} \qquad (108)$$

$$\mu_1 = 0.407T + 80.4 \qquad (109)$$

For values of T between 340°C and 365°C the viscosity is interpolated between the values given by the two expressions in Equation 106. In Equations 106 through 109 temperature is in °C, density is in g/cm^3, thermal conductivity is in mW/m-°K, and viscosity is in micropoise. The viscosity is converted to lbm/ft-hr in the fluid property subroutine for use in the code.

Steam is treated as an ideal gas for temperatures greater than 815°C, and its thermal conductivity and viscosity above this temperature are calculated using the methods used for ideal gases that are described below.

The Lennard-Jones potential (Ref. 76) is used to calculate the pure gas transport properties. The gas viscosity is given by

$$\mu = 6.4572 \times 10^{-3}\ \sqrt{MT}/\sigma^2\ \Omega_\mu \qquad (110)$$

where

μ = gas viscosity (lbm/ft-hr)

M = molecular weight

T = gas temperature (K)

σ = zero energy collision diameter

Ω_μ = $f(k_B T/\epsilon)$

ϵ = maximum energy of attraction

k_B = Boltzmann constant.

The force constants σ and ϵ/K_B of the Lennard-Jones potential for each gas type is given in Table 3. A fit for the collision integral, Ω_μ, has been developed from the values given in Ref. 76. This fit is given by the following relationships:

$$x = \ell n\ (K_B T/\epsilon) \tag{111}$$

$$\Omega\ (k_B T/\epsilon) = 0.1549\ x^3 + 0.310X^2$$

$$- 0.7961\ x + 1.587 \qquad \frac{k_B T}{\epsilon} < 1.0 \tag{112}$$

$$= - 0.0565\ x^3 + 0.3305\ x^2 \qquad 1.0 < \frac{K_{BT}}{e} < 10.0$$
$$- 0.794\ x + 1.586$$

$$= 0.0083\ x^2 - 0.1596\ x$$
$$+ 1.1474 \qquad 10. < \frac{K_{BT}}{\epsilon} < 100.0$$

$$= - 0.08637\ x + 0.98595 \qquad 100 < \frac{K_B T}{\epsilon}$$

Table 3 Lennard-Jones Force Constants

Gas	$(A)^2$	(K)	Gas Type
Air	13.08	97.0	Polyatmoic (Ref. 77)
Argon	11.68	124.0	Monoatomic (Ref. 77)
Helium	6.636	10.2	Monoatomic (Ref. 77)
Hydrogen	8.497	38.0	Polyatomic (Ref. 77)
Krypton	12.24	225.0	Monoatomic (Ref. 77)
Nitrogen	13.55	91.5	Polyatomic (Ref. 77)
Oxygen	11.79	113.0	Polyatomic (Ref. 77)
Xenon	16.44	229.0	Monoatomic (Ref. 77)
Steam	6.975	809.1	Polyatomic (Ref. 78)

The thermal conductivity of a pure monatomic gas (Ref. 79) is:

$$k' = \frac{15}{4}\frac{\bar{R}}{M}\mu = 4.8191 \times 10^{-3} R \mu \qquad (113)$$

where k' = monoatomic thermal conductivity (Btu/hr-ft-°F)
$\bar{R}$ = universal gas constant
R = gas constant (ft-lbf/lbm-K)
μ = gas viscosity (lbm/ft- hr)

In polyatomic gases, additional energy moves by the diffusional transport of internal energy. This contribution to the total thermal conductivity is approximated by (Ref. 80):

$$k'' \simeq 0.88 \left(\frac{2}{5}\frac{C_p}{R} - 1\right) k' \qquad (114)$$

where k'' = internal thermal conductivity (Btu/hr-ft-°F)
C_p = constant pressure specific heat (Btu/lbm-R)
R = gas constant (Btu/lb- °R)
k' = monoatomic thermal conductivity (Btu/hr-ft-°F)

The viscosity of the gas mixture is calculated using the method of Wilke (Ref. 81) which is given by the approximate equation

$$\mu_{mix} = \sum_{i=1}^{N} \frac{\mu_i}{i + \sum_{\substack{j=1 \\ j=i}}^{N} \phi_{ij} \frac{X_j}{X_i}} \tag{115}$$

where μ = gas mixture viscosity (lbm/ft-hr)
μ_i = viscosities of the component gases
X_i and X_j = mole fractions of the component gases

The coefficients ϕ_{ij} are a function of vicosity and molecular-weight:

$$\phi_{ij} = \frac{[1 + (\mu_i/\mu_j)^{1/2} (M_j/M_i)^{1/4}]^2}{\sqrt{2} [1 + (M_i/M_j)]^{1/2}} \tag{116}$$

The identity

$$\phi_{ji} = \phi_{ij} k'_j/k'_i \tag{117}$$

is used to reduce the amount of computation required where k' and k' are the monotonic thermal conductivities of the component gases. j j

The monatomic conductivity of the gas mixture is calculated using Brokaw's method (Ref. 82) given by

$$k'_{mix} = \sum_{i=1}^{N} \frac{k'_i}{1 + \sum_{\substack{j=1 \\ j \neq i}}^{N} \Psi_{ij} X_j / X_i} \tag{118}$$

where k'_{mix} = monatomic thermal conductivity of the gas mixture (Btu/hr-ft-°F)

k'_i = monatomic thermal conductivity of the gas components.

The coefficients, Ψ_{ij}, are given as

$$\Psi_{ij} = \phi_{ij} \left[1 + 2.41 \frac{(M_i - M_j)(M_i - 0.142\, M_j)}{(M_i + M_j)^2}\right] \tag{119}$$

The formula for the internal thermal conductivity of a gas mixture developed by Hirschfelder (Ref. 83) is given by

$$k''_{mix} = \sum_{i=1}^{N} \frac{k''_i}{1 + \sum_{\substack{j=1 \\ j \neq i}}^{N} \phi_{ij} X_j / X_i} \tag{120}$$

where k''_{mix} = gas mixture internal thermal conductivity (Btu/hr-ft-°F)

k''_i = internal thermal conductivities of the gas components

ϕ_{ij} = same coefficient required for the mixture viscosity.

The total steam/gas mixture thermal conductivity is given as the sum of the monatomic and internal thermal conductivities:

$$k_{mix} = k'_{mix} + k''_{mix} \tag{121}$$

The above equations are approximations based on rigorous kinetic theory. They represent the best general methods now available for computing the transport properties of pure nonpolar gases. The mixture formulas should give approximately correct results for mixtures with traces of polar constituents.

Because steam is a highly polar molecule and may be in high concentrations for many applications in which COBRA-NC will be used, it should be expected that a certain error will result from use of these formulas. The lack of a better method for calculating the mixture properties makes this a necessary evil for now.

3.8.2 Thermodynamic Properties

Water saturation enthalpies are computed as functions of pressure from equations developed by Agee for EPRI (Ref. 32):

$$h_f = \sum_{n=1}^{9} A_{1,n} Y^{n-1} \qquad 0.1 < P < 898.7$$

$$h_f = \sum_{n=1}^{9} A_{2,n} Y^{n-1} \qquad 989.7 < P < 2529.9 \qquad (122)$$

$$h_f = \sum_{n=1}^{9} A_{3,n} Z^{n-1} \qquad 2529.9 < P < 3208.$$

$$h_g = \sum_{n=1}^{5} B_{1,n} Y^{n-1} + \sum_{n=6}^{8} B_{1,n} Y^{n+3} \qquad 0.1 < P < 1467.6$$

$$h_g = \sum_{n=1}^{9} B_{2,n} Y^{n-1} \qquad 1467.6 < P < 2586.0 \qquad (123)$$

$$h_g = \sum_{a\ n=1}^{7} B_{3,n} Z^{n-1} \qquad 2586 < P < 3208$$

where $Y = \ln(P)$

$Z = (3208.200000001 - P)^{0.41}$

The units of P are psia, and h is in Btu/lbm. The coefficients A and B are:

n	$A_{1,n}$	$A_{2,n}$	$A_{3,m}$
1	$0.6970887859(10)^{2}$	$0.8408618802(10)^{6}$	$0.9060030436(10)^{3}$
2	$0.3337529994(10)^{2}$	$0.2637413208(10)^{6}$	$-0.1426813520(10)^{2}$
3	$0.2318240735(10)^{1}$	$-0.4634506669(10)^{6}$	$0.1522233257(10)^{1}$
4	$0.1840599513(10)^{0}$	$0.1130306339(10)^{6}$	$-0.6973992961(10)^{0}$
5	$-0.5245502294(10)^{-2}$	$-0.4350217298(10)^{3}$	$0.1743091663(10)^{0}$
6	$0.2878007027(10)^{-2}$	$-0.3898988188(10)^{4}$	$-0.2319717696(10)^{-1}$
7	$0.1753652324(10)^{-2}$	$0.6697399434(10)^{3}$	$0.1694019149(10)^{-2}$
8	$-0.4334859620(10)^{-3}$	$-0.4730726377(10)^{2}$	$-0.6454771710(10)^{-4}$
9	$0.3325699282(10)^{-4}$	$0.1265125057(10)^{1}$	$0.1003003098(10)^{-5}$

n	$B_{1,n}$	$B_{2,n}$	$B_{3,n}$
1	$0.1105836875(10)^{4}$	$0.5918671729(10)^{6}$	$0.9059978254(10)^{3}$
2	$0.1436943768(10)^{2}$	$-0.2559433320(10)^{6}$	$0.5561957539(10)^{1}$
3	$0.8018288621(10)^{0}$	$0.3032474387(10)^{5}$	$0.3434189609(10)^{1}$
4	$0.1617232913(10)^{-1}$	$0.4109051958(10)^{1}$	$-0.6406390628(10)^{0}$
5	$-0.1501147505(10)^{-2}$	$0.3475066877(10)^{0}$	$0.5918579484(10)^{-1}$
6	$-0.1237675562(10)^{-4}$	$-0.3026047262(10)^{0}$	$-0.2725378570(10)^{-2}$
7	$0.3004773304(10)^{-5}$	$-0.1022018012(10)^{2}$	$0.5006336938(10)^{-4}$
8	$-0.2062390734(10)^{-6}$	$0.1591215116(10)^{1}$	0.0
9	0.0	$-0.6768383759(10)^{-1}$	0.0

The enthalpy of superheated vapor as a function of temperature and pressure is computed from equations given in Keenan and Keys' tables (Ref. 33) of 1936:

$$h = f(P,T)$$

$$= F_0 P + \frac{F_1}{2} + \frac{F_3}{4} + \frac{F_{12}}{13} p^{13} + F' \qquad (124)$$

To define F_0, F_1, F_3, and F_{12}, let

$$\tau = 1/T$$

$$B_0 = 1.80 - 2641.62\ \tau 10^{80870\tau^2}$$

$$B_1 = B_0^2\ (82.546\ \tau^2 - 1.6246(10)^5 \tau^3)$$

$$B_3 = B_0^4\ (0.21828\ \tau^3 - 1.2697(10)^5 \tau^5)$$

$$B_{12} = -B_0^{13}\ (3.635(10)^{-4} \tau^{12} - 6.768(10)^{64} \tau^{36}) \qquad (125)$$

Then the F_K are defined by

$$F_k = \frac{\partial}{\partial \tau}\ (B_k \tau)\ ,\ k = 0,1,3,12 \qquad (126)$$

The function F' is given by

$$F' = \int_{273.16}^{T} C_{p_o}\ dT + 2502.36 \qquad (127)$$

with

$$C_{p_o} = 1.4720 + 7.5566(10)^{-4}T + 47.8365\,\tau \qquad (128)$$

In Equations 124 through 128, T is in °K, P is in atmospheres, and h is in J/g. Equation 124 is used only for temperatures below 815°C.

Values for superheated vapor temperature are computed as functions of pressure and enthalpy using an iterative method described by McClintock and Silvestri (Ref. 34) for enthalpies below 1797 Btu/lbm. First, estimates for T and C_p are computed from the expressions

$$T = A_1 + A_2h + A_3h^2 + A_4h^3 + A_5P + A_6P^2$$

$$+ A_7P^3 + P(A_8h + A_9h^2 + A_{10}h^3) \qquad (129)$$

$$1/C_p = B_1 + B_2h + B_3h^2 + B_4h^3 + B_5 \ln P + B_6(\ln P)^2$$

$$+ B_7(\ln P)^3 + (\ln P)\,(B_8h + B_9h^2 + B_{10}h^3) \qquad (130)$$

where T is in °F, P is in psia, h is in Btu/lbm, and C_p is in Btu/lbm-°F.

When $P \leq 1000$ psia, or $P > 1000$ psia and $h \geq 1280$ Btu/lbm, the constants are

$A_1 = -1.0659659(10)^4$
$A_2 = 2.0110905(10)^1$
$A_3 = -1.250954(10)^{-2}$
$A_4 = 2.8274992(10)^{-6}$
$A_5 = 4.9815820$

$A_6 = -7.7618225(10)^{-6}$
$A_7 = 2.4391612(10)^{-10}$
$A_8 = -9.8147341(10)^{-3}$
$A_9 = 6.5824890(10)^{-6}$
$A_{10} = -1.4747938(10)^{-9}$
$B_1 = -2.8557816$
$B_2 = 1.3250230(10)^{-2}$
$B_3 = -1.0521514(10)^{-5}$
$B_4 = 2.5007955(10)^{-9}$
$B_5 = -3.4620214$
$B_6 = -3.6261637(10)^{-2}$
$B_7 = 7.3529479(10)^{-4}$
$B_8 = 5.7703098(10)^{-3}$
$B_9 = -2.9972073(10)^{-6}$
$B_{10} = 5.2037300(10)^{-10}$

Where $P > 1000$ psia and $h < 1280$ Btu/lbm, the constants are given by

$A_1 = -4.5298646(10)^{3}$
$A_2 = 1.5358850(10)^{1}$
$A_3 = -1.5655537(10)^{-2}$
$A_4 = 5.2687849(10)^{-6}$
$A_5 = 4.4185386(10)^{-1}$
$A_6 = -9.1654905(10)^{-6}$
$A_7 = 2.7549766(10)^{-10}$
$A_8 = -1.1541553(10)^{-3}$
$A_9 = 1.2384560(10)^{-6}$
$A_{10} = -4.1724604(10)^{-10}$
$B_1 = 1.2659960(10)^{2}$
$B_2 = -2.5611614(10)^{-1}$
$B_3 = 2.2270593(10)^{-4}$
$B_4 = -5.9928922(10)^{-8}$
$B_5 = -2.1818030(10)^{1}$
$B_6 = 1.3424036$

$$B_7 = -4.9110372(10)^{-2}$$
$$B_8 = 2.7966370(10)^{-2}$$
$$B_9 = -2.4665012(10)^{-5}$$
$$B_{10} = 6.7723080(10)^{-9}$$

The estimated temperature is then used to compute an approximate enthalpy from

$$h' = f(P,T) \tag{131}$$

where the function f(P,T) has been described by Equations 112 through 116. Next, a temperature correction, ΔT, is computed from

$$\Delta T = (1/C_p)\ (h - h') \tag{132}$$

and the new estimated temperature becomes

$$T' = T + \Delta T \tag{133}$$

A new approximate enthalpy, h", is computed using this temperature in Equation 131, and the iteration is continued until $(T - T') < 1.0°F$. Iteration is not used in the specific heat calculation. The C_p value given by Equation 130 is taken as the final value.

The specific heat of steam for enthalpies greater than 1797 Btu/lbm is assumed to be a function of temperature only. Polynomial fits to the data from (Ref. 78) for steam specific heats from 1500°F to 8540°F are given by the relationships:

$$C_p = -5.1039 \times 10^{-13}\ T^3 - 9.2456 \times 10^{-9}\ T^2 + 1.2324 \times 10^{-4}\ T + 0.398 \qquad 1500 < T < 3500°F \tag{134}$$

and

$$C_p = 4.7828 \times 10^{-13}\ T^3 - 1.1429 \times 10^{-8}\ T^2 + 1.0261 \times 10^{-4}\ T + 0.4563 \qquad 3500F \leq T \leq 8540°F$$

where

C_p is the specific heat in (Btu/lbm-°F).

The gas temperature is then calculated using an iterative algorithm. The specific heat is first calculated using the old time temperature. The error in the new time temperature is then estimated from the relationship

$$T_{i+1} - T^n - \frac{1}{C_p} (h^{n+1} - h^n) = E \tag{135}$$

The linear variation of this error with respect to the temperature is

$$\frac{\partial E}{\partial T} = 1 - \frac{1}{C_p^2} (h^{n+1} - h^n) \frac{\partial C_p}{\partial T} \tag{136}$$

The linear variation in vapor temperature required to reduce this error to zero is given by

$$\delta T = \frac{- E}{\frac{\partial E}{\partial T}} \tag{137}$$

Then, the new iterate value for the vapor temperature is

$$T^{i+1} = T^i + \delta T \tag{138}$$

The specific heat is then recalculated using T^{i+1} and the error in vapor temperature is re-evaluated. This iteration continues until the change in temperature is less than 0.1°F. The new time specific heat is then calculated as

$$C_p = 0.5\ (C_p^{\,i+1} + C_p^{\,n}) \tag{139}$$

The new time temperature is then calculated as

$$T^{n+1} = T^n + \frac{1}{C_p}\ (h^{n+1} - h^n) \tag{140}$$

The specific heat for each component of the noncondensable gas mixture is computed using polynomial fits to data and the temperature of the vapor calculated using one of the two methods described above. The polynomial equations for the specific heat of each gas component are

Air

$$C_p = 0.24439 - 4.2042 \times 10^{-5}\ T + 9.6113 \times 10^{-8}\ T^2 - 1.1638 \times 10^{-11}\ T^3 \qquad T < 600\ K \tag{141}$$

$$C_p = 0.20883 + 7.7103 \times 10^{-5}\ T - 8.5673 \times 10^{-9}\ T^2 - 4.7577 \times 10^{-12}\ T^3 \qquad 600\ K \leq T < 1500\ K \tag{142}$$

Argon

$$C_p = 0.12428 \qquad T \leq 6000\ K \tag{143}$$

Helium

$$C_p = 1.2404 \qquad T \leq 6000\ K \qquad (144)$$

Hydrogen

$$C_p = 1.46910 + 1.60057 \times 10^{-2}\ T - 4.4405 \times 10^{-5}\ T^2 + 4.2122 \times 10^{-8}\ T^3 \qquad T < 400\ K \qquad (145)$$

$$C_p = 3.569 - 4.896 \times 10^{-3}\ T + 6.225 \times 10^{-7}\ T^2 - 1.1969 \times 10^{-10}\ T^3 \qquad 400\ K \leq T < 1500\ K \qquad (146)$$

$$C_p = 2.9187 + 7.3292 \times 10^{-4}\ T - 8.3631 \times 10^{-8}\ T^2 - 3.3863 \times 10^{-13}\ T^3 \qquad 1500\ K \leq T < 2500\ K \qquad (147)$$

$$C_p = 2.9405 + 7.8905 \times 10^{-4}\ T - 1.3215 \times 10^{-7}\ T^2 + 8.6861 \times 10^{-12}\ T^3 \qquad 2500 \leq T \leq 5000\ K \qquad (148)$$

Krypton

$$C_p = 0.05911 \qquad T \leq 6000\ K \qquad (149)$$

Nitrogen

$$C_p = 0.2599 - 8.4212 \times 10^{-5}\ T + 1.7212 \times 10^{-7}\ T^2 - 6.7294 \times 10^{-11}\ T^3 \qquad T < 775\ K \qquad (150)$$

$$C_p = 0.2017 + 1.0801 \times 10^{-4}\ T \qquad 775\ K \leq T \leq 1500\ K$$

$$- 3.3221 \times 10^{-8} T^2$$

$$+ 2.4523 \times 10^{-12} T^3 \qquad (151)$$

Oxygen

$$C_p = 0.2221 - 7.692 \times 10^{-5} T \qquad T < 760 \text{ K}$$

$$+ 2.7876 \times 10^{-7} T^2$$

$$- 1.7011 \times 10^{-10} T^3 \qquad (152)$$

$$C_p = 0.1771 + 1.4951 \times 10^{-4} T \qquad 760 \text{ K} \leq T \leq 1500 \text{ K}$$

$$- 8.4494 \times 10^{-8} T^2$$

$$+ 1.8324 \times 10^{-11} T^3 \qquad (153)$$

Xenon

$$C_p = 0.03791 \qquad T \leq 6000 \text{ K} \qquad (154)$$

The noncondensable gas mixture enthalpy is calculated from the relationship

$$h^{n+1} = h^n + C_{p_{mg}} (T^{n+1} - T^n)$$

The density of the noncondensable gas mixture is calculated from the equations of state for an ideal gas:

$$\rho_{mg} = \frac{n_{mg}}{R_{mg} T^{n+1}} \qquad (155)$$

The gas constant and specific heat for the noncondensable gas mixture are calculated using a mass fraction weighting of the component gases:

$$R_{mg} = \sum_{i=1}^{N} m_{f_i} R_i \tag{156}$$

$$C_{P_{mg}} = \sum_{i=1}^{N} m_{f_i} C_{P_i} \tag{157}$$

Liquid and vapor specific volumes as functions of pressure and enthalpy are computed using equations from Reference 33. For the vapor,

$$v = E_1 + E_2 P + E_3/P + E_4 h + E_5 Ph + E_6 h/P \tag{158}$$

and for the liquid,

$$v = \exp \left\{ \sum_{k=0}^{4} \sum_{n=0}^{2} C_{k,n} P^n h^k \right\} \tag{159}$$

where P is in psia, h is in Btu/lbm, and v is in ft^3/lbm. The constants for these equations are

$$E_1 = -0.81735849(10)^{-3}$$
$$E_2 = 0.12378514(10)^{-4}$$
$$E_3 = -0.10339904(10)^{4}$$
$$E_4 = -0.62941689(10)^{-5}$$
$$E_5 = -0.87292160(10)^{-8}$$
$$E_6 = 0.12460225(10)^{1}$$

$$C_{0,0} = -0.41345(10)^{1} \quad C_{0,1} = -0.59428(10)^{-5} \quad C_{0,2} = 0.15681(10)^{-8}$$
$$C_{1,0} = 0.13252(10)^{-4} \quad C_{1,1} = 0.63377(10)^{-7} \quad C_{1,2} = -0.40711(10)^{-10}$$
$$C_{2,0} = 0.15812(10)^{-5} \quad C_{2,1} = -0.39974(10)^{-9} \quad C_{2,2} = 0.25401(10)^{-12}$$

$$C_{3,0} = 0.21959(10)^{-8} \quad C_{3,1} = 0.69391(10)^{-12} \quad C_{3,2} = -0.52372(10)^{-15}$$
$$C_{4,0} = 0.21683(10)^{-11} \quad C_{4,1} = -0.36159(10)^{-15} \quad C_{4,2} = 0.32503(10)^{-18}$$

4.0 HEAT TRANSFER MODELS

The heat transfer models in COBRA-NC determine the material heat release rates and temperature response of the fuel rods and structural components of a light water reactor during operating and transient conditions and the heat transfer to or from containment structures during transients. All of the heat transfer calculations are performed at the beginning of each time step before the hydrodynamic solution. Heat transfer coefficients based on old time fluid conditions are used to advance the material conduction solution. The resultant heat release rates are explicitly coupled to the hydrodynamic solution as source terms in the fluid energy equations.

To effectively perform these tasks, a consistent set of heat transfer models was developed. It consists of five components:

- CONDUCTION MODEL — specifies the conductor geometry and material properties, and solves the conduction equation
- HEAT TRANSFER PACKAGE — selects and evaluates the appropriate heat transfer correlations
- QUENCH FRONT MODEL — a "fine mesh-rezoning" method that calculates quench front propagation due to axial conduction and radial heat transfer
- GAP CONDUCTANCE MODEL — a dynamic gap conductance model that evaluates fuel pellet-clad conductance for a nuclear fuel rod. (Ref. 35, 36, and 37).
- CLAD OXIDATION MODEL — A zircaloy cladding oxidation model that calculates the heat source, hydrogen generation rate and steam consumption rate due to the metal/water reaction.

4.1 Conduction Models

The rod model is designed for nuclear fuel rods, heater rods, tubes, and walls. These options allow the user to simulate most of the conductor geometries found in reactor vessels and heat transfer experiments. In addition, an unheated conductor model is provided for structural heat transfer surfaces within a reactor primary system or within the containment building.

4.1.1 Conductor Geometry

A nuclear fuel rod model requiring minimal user input is built into the code. Material properties can be specified by input or defaulted to uranium-dioxide and zircaloy. These properties are calculated using correlations from MATPRO-11 (Revision 1) (Ref. 38). The conductor geometry for a nuclear fuel rod is

illustrated in Figure 9. Only cylindrical fuel rods with fluid thermal connections on the rod exterior are considered by this model.

A dynamic gap conductance model based on the GAPCON (Ref. 37,39) and FRAP (Ref. 36,40,41) computer codes is available for use with the nuclear fuel rod model. This is discussed in Section 4.4. Alternatively, the user may specify gap conductance by input, either as a constant or with axial and temporal variations using input forcing functions. (The gap conductance options are available only with the nuclear fuel rod model.)

Electric heater rods used as fuel pin simulators and other solid cylinders can be modeled with the heater rod option. These rods consist of concentric rings of different material regions, as shown in Figure 10. In each region the material type, number of radial nodes, width, and power factor are specified by input. Contact resistances are not calculated between material regions but can be modeled by including a region one node wide with material properties that give it the appropriate thermal resistance.

Conductors, either tube or plate, with thermal connections to channels on either the inner or the outer surface are modeled by the tube and wall models. These geometries, shown in Figure 11, are similar to the heater rod model except for the interior coolant connections. Concentric and flat plate fuel elements, thermal walls, and simple tubes can be modeled with these options. Each rod may extend through any number of channel-splitting sections, but

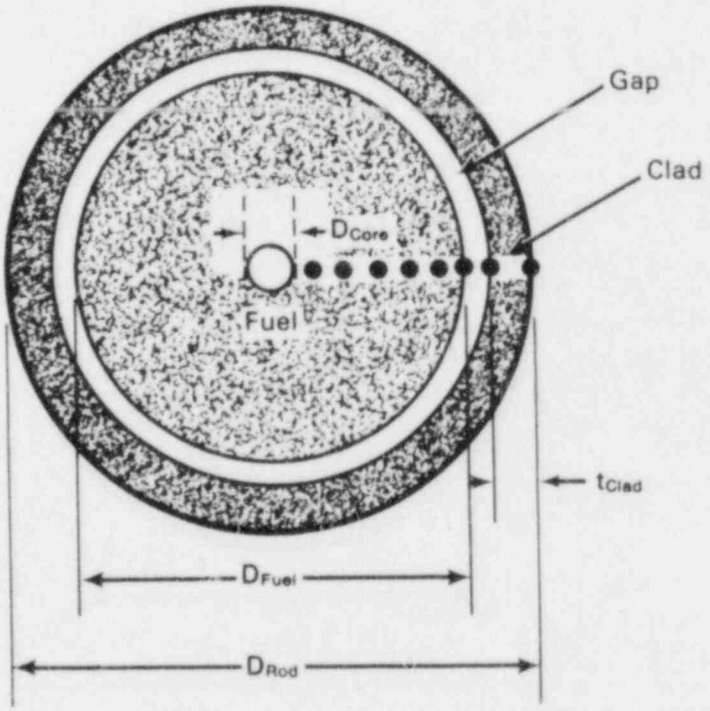

Figure 9 Nuclear fuel rod geometry

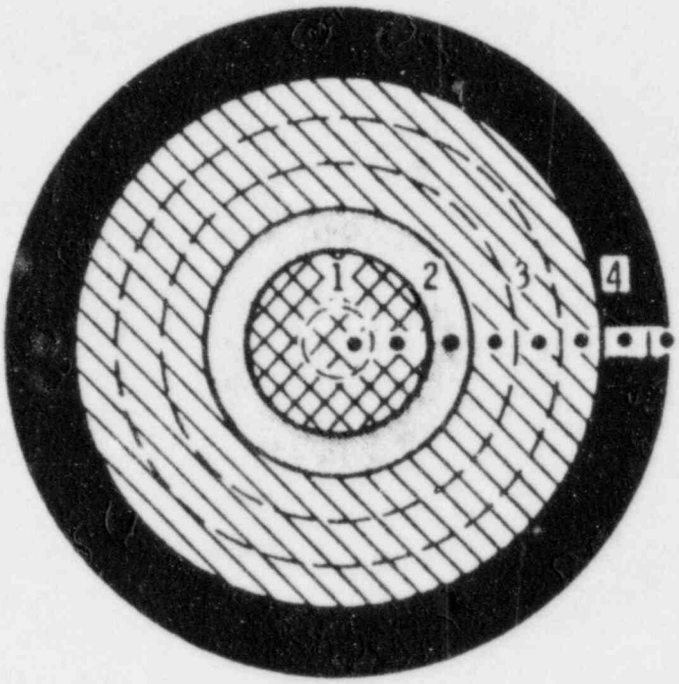

Figure 10 Heater rod geometry (example of a fuel pin simulator)

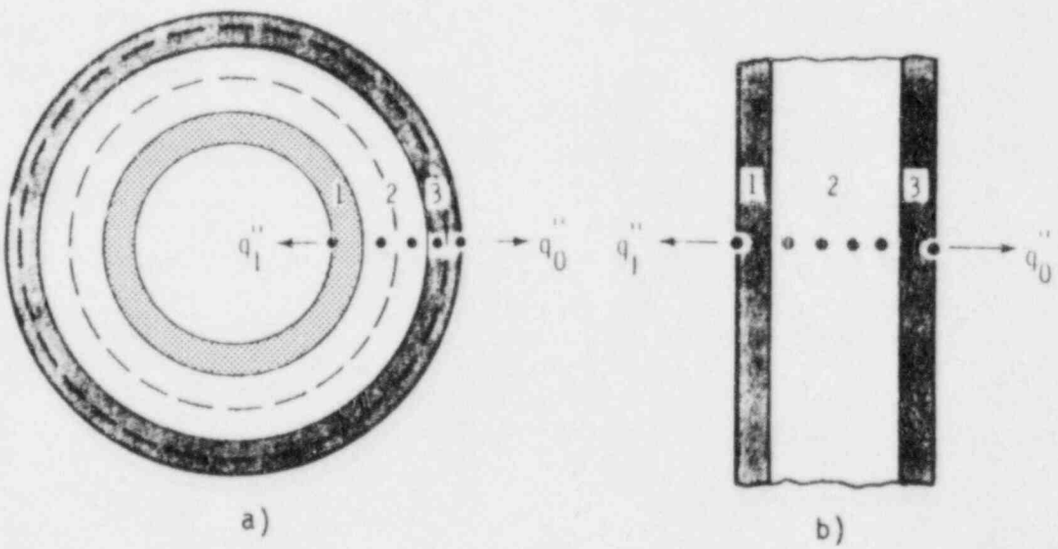

Figure 11 Tube and wall conductor geometries

each heat transfer surface may be connected to only one channel in each section. Detailed discussions of how to use these models for specific problems and the definition of a section are included in the User's Manual, Volume 3.

4.1.2 Unheated Conductor Model

Structural heat transfer surfaces can be more efficiently modeled with the unheated conductor model. This option accesses the same conductor geometries (except for the nuclear fuel rod geometry) as the rod model, and uses the same heat transfer package. However, to economize computer time and storage, the unheated conductor model is limited in the following ways:

- No internal heat generation is included.
- Radial conduction only is used.
- No fine mesh-rezoning quench front model is included.
- Unheated conductors do not extend across section boundaries.
- The fluid solution cannot be forced into the "hot wall" flow regime.
- Vapor properties in the convective heat transfer correlations are evaluated at the bulk vapor temperature rather than at the film temperature.
- The minimum film boiling temperature is set to a constant 900°F.

These limitations apply only to the unheated conductor model and not to the rod model in general. Unheated conductors should be used to model structural elements for which expected peak temperatures are well below the minimum film boiling point. They are generally used to model vessel walls, plates, support columns, and other structures in reactor vessels. They are also used to model metal and concrete structural surfaces in containments.

4.1.3 Conduction Equation

The heat transfer model includes the ability to simulate generalized conductor geometries (fuel rods, electric heater rods, tubes, and walls) and temperature-dependent material properties. To accomplish this, a finite-difference form of the conduction equation has been employed. The difference equations are formulated using the "heat balance" approach (Ref. 43), which easily accommodates the following features:

- unequal mesh spacing
- temperature-dependent material properties
- space-dependent material properties

- internal resistances (such as those due to gaps)
- radial heat generation profiles.

The finite-difference nodes of the conduction equation are modeled as control volumes connected by thermal resistances. They form a set of linearized equations solved by Gaussian elimination and back-substitution.

The radial conduction equation for a control volume can be derived from a simple heat balance. For node i of Figure 12 this is

$$(\rho C_p V)_i \frac{\partial T_i}{\partial t} = - Q_{i,i-1} - Q_{i,i+1} + Q_i''' V_i \qquad (160)$$

where ρ = density (lbm/ft^3)

C_p = specific heat ($Btu/lbm-\ ^\circ F$)

V = node volume (ft^3)

T = node temperature ($^\circ F$)

$Q_{i,i-1}$ = radial heat flow from node (i) to (i-1) (Btu/sec)

$Q_{i,i+1}$ = radial heat flow from node (i) to (i+1) (Btu/sec)

Q_i''' = volumetric heat generation rate ($Btu/sec-\ ft^3$)

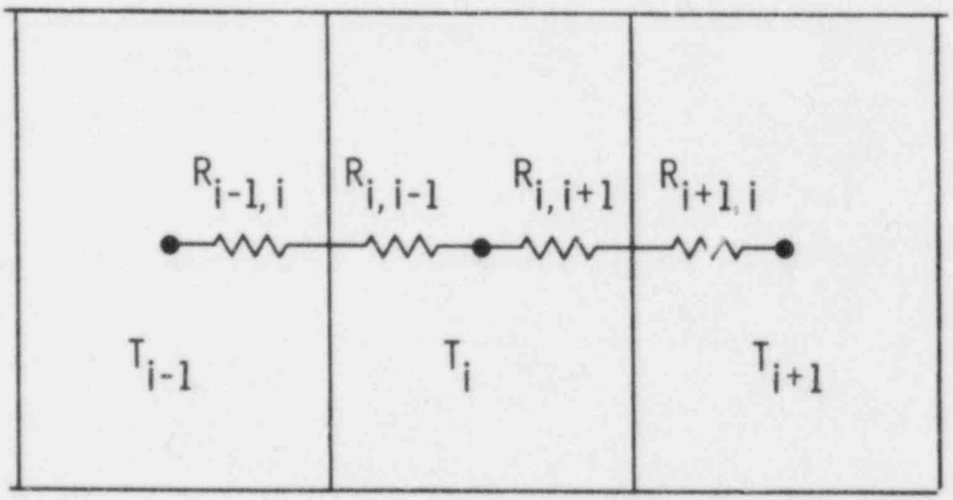

Figure 12 Heat balance control volume

The locations of radial conduction nodes are automatically calculated for a conductor geometry type. Each material region is divided into a specified number of subregions of equal radial thickness, and a conduction node is located at the center of mass of each subregion. This rule is followed for all nodes except

- the node at the inside and outside surface of a "TUBE" or "WALL"
- the outside surface of a heater rod
- the fuel pellet exterior, cladding interior, and cladding exterior surface for a nuclear fuel rod.

For these surfaces, a subregion half as wide as the other subregions is defined, and the node is located on the surface. The noding within a nuclear fuel rod is illustrated in Figure 13. (The fuel centerline temperature is calculated by Hermite interpolation.)

The radial positions of the conduction nodes are fixed; relocation due to thermal expansion is not calculated. To prevent an apparent loss of mass from the conductor because of density change with temperature, the term ρv is evaluated at the cold state density and dimensions, and defines the mass M_i associated with node i. Hence Equation 168 becomes

$$(MC_p)_i \frac{\partial T_i}{\partial t} = - Q_{i,i-1} - Q_{i,i+1} + Q'''_i V_i \qquad (161)$$

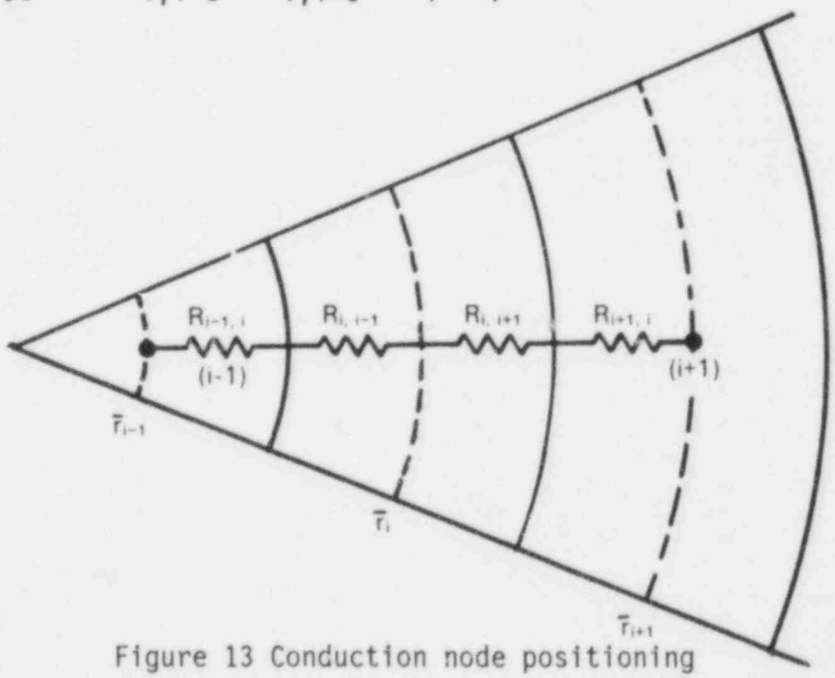

Figure 13 Conduction node positioning

Heat transfer through a node is computed from the conductance, K, of the material and the temperature gradient across the node as

$$Q_{i,j} = - K_{i,j} (T_j - T_i)$$

and

$$K_{i,j} = K_{j,i} \quad \text{for } j = \begin{cases} i-1 \\ i+1 \end{cases}$$

The conductance is simply the inverse of the thermal resistance, R, between nodes and is computed as

$$K_{i,k-1} = 1/(R_{i,i-1} + R_{i-1,i}) \tag{162}$$

Thermal resistances are calculated for each node as a function of geometry and thermal conductivity. (See Appendix C for a complete explanation of this procedure.)

Substituting Equation 159 into 158 gives

$$(MC_p)_i \frac{\partial T_i}{\partial t} = K_{i,i-1} (T_{i-1} - T_i) + K_{i,i+1} (T_{i+1} - T_i) + Q'''_i V_i \tag{163}$$

Forward differencing the temporal derivative in Equation 161 yields

$$\frac{(MC_p)_i}{\Delta t}(T_i - T_i^n) = K_{i,i-1}(T_{i-1} - T_i) + K_{i,i+1}(T_{i+1} - T_i) + Q_i''' V_i \quad (164)$$

where Δt = time increment
n = old time level (all other temperatures are at the new time level).

To solve this equation, an implicit formulation is applied in the radial direction and the equation solved by Gaussian elimination for all nodes at that axial level. Axial conduction, if used, is treated as an explicit source term. The finite-difference equation for node (i) is then

$$\frac{(MC_p)_i}{\Delta t}(T_i - T_i^n) = K_{i,i-1}(T_{i-1} - T_i) + K_{i,i+1}(T_{i+1} - T_i)$$

$$+ K_{i,j-1}(T_{j-1}^n - T_i^n) + K_{i,j+1}(T_{j+1}^n - T_i^n)$$

$$+ Q_i''' V_i \quad (165)$$

where the subscripts (j+1) and (j-1) represent the nodes at the same radial location and immediately above and below node i. If the stability criterion for the explicit axial conduction is exceeded, the time step used in the conduction equation is divided into two or more smaller time steps and the conduction equation is solved for each of these.

Variations of Equation 165 are defined for the boundary nodes. The boundary condition applied to the conduction equation can be adiabatic or a surface heat transfer coefficient. Adiabatic boundary conditions are assigned to the center nodes of solid cylindrical rods (nuclear and heater rods) and at any surface

node not connected to the fluid. Heat transfer coefficient boundary conditions are applied at surfaces connected to the fluid.

The heat transfer surface is coupled to the fluid channel through the heat transfer coefficient boundary condition. For each surface heat transfer node, both a heat transfer coefficient and a fluid sink temperature are specified for each phase of the fluid. Thus, the rod heat flux is given by

$$q'' = H_\ell \, (T_s - T_\ell^n) + H_{vg} \, (T_s - T_{vg}^n) \tag{166}$$

The fraction of the rod surface area in contact with a given phase is accounted for in the heat transfer coefficient (e.g., $H_v = 0$ for annular flow).

The nucleate boiling heat flux depends very strongly on the wall surface temperature. Because the wall temperature is in turn affected strongly by the heat flux, the surface temperature solution may oscillate in nucleate boiling unless the heat transfer and wall temperature solution are coupled implicitly. This is done non-iteratively by including the "linearized" derivative of the heat transfer coefficient with respect to temperature in the surface boundary condition. Therefore, the heat flux from the surface to phase is given by

$$q''_\ell = H_\ell \, (T_s - T_\ell^n) + \left(\ell \frac{\partial H_\ell}{\partial T_s}\right) (T_s - T_s^n) \, (T_s^n - T_\ell^n) \tag{167}$$

Rewriting Equation 165 for a surface node (s):

$$\begin{aligned} \frac{(MC_p)_s}{\Delta t} \, (T_s - T_s^n) = {} & K_{s,s-1} \, (T_{s-1} - T_s) + K_{s,j+1} \, (T_{j+1}^n - T_s^n) \\ & + K_{s,j+1} \, (T_{j+1}^n - T_i^n) \\ & - A_s \left[H_\ell (T_s - T_\ell^n) + \frac{\partial H_\ell}{\partial T_s} \, (T_s - T_s^n)(T_s^n - T_\ell^n)\right] \\ & - A_s \, H_v \, (T_s - T_v^n) + Q_s''' \, V_s \end{aligned} \tag{168}$$

where A_s is the heated surface area.

Equation 168 is solved simultaneously with a set of equations for the interior nodes to determine the new time temperatures. The amount of heat transferred to each phase of the fluid during the time step is back-calculated after the conduction equation is solved, as follows:

$$Q_\ell = \left[H_\ell (T_s - T_\ell^n) + \frac{\partial H_\ell}{\partial T_s} (T_s - T_s^n)(T_s^n - T_\ell^n)\right] A_s$$

$$Q_v = H_{vg} (T_s - T_{vg}^n) A_s \qquad (169)$$

4.2 Heat Transfer Package

The heat transfer package consists of a library of heat transfer correlations and a selection logic algorithm. Together these produce a continuous boiling curve that is used to determine the phasic heat fluxes. A schematic of the boiling curve shown in Figure 14 and 15 illustrate the heat transfer regime selection logic. The correlations used in each regime are detailed below.

4.2.1 Single-Phase Vapor

The Dittus-Boelter (Ref. 15) and the ORNL (Ref. 44) convection and heat transfer correlations are used to model heat transfer to the single-phase vapor/gas mixture.

The ORNL correlation is based on a modified wall Reynolds number:

$$Re_{mw} = \frac{G_{vg} D_H}{\mu_w} \left(\frac{\rho_w}{\rho_{vg}}\right) \qquad (170)$$

The heat transfer correlation is

$$HTC = 0.021 \, Re_{mw}^{0.8} \, Pr_w^{0.4} \, \frac{k_{vg_w}}{D_H} \qquad (171)$$

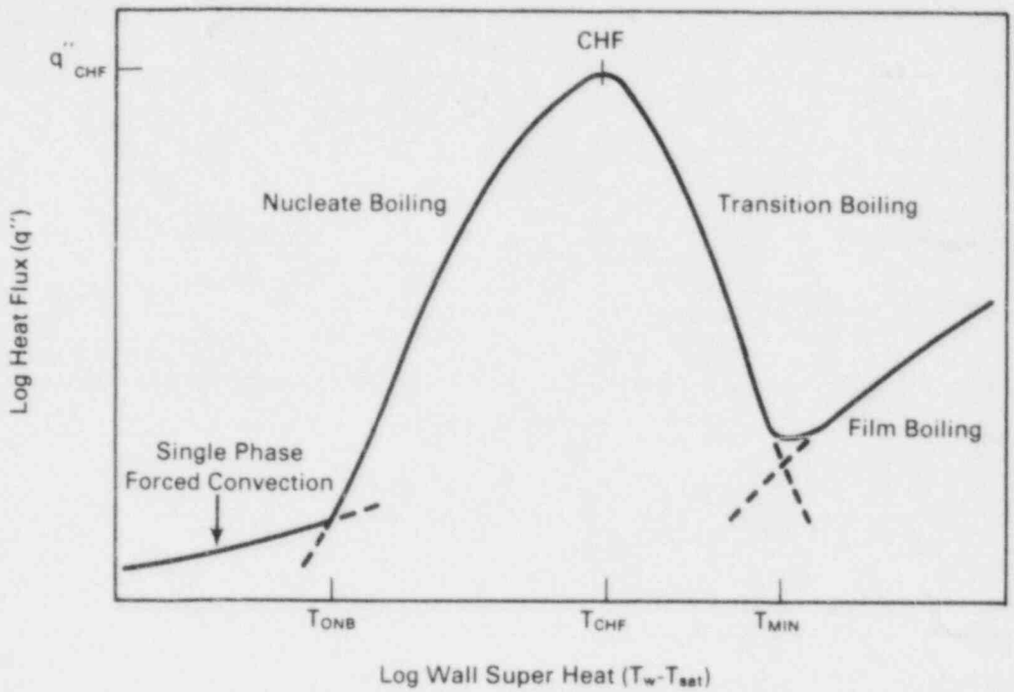

Figure 14 Schematic representation of the boiling curve

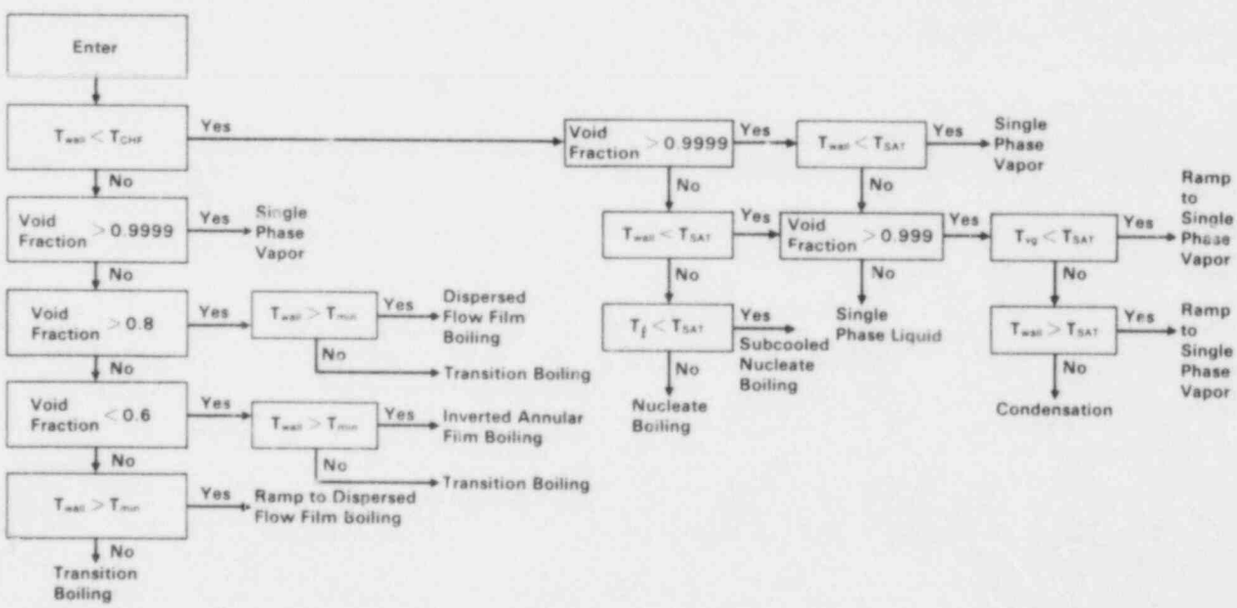

Figure 15 Heat transfer regime selection logic

The fluid properties in both Equations 170 and 171 are evaluated at the wall temperature. The vapor/gas density in Equation 170 is evaluated at the bulk temperature. All other properties are those of the vapor/gas mixture at the wall temperature. Equation 171 is limited to a minimum value of

$$N_{u_w} = 3.66\ Pr_w^{0.4} .$$

The Dittus-Boelter correlation is used for modified wall Reynolds numbers greater than 1000

$$HTC = 0.023 \left(\frac{G_{vg}\ D_H}{\mu_{vg}}\right)^{0.8} (Pr_{vg})^{0.4} \frac{K_{vg}}{D_H} \qquad (172)$$

The vapor/gas mixture properties are evaluated at the bulk fluid temperature.

If the heat transfer surface temperature is below the saturation temperature and steam is available, then condensation is assumed to occur. The condensation heat transfer coefficient is assumed to be the maximum of the convection heat transfer coefficient given above and the Uchida correlation (Ref. 84):

$$H_{UC} = 79.33 \left(\frac{\rho_v}{\rho_g}\right)^{0.8} \qquad (173)$$

The upper limit on H_{UC} is 280.0 Btu/hr-ft^2-°F and the lower limit is 0.0. The condensation heat flux to the heat transfer surface is calculated using the temperature difference between the wall and saturation:

$$q''_{cond} = H_{cond} (T_{wall} - T_g) \qquad (174)$$

The condensation heat flux is used to calculate an e plicit condensation rate given by the expression

$$\Gamma_{con} = \frac{-q_{cond}}{(h_v - h_f)} \tag{175}$$

The amount of heat removed from the vapor phase during the condensation process is equal to $\Gamma_{cond}\ h_v$ while $-\Gamma_{con}\ h_f$ is added to the liquid phase. (Also, Γ_{cond} lbm/sec of steam mass is removed from the vapor phase and added to the liquid phase.) Thus, the net heat removed from the fluid is equal to the heat added to the solid surface

$$\Gamma_{cond}\ (h_v - h_f) = h_{cond} A\ (T_w - T_s) \tag{176}$$

This amount of heat is deposited into the surface heat transfer node as an energy source, and both the vapor and liquid heat transfer coefficients are set to zero.

This method allows the code to calculate the condensation of steam on cold surfaces when the bulk steam temperature is superheated without desuperheating the uncondensed vapor. The condensation heat flux is ramped to zero once sufficient condensation has occurred to form a liquid film on the heat transfer surface. Heat transfer is then calculated between the superheated vapor and the liquid film and the liquid film and the heat transfer surface after this point.

4.2.2 Single-Phase Liquid

Convection to single-phase liquid is computed as the largest of either the Dittus-Boelter turbulent convection correlation, laminar flow with a Nusselt number equal to 7.86 (Ref. 45), or conduction through a liquid film.

- Dittus-Boelter (liquid)

$$HTC = 0.023\ \frac{k_\ell}{D_H}\ \left(\frac{G_\ell\ D_H}{\mu_\ell}\right)^{0.8}\ (Pr_\ell)^{0.4} \tag{177}$$

- Laminar

$$HTC = 7.86 \frac{k_\ell}{D_H} \tag{178}$$

- Conduction through liquid film

$$HTC = 2.0\ k_\ell/\delta \text{ where } \delta = \max\left(0.0013 \text{ ft}, \frac{\alpha_\ell D_H}{4}\right) \tag{179}$$

4.2.3 Nucleate Boiling

When the wall temperature is greater than saturation but less than the critical heat flux temperature and liquid is present, the Chen (Ref. 46) nucleate boiling correlation is used. The Chen correlation applies to both the saturated nucleate boiling region and the two- phase forced convection evaporation region. It automatically makes the transition to single-phase convection at low wall superheat and pool boiling at low flow rate. Chen assumes a superposition of a forced-convection correlation (Dittus-Boelter type) and a pool boiling equation (Forster-Zuber). Thus,

$$H_{CHEN} = H_{SPL} + H_{NB}$$

$$\text{where} \quad H_{SPL} = 0.023\ F\ \left(\frac{k_f}{D_H}\right)\ Re^{0.8}\ Pr^{0.4} \tag{180}$$

F = Reynolds number factor (Figure 16)

Re = Reynolds number = $\dfrac{(1-x)\ G\ D_H}{\mu_f}$

Pr = Prandtl number

and

$$H_{NB} = 0.00122\ S\ \left[\frac{k_f^{0.79} Cp_f^{0.45} \rho_f^{0.49} g_c^{0.25}}{\sigma^{0.5} \mu_f^{0.29} h_{fg}^{0.24} \rho_g^{0.24}}\right] (T_w - T_f)^{0.24} (P_w - P)^{0.75} \quad (181)$$

where S = suppression factor (Figure 17)
T_w = wall surface temperature
P_w^w = saturation pressure corresponding to T_w (lbf/ft^3).

All fluid properties are those for steam and water evaluated at saturation conditions for the total pressure. Butterworth developed curve fits for both the Reynolds number factor (F) and the suppression factor[a] (S) as follows (Ref. 47):

$$F = \begin{cases} 1.0 & ; \chi_{tt}^{-1} < 0.1 \\ 2.34\ (\chi_{tt}^{-1} + 0.213)^{0.736} & ; \chi_{tt}^{-1} > 0.1 \end{cases} \quad (182)$$

where χ_{tt}^{-1} = inverse Martinelli factor

$$\chi_{tt}^{-1} = \left(\frac{x}{1-x}\right)^{0.9} \left(\frac{\rho_f}{\rho_g}\right)^{0.5} \left(\frac{\mu_g}{\mu_f}\right)^{0.1} \quad (183)$$

The quality x, used in Equation 183 is the minimum of the following quality and the thermodynamic quality for the vapor/gas and water mixture.

$$S = \begin{cases} [1 + 0.12\ (Re'_{TP})^{1.14}]^{-1} & ; Re'_{TP} < 32.5 \\ [1 + 0.42\ (Re'_{TP})^{0.78}]^{-1} & ; 32.5 < Re'_{TP} < 50.9 \\ 0.1 & ; Re'_{TP} > 50.9 \end{cases} \quad (184)$$

(a) Reynolds number limit modified from original 70 to be continuous

where $Re'_{TP} = (1 \times 10^{-4})\ Re\ F^{1.25}$ (185)

These factors are illustrated graphically in Figures 16 and 17.

4.2.4 Subcooled Nucleate Boiling

The Chen correlation, although developed for saturated boiling, may be extended into the subcooled region. As discussed in the saturated boiling section, the Chen correlation superimposes a forced convective and nucleate boiling component. For subcooled boiling,

$$q'' = q''_{FC} + q''_{NB} \tag{186}$$

The nucleate boiling heat flux is evaluated as

$$q''_{NB} = H_{NB}\ (T_w - T_f) \tag{187}$$

where H_{NB} is defined by Equation 181 above, and the suppression factor, S, is computed from Equation 184 using the single-phase Reynolds number $Re = G_\ell D_H/\mu_\ell$. The forced convection heat flux is computed from Equation 180 using subcooled liquid properties and setting the flow factor, F, to unity, so that

$$q''_{FC} = 0.023\ \left(\frac{k_\ell}{D_H}\right)\ Re^{0.8}\ Pr^{0.4}\ (T_w - T_\ell) \tag{188}$$

where $Re = \dfrac{G_\ell D_H}{\mu_\ell}$

T_ℓ = local bulk fluid temperature

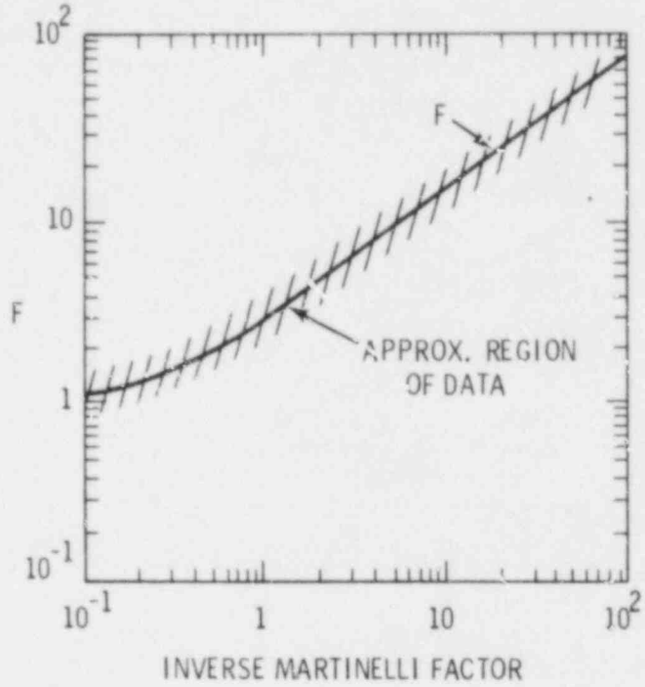

Figure 16 Reynolds number factor, F, for Chen correlation

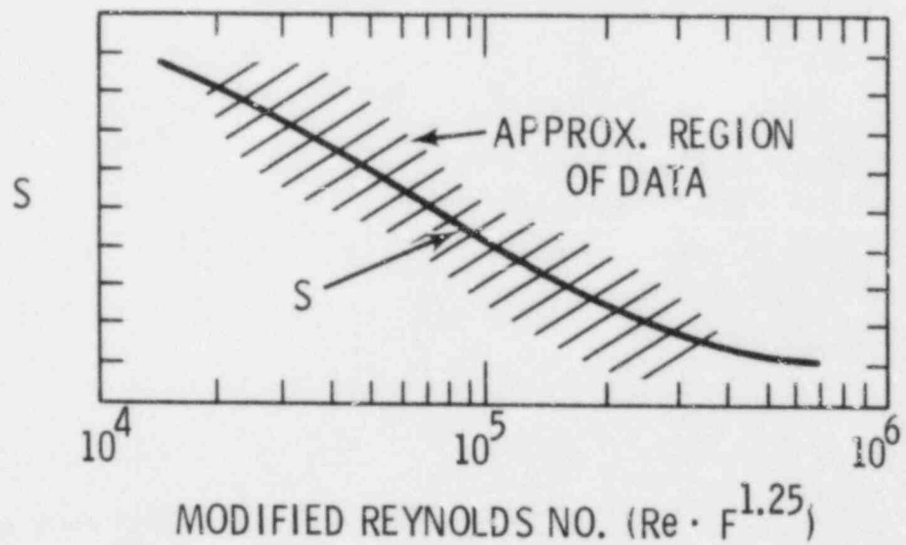

Figure 17 Suppression factor, S, for Chen correlation

Moles and Shaw (Ref. 48) compared the Chen correlation to subcooled boiling data for several fluids and reported satisfactory agreement for water at low to moderate subcoolings.

During subcooled boiling, vapor generation occurs and a significant void fraction (α~0.6) may exist despite the presence of subcooled water. In this regime, four processes are of interest:

- forced convection to liquid
- vapor generation at the wall
- condensation near the wall
- bulk condensation (subcooled liquid core).

Condensation occurring because of the presence of vapor in the subcooled liquid core is calculated implicitly during the solution of the energy equations and does not affect the determination of phasic heat inputs. Forced convection to liquid is treated using Equation 186 and the heat input to the liquid energy equation. The nucleate boiling component of the Chen correlation (Equation 185) defines the amount of heat available to cause vapor generation at the wall.

The near-wall condensation is estimated using the Hancox-Nicoll (Ref. 49) correlation for heat flux at the point where all the bubbles generated collapse in the near-wall region:

$$q''_{HN} = 0.4 \left[\frac{C_{p_f} \mu_f}{D_H}\right] \left[\frac{G D_H}{\mu_f}\right]^{0.662} (T_f - T_\ell) \qquad (189)$$

where T_f = saturation temperature for total pressure
T_ℓ = subcooled liquid temperature.

The heat flux dissipated in near-wall condensation is calculated as

$$q''_c = \text{MAXIMUM}\ (0.0,\ q''_{HN} - q''_{SPL}) \qquad (190)$$

Subtracting the near-wall condensation from the amount available for vapor generation yields

$$Q_\Gamma = (q''_{NB} - q''_c)\ A_H \tag{191}$$

However, a fraction of Q_Γ is expended to heat up the subcooled liquid "pumped" into the saturated thermal boundary layer. This fraction is given by the Rouhani (Ref. 50) model:

$$\epsilon_p = \frac{(\rho_f/\rho_g)\ (h_f - h_\ell)}{h_{fg} + (\rho_f/\rho_g)\ (h_f - h_\ell)} \tag{192}$$

and

$$\epsilon_\Gamma = (1 - \epsilon_p) = \frac{h_{fg}}{h_{fg} + (\rho_f/\rho_g)(h_f - h_\ell)} \tag{193}$$

where ϵ_p = fraction of heat to boundary layer
ϵ_Γ = fraction of heat causing vapor generation

and all fluid saturation properties are evaluated at the total pressure. Finally, the amount of vapor generation is

$$Q_\Gamma = (q''_{NB} - q''_c)\ \epsilon_\Gamma\ A_H \tag{194}$$

and, adding all the heat inputs to the liquid

$$Q_L = [q''_{SPL} + (1 - \epsilon_\Gamma)\ q''_{NB} + \epsilon_\Gamma\ q''_c]\ A_H \tag{195}$$

The heat source term for vapor generation, Q_Γ, enters the liquid energy equation as an explicit vapor generation rate [$\Gamma = Q_\Gamma/(h_g - h_f)$] and will partially condense because of the implicit bulk condensation. This model has been quite successful in predicting subcooled void distributions (Ref. 52).

4.2.5 Critical Heat Flux and Transition Boiling Regime

The intersection of the nucleate boiling and transition boiling heat transfer regimes occurs at the CHF point. To provide for a continuous transition between regimes, the CHF point (q''_{CHF}, T_{CHF}) must be specified.

Three CHF regimes are considered (see Figure 18): pool boiling, forced-convection departure from nucleate boiling (DNB) and annular film dryout.

Pool Boiling DNB

Pool boiling DNB is selected when the mass flux is low ($G < 30$ g/cm^{2}sec) and the flow regime is not annular film flow. The pool boiling critical heat flux is given by Griffith's (Ref. 74) modification of the Zuber (Ref. 53) equation:

$$q''_{CHF} = 0.9\ (1 - \alpha)\ \frac{\pi}{24}\ h_{fg}\ \rho_g^{0.5}\ [g_c g \sigma(\rho_f - \rho_g)]^{0.25} \qquad (196)$$

The critical heat flux in this region is chosen as the larger of Equation 193 and the forced convection DNB heat flux evaluated at a mass flux of 30 g/cm^2-sec. The saturation properties are calculated at the total pressure and not at the partial pressure of steam.

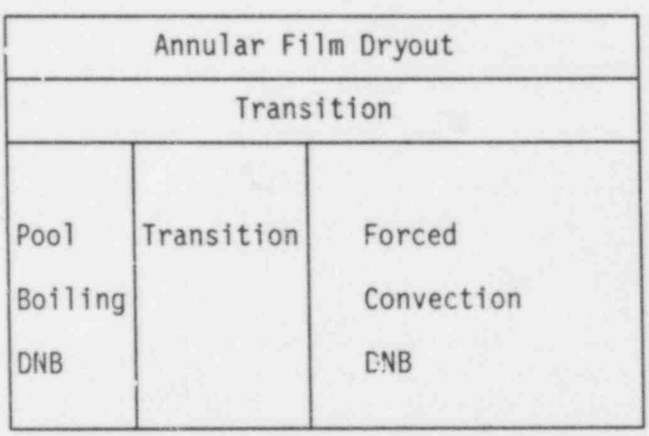

Figure 18 Schematic of CHF regime selection logic

Forced-Convection DNB

Forced-convection DNB is considered when the mass flux is greater than 30 g/cm^{2}sec and the flow regime is not annular film flow. The critical heat flux is given by the Biasi correlation (Ref. 54), which consists of two equations, one for low-quality CHF and one for high-quality CHF, and is given below:

$$q''_{B1} = (5.9695 \times 10^6)\, G^{-1/6}\, (F(P)G^{-1/6} - X)\, D_H^{-n} \tag{197}$$

$$q''_{B2} = (11.98 \times 10^6)\, H(P)\, (1 \times X)\, D_H^{-n}\, G^{-0.6} \tag{198}$$

where q'' = critical heat flux (Btu/hr-ft^2)
G = mass flux (g/cm^2-sec)
P = total pressure (bars)
D_H = hydraulic diameter (cm)
X = quality
n = 0.6, if $D_H < 1.0$ cm: $n = 0.4$, if $D_H \geq 1.0$ cm

and

$$F(P) = 0.7249 + 0.099\, P \exp(-0.032\, P) \tag{199}$$

$$H(P) = -1.159 + 0.149\, P \exp(-0.019\, P) + 8.99\, P\, (10+P^2)^{-1}. \tag{200}$$

The critical heat flux is defined as the maximum of the two equations.

$$q''_{CHF} = \text{maximum}\,(q''_{B1}, q''_{B2}) \tag{201}$$

Annular Film Dryout

If annular flow exists, the departure from nucleate boiling is caused by annular film dryout. In this regime, the heat flux is not limited by a correlation; instead, forced convection vaporization exists until the film dries out. Film dryout is a complex function of the film flow rate, the applied heat flux, and the entrainment/de-entrainment rate, and is determined by the solution of the hydrodynamic equations. This approach was pioneered by Whalley et al. (Ref. 55,56) and has been applied successfully to the analysis of the Bennett tube tests (Ref. 57) (see Volume 4, Developmental Assessment and Applications). It is assumed that the liquid film is entirely evaporated when the liquid fraction is less than 0.0025.

To be consistent with the remainder of the heat transfer package, the critical heat flux point for annular film dryout must be defined. A value of 75°F wall superheat has been selected, and the critical heat flux is set to that given by the Zuber equation. The onset of film boiling is not affected by this definition because film boiling is controlled by film dryout (see Figure 15). As before, the critical heat flux is ramped between the annular film dryout regime and the pool boiling and forced-convection DNB regimes.

Critical Heat Flux Temperature

To define the boiling curve, it is necessary to know the surface temperature at which CHF occurs. An iterative procedure is used to find the wall temperature at which the heat flux from the Chen nucleate boiling correlation is equal to the critical heat flux. Thus,

$$q''_{CHEN}\ (T_{CHF}) = q''_{CHF}$$

Minimum Stable Film Boiling Point

The transition boiling regime is bounded by the CHF point (below which the wall is continuously wetted and nucleate boiling exists) and the minimum stable film boiling point (above which the liquid cannot wet the wall and film boiling exists). It is assumed that the minimum film boiling temperature is the wall temperature that results in an instantaneous contact temperature equal to the homogeneous nucleation temperature, T_{HN}. Using a contact temperature correction to include the effects of surface thermal properties, the minimum film boiling temperature is

$$T_{MIN} = T_{HN} + (T_{HN} - T_{\ell}) \sqrt{\frac{(k\rho C_p)_{\ell}}{(k\rho C_p)_w}} \quad (202)$$

where the homogeneous nucleation temperature is given as a function of pressure by a simple curve fit

$$T_{HN} = 705.44 - (4.722E\text{-}2)\ DP + (2.3907E\text{-}5)\ DP^2 - (5.8193E\text{-}9)\ DP^3 \quad (203)$$

where DP = 3203.6 - P.

The minimum film boiling temperature is specified as the larger of either Equation 202 or that given by Henry's (Ref. 58) modification of the Berenson correlation:

$$T_{MIN} = T_B + 0.42\ (T_B - T_{\ell}) \sqrt{\frac{(k\rho C_p)_{\ell}}{(k\rho C_p)_w}} \left[\frac{h_{fg}}{C_{pw}(T_B - T_f)}\right]^{0.6} \quad (204)$$

where

$$T_B = T_f + 0.127 \frac{\rho_v\ h_{fg}}{k_v} \left[\frac{g(\rho_f - \rho_g)}{(\rho_f + \rho_g)}\right]^{2/3} \left[\frac{g_c \sigma}{g\ (\rho_f - \rho_g)}\right]^{1/2} \left[\frac{\mu_v}{g\ (\rho_f - \rho_g)}\right]^{1/3}$$

In addition, the minimum film boiling temperature is restricted to:

$$800^{\circ}F \leq T_{MIN} \leq 1200^{\circ}F$$

Again, the saturation properties are calculated at the total pressure.

Transition Boiling

At present, there is no consensus on a correlation to use for the transition boiling region. The COBRA-NC uses a simple interpolation scheme (Ref. 74) between the critical heat flux (T_{CHF}, q''_{CHF}) and minimum film boiling (T_{MIN},

q''_{MIN}) point to compute the fraction of the wall that is wettable. This method is simple and physically based, and results in a continuous boiling curve.

It is assumed that the transition boiling heat transfer is composed of both nucleate boiling (wet wall) and film boiling (dry wall) heat transfer, as follows:

$$q''_{TB} = \text{maximum } (0.2\ (1-\alpha)\ \delta\ q''_{CHF} + q''_{FB} \tag{205}$$

where

$$\delta = \left(\frac{T_w - T_{MIN}}{T_{CHF} - T_{MIN}}\right)^2 \tag{206}$$

For top quenching, the void fraction can be very large (0.95 to 0.99) and yet still produce significant quench rates. Because the void fraction remains near unity, the (1-α) modifier in Equation 196 applies too restrictive a constraint upon the transition boiling heat flux. This is overcome by removing the from the calculation for a region near the top quench front (the so-called "sputtering" region). Instead, an exponential decay as a function of distance is employed

$$\xi = \text{EXP } [-2.75(\Delta Z-0.1)]$$
$$\xi = \text{minimum } (1.0, \text{maximum } (\xi, 1-\alpha) \tag{207}$$

where ξ = exponential modifier
ΔZ = distance below a top quench front (inches)

and

$$q''_{TB} = \xi\ \delta q''_{CHF} + q''_{FB} \tag{208}$$

The transition boiling heat flux at a top quench front is not enhanced above the reasonable value of ($\delta\ q''_{CHF}$); rather, the amount by which it is decreased as a function of void fraction is reduced. The film boiling heat flux is the value obtained by evaluating the appropriate film boiling correlation (see below).

4.2.6 Dispersed Flow and Inverted Annular Film Boiling

Heat transfer in the film boiling region is assumed to result from one of two mechanisms: dispersed flow film boiling (DFFB) or inverted annular film boiling (IAFB).

Dispersed flow film boiling is selected if the void fraction is greater than 0.8. It is treated by a "two-step" method where the dominant heat transfer mode is forced convection to superheated steam. The steam superheat is then determined by the interfacial heat transfer rate to the entrained droplets as part of the hydrodynamic solution. Heat fluxes due to wall-droplet radiation and droplet impingement are superimposed upon the vapor convective heat flux. The total heat flux is

$$q''_{DFFB} = q''_{FC} + q''_{R} + q''_{W-D} \tag{209}$$

where $q''_{FC} = H_{SPV}\ (T_W - T_V)$

H_{SPV} = the Dittus-Boelter correlation

T_v = superheated vapor temperature

q''_R = wall-drop radiation heat flux

q''_{W-D} = drop impingement heat flux

Heat transfer due to droplets striking the wall is evaluated using the Forslund-Rohsenow (Ref. 59) equation:

$$q''_{W-D} = 0.2\ \frac{\pi}{4}\ \left(\frac{6}{\pi}\right)^{2/3}\ (1 - \alpha)^{2/3} \left[\frac{g\rho_f\ \rho_v\ h_{fg}\ k_v^3}{(T_w - T_f)\ \mu_v \left(\frac{\pi}{6}\right)^{1/3} D_D}\right]^{1/4} \tag{210}$$

where D_D = drop diameter, calculated using the entrained void fraction and the droplet number density.

The radiative heat transfer, q''_p is calculated using the model of Sun, Gonzalez and Tien (Ref. 60) and is discussed later under radiation heat transfer.

When the void fraction is less than 0.6, inverted annular film boiling is assumed to occur. The heat flux for this regime is computed from the larger of either the value calculated in Equation 209 for dispersed flow film boiling or the value from the modified Bromley correlation (Ref. 61);

$$q''_{BROM} = 0.62 \left(\frac{D_H}{\lambda_c}\right)^{0.172} \left[\frac{k_g^3 \rho_g (\rho_f - \rho_g) h'_{fg} g}{D_H \mu_g (T_w - T_f)}\right]^{1/4} (T_w - T_f) \qquad (211)$$

where $h'_{fg} = h_{fg} [1.0 + 0.4 C_{pv} (T_w - T_f)/h_{fg}]$

$$\lambda_c = 2\pi \left[\frac{g_c \sigma}{g (\rho_f - \rho_g)}\right]^{1/2}$$

The radiation heat flux from the wall to the liquid core is

$$q''_{R_I} = \frac{\sigma_{SB}}{\frac{1}{\epsilon} + \frac{1}{\alpha_L} - 1} (T_w^4 - T_f^4) \qquad (212)$$

where σ_{SB} = Boltzman constant
ϵ = emissivity of heat heated rods
α_L = absorptivity of liquid

So, for inverted annular film boiling, the heat flux is

$$q''_{IAFB} = q''_{BROM} + q''_{R_I} \qquad (213)$$

At intermediate void fractions ($0.8 > \alpha > 0.6$), the heat flux is interpolated between the values for inverted annular and dispersed flow film boiling. All fluid saturation properties are calculated for steam at the total pressure and not at the partial pressure of steam.

Radiation Heat Transfer in Dispersed Flow Film Boiling Regime

The radiation heat transfer model used in the dispersed flow regime was developed by Sun, Gonzalez and Tien (Ref. 60). They demonstrated that if the dispersed flow regime is "optically thin", then the wall, vapor, and liquid droplets can be treated as single nodes in a conventional network analysis of radiation heat transfer. Using this assumption, the gray body factors are

$$F_{W\text{-}D} = 1/[R_2\ (1 + \frac{R_3}{R_1} + \frac{R_3}{R_2})]$$

$$F_{W\text{-}V} = 1/[R_1\ (1 + \frac{R_3}{R_1} + \frac{R_3}{R_2})] \qquad (214)$$

where

$$R_1 = \frac{1 - \epsilon_v}{\epsilon_v(1 - \epsilon_v\epsilon_f)}$$

$$R_2 = \frac{1 - \epsilon_f}{\epsilon_f(1 - \epsilon_v\epsilon_f)} \qquad (215)$$

$$R_3 = \frac{1}{1 - \epsilon_v\epsilon_f} + \frac{1 - \epsilon_w}{\epsilon_w}$$

and

$$\epsilon_v = 1 - \exp(-\,a_v\,L)$$

$$\epsilon_f = 1 - \exp(-\,a_f\,L) \qquad (216)$$

The parameter L is the mean beam length and is assumed equal to the hydraulic diameter of the cell. The vapor emissivity (a_v) is assumed equal to 0.02, and the liquid emissivity is

$$a_f = 0.74 \left(\frac{\pi}{4}\right) D_D^2 N_D \tag{217}$$

where N_D is the drop number density.

The radiative heat fluxes are given by

$$q''_{W-D} = F_{W-D} \sigma_{SB} (T_w^4 - T_f^4)$$

$$q''_{W-V} = F_{W-V} \sigma_{SB} (T_w^4 - T_v^4) \tag{218}$$

where σ_{SB} is the Boltzman constant.

4.3 Quench Front Model

Coupled thermal-hydraulic numerical simulations of rewetting encounter difficulties with large axial computational mesh spacing (typically, 2 feet for a full vessel) which cannot adequately resolve the axial profile of temperature and surface heat flux across the quench front. During quenching, the entire boiling curve--from film boiling through transition boiling and critical heat flux to nucleate boiling--can be encompassed by one hydrodynamic mesh cell. Constraining the entire cell to be in one boiling regime is nonphysical and results in stepwise cell-by-cell quenching, producing flow oscillations that can obscure the correct hydrodynamic solution. Consequently, an integration of the boiling curve shape through the hydrodynamic computational cell must be performed to determine the fluid heat input.

A fine mesh-rezoning technique (Ref. 62) is employed in the rod model to surmount these difficulties. Fine mesh heat transfer cells with axial and radial conduction are superimposed upon the coarse hydrodynamic mesh spacing, and a boiling heat transfer package is applied to each node.

By solving the two-dimensional conduction equation for a variable fine mesh at the quench front, propagation due either to quenching or dryout can be resolved and the surface heat flux integrated to provide the cell-averaged phasic heat inputs for the fluid energy equation. The resulting quench front velocity will be a function of:

- axial conduction
- boiling curve shape

- prequench heat transfer
- internal heat transfer within the rod.

Resolution of axial temperature and surface heat flux excursions is achieved by rezoning the heat conductor mesh in their vicinity. Figure 19 illustrates the normal axial noding scheme. Both fluid and rod temperatures are calculated at the centers of the fluid continuity cells. Two extra rod nodes are included at the top and bottom of the rod. When axial temperature differences between adjacent axial nodes exceed splitting criteria (user-specified maximum surface temperature differences) an additional row of nodes is inserted halfway between the two original nodes. (This is illustrated in Figure 20.) The temperatures assigned to these nodes are computed so that energy is conserved. This splitting process continues (over a succession of time steps) until the mesh is fine enough to resolve the surface temperature curve to the desired level of detail.

The correct temperature differences to be used as splitting criteria depend on the heat transfer regime. They are further modified by functions of the wall temperature (when the wall temperature is near the critical heat flux temperature) to ensure resolution of the surface heat flux profile in the vicinity of the quench front. The temperatures assigned to the inserted nodes are calculated from an energy balance:

$$Cp_1 (T_1 - T_I) \frac{\Delta X}{2} + Cp_2 (T_2 - T_I) \frac{\Delta X}{2} = 0$$

$$T_I = \frac{(CpT)_1 + (CpT)_2}{(Cp_1 + Cp_2)} \qquad (219)$$

where the subscripts I, 1, and 2 represent the inserted and two original nodes, respectively.

Conversely, when a fine mesh has been established, but the disturbance has propagated downstream and the fine mesh is no longer necessary, adjacent nodes can be coalesced back down to one node. The decision to merge cells is based on minimum temperature differences between adjacent nodes. Eventually, all the fine mesh nodes in a region will coalesce, and only the original nodes (those coincident with hydrodynamic scalar mesh cell boundaries) will remain.

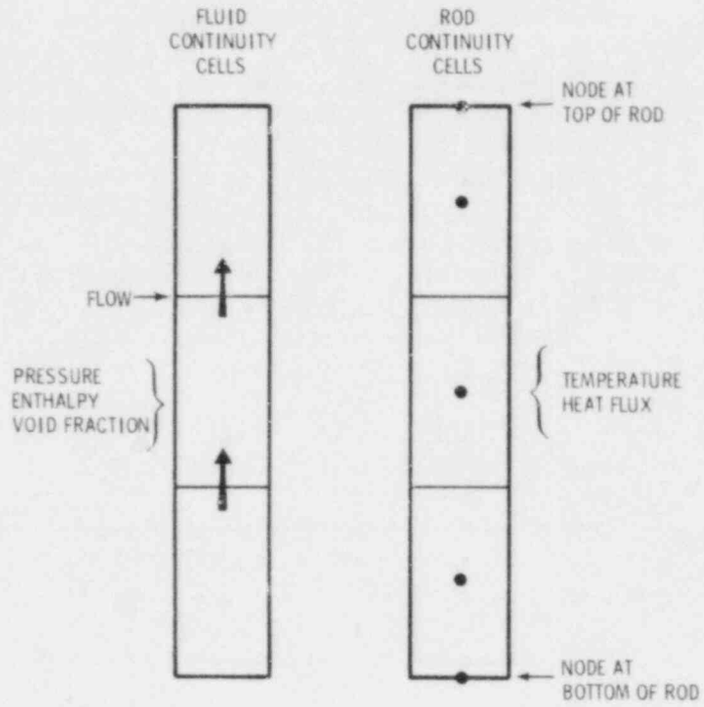

Figure 19 Example of COBRA-TF axial noding scheme

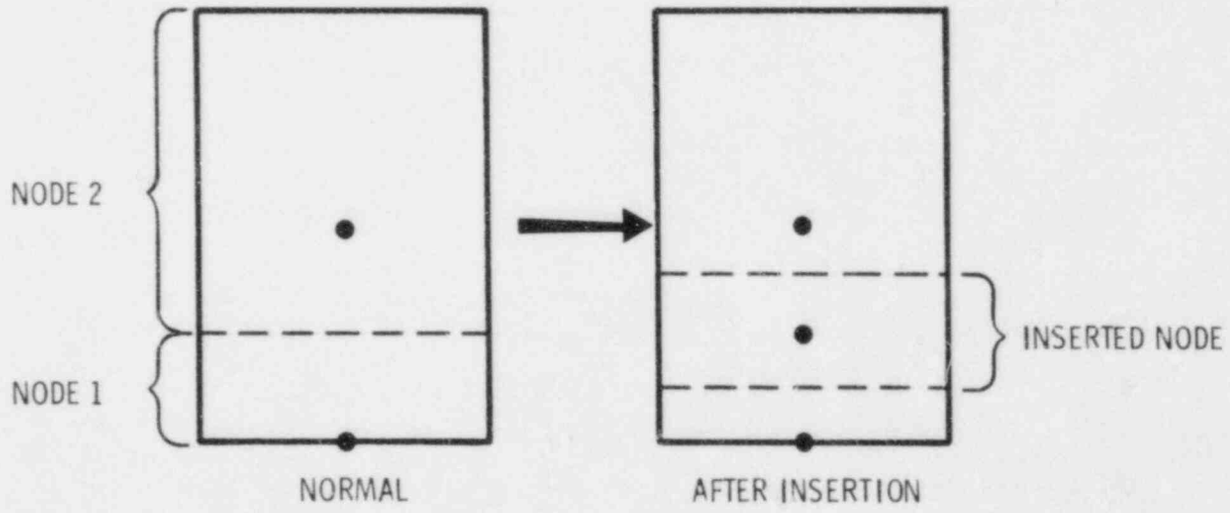

Figure 20 Example of node insertion

The fine mesh-rezoning model differs from other reflood models [such as the one employed in RELAP4/MOD6 (Ref. 63)] in that the fine mesh nodes are stationary and do not have a fixed mesh spacing. The fine mesh nodes are split to create a graduated mesh spacing that readjusts itself constantly to the changing axial temperature gradient. This approach permits node sizes small enough (e.g., 0.05 inches) to resolve axial conduction and the boiling curve shape at the quench front, and yet minimizes the number of nodes required. It ensures conservation of stored energy when cells are added, and simplifies coupling with the hydrodynamic solution. Figures 21 and 22 (taken from a simulation of a FLECHT low flooding rate test) illustrate the resolution of the cladding temperature profile and the surface heat flux in the vicinity of the quench front.

4.4 Gap Conductance Model

The dynamic gap conductance model computes changes in the nuclear fuel rod structure and fill gas pressure that affect the gap conductance and fuel temperature during a transient. The method is based primarily on previous work in the GAPCON (Ref. 37,39) and FRAP (Ref. 36,40,41) series of fuel performance codes but with the mechanics and fill gas pressure models greatly simplified. The material property correlations are taken exclusively from MATPRO-11 (Revision 1) (Ref. 38); refer to Appendix B.

The gap conductance between the fuel outside surface and cladding inside surface has three components:

$$H_{gap} = H_{rad} + H_{gas} + H_{solid} \tag{220}$$

where H_{rad} = heat transfer due to thermal radiation
H_{gas} = heat transfer due to conduction in the fill gas
H_{solid} = heat transfer due to physical contact between the fuel pellet and the clad.

Each of these terms has associated with it certain models and assumptions. These are discussed in detail below. In all models, the gap is assumed axisymmetric, the fuel is uranium dioxide, and the cladding is zircaloy. Thermal properties of other materials may be specified by the user, but the mechanical material properties will remain those of uranium dioxide and zircaloy.

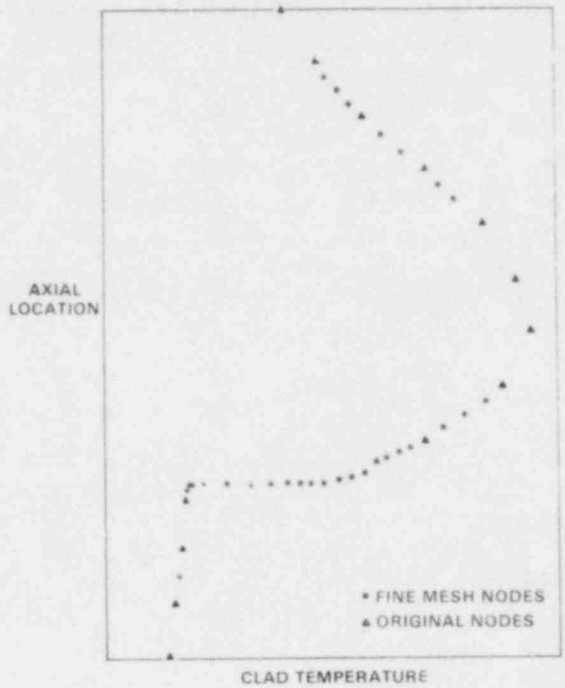

Figure 21 Fine mesh renoding: cladding temperature profile

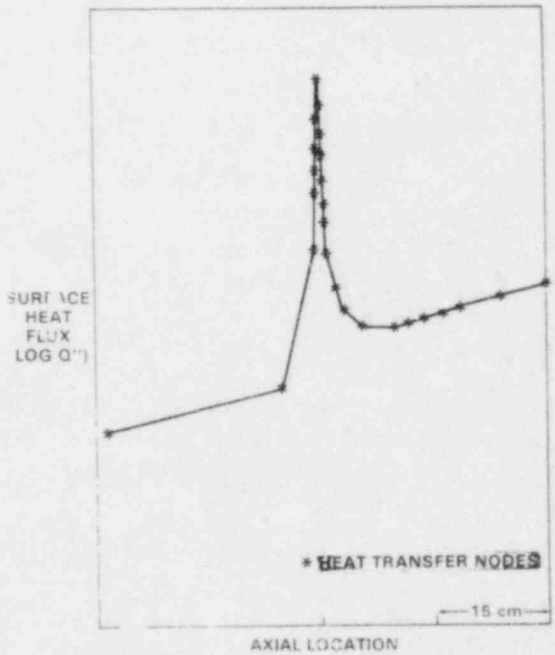

Figure 22 Fine mesh renoding: surface heat flux

4.4.1 Radiant Heat Transfer

The gap conductance due to radiant heat transfer is the ratio of the gap radiant heat flux, to the temperature rise across the fuel/cladding gap

$$H_{rad} = \frac{q''_R}{T_1 - T_2} \tag{221}$$

The radiant heat flux leaving the fuel surface, q''_r, is determined from the Stefan-Boltzmann equation using appropriate fuel cladding geometry factors, so that

$$q''_r = \sigma_{SB} \left[\frac{1}{\epsilon_1} + \frac{A_1}{A_2}\left(\frac{1}{\epsilon_2} - 1\right)\right]^{-1} \left[T_1^4 - T_2^4\right] \tag{222}$$

where A_1 = fuel surface area (ft^2)
A_2 = cladding surface area (ft^2)
ϵ_1 = fuel surface emissivity
ϵ_2 = cladding surface emissivity
T_1 = fuel surface temperature ($^\circ R$)
T_2 = cladding surface temperature ($^\circ R$)
σ_{SB} = Stefan-Boltzmann constant (1.714×10^{-9} Btu/hr-ft^2-$^\circ R^4$)

The emissivities of the fuel and cladding are calculated using relationships from MATPRO-11 (Revision 1); see Appendix B, Equation B.6. The effect of the cladding oxide layer thickness on the emissivity is neglected.

4.4.2 Conduction Heat Transfer in the Fill Gas

Heat conduction through the fill gas is calculated using the model developed for GAPCON-2 based on a linear regression analysis of Ross-Stoudt data by Lanning and Hann (Ref. 64). For a normal open gap the conductance is

$$H_{gas} = \frac{k_{gas}}{t_g + 1.845\,(g_1 + g_2)} \tag{223}$$

where k_{gas} = fill gas mixture thermal conductivity (Btu/hr-ft- °F)

t_g = gas gap width (from deformation model) (ft)

g_1 = fuel pellet temperature jump distances (ft)

g_2 = cladding temperature jump distances (ft)

The temperature jump distances compensate for the nonlinearity of the temperature gradient near the walls and the temperature discontinuities on the wall surface as illustrated in Figure 23. The nonlinear temperature gradient is due to the incomplete thermal mixing of the gas molecules near the surface. The surface temperature discontinuity results from the incomplete thermal accommodation of the gas molecules to the surface temperature.

The GAPCON-2 modification of the Lloyd model (Ref. 65) is used to calculate the temperature jump distance. The Lloyd model compares well with available data and is used in both the FRAP and GAPCON-2 codes. The temperature jump distance term is evaluated with the relationship[(a)]

$$(g_1 + g_2) = 1.131(10^{-5}) \frac{k_{gas} (T_g)^{1/2}}{P_{gas} \sum_{j=1}^{6} \frac{a_j f_j}{(M_j)^{1/2}}} \qquad (224)$$

where k_{gas} = fill gas mixture thermal conductivity (Btu/hr-ft-°F) (see Appendix B)

T_g = gas gap average temperature (°K)

f_j = mole fraction of jth gas

M_j = molecular weight of jth gas

a_j = accommodation coefficient of jth gas

P_{gas} = fill gas pressure (psia).

(a) Note that the equation as written in the GAPCON-2 manual is in error.

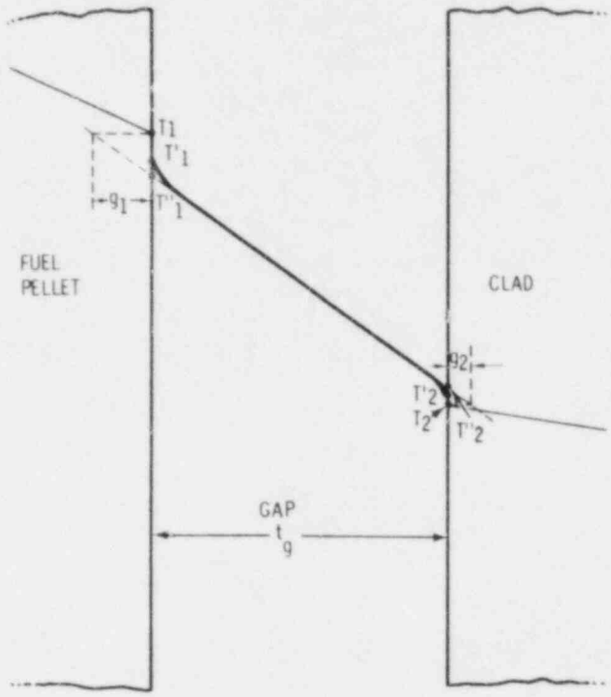

Figure 23 Temperature jump distances for an ideal gap

Measurements for helium and xenon on UO_2 by Ullman et al. (Ref. 66) show that accommodation coefficients are temperature-dependent and vary for different gases. These dependencies are incorporated by using the GAPCON-2 curve fits to the Ullman data:

$$a_{He} = 0.425 - 2.3(10^{-4})T$$
$$a_{Xe} = 0.749 - 2.5(10^{-4})T \qquad (225)$$

where T is in Kelvin (°K).

The accommodation coefficients for other gases are approximated using a linear interpolation between those of helium and xenon based on molecular weight. This was found to correlate the data of Thomas (Ref. 67) with reasonable accuracy.

The gas mixture conductivity, k_{gas}, is determined from the conductivities of the constituent gases using a simplified version of the model in the MATPRO-11 subroutine GTHCON. Since the code uses the temperature jump model described above the free molecular convection (Knudsen) regime correction to the gas conductivity given in MATPRO is not required. The conductivities of helium, xenon, argon, krypton, hydrogen and nitrogen gas are calculated using correlations from MATPRO-11 (Revision 1). The correlations compare favorably with the Chapman-Enskog theory used in GAPCON but are much easier to implement.

When fuel/cladding contact occurs--from deformation caused by thermal expansion or mechanical stress or a combination of the two--the heat conductance in the gas becomes

$$H_{gas} = \frac{kj_{gas}}{\{1.8[C(R_1 + R_2) + g_1 + g_2] - 4.2(10^{-7})\}} \qquad (226)$$

where k_{gas} = fill gas mixture thermal conductivity (determined as for open gap)

g_1, g_2 = fuel pellet and cladding temperature jump distances (determined as for the open gap)

C = $1.98 \exp [-8.8(10^{-5})]P_i$, dimensionless constant where P_i is the contact pressure (in psi, determined by the deformation model).

Fuel cladding contact is defined to occur when

$$t_g < 3.6\ (R_1 + R_2) \qquad (227)$$

where t_g = gas gap width (from the deformation model; discussed below)

R_1 = mean surface roughness of fuel pellet

R_2 = mean inside surface roughness of cladding.

By this criterion, contact is assumed to occur because of waviness and mismatch of the fuel/clad interface when the calculated gap width closes to within 3.6 times the combined surface roughnesses. This was determined by comparing measured gap widths with calculated gap widths from GAPCON (Ref. 68). A more complete discussion is available in the GAPCON-2 manual (Ref. 37).

4.4.3 Fuel/Cladding Contact Conductance

When the fuel and cladding are not in contact, H_{solid} must be zero. But when the deformation model determines that the gap between the fuel and cladding is small enough for contact to occur, the Mikic/Todreas model (Ref. 69,70) is used to determine the contact conductance. Of the available models it provides the best agreement with a wide range of contact conductance data (Ref. 64,71).

In this model, H_{solid} is defined in terms of the physical properties of the materials and the geometry of the interface between them:

$$H_{solid} = \frac{5k_m}{(R_1^2 + R_2^2)^{1/2}} \left(\frac{P_{int}}{H_M}\right)^n \left(\frac{R_1}{\lambda_1}\right) \quad (228)$$

where $k_m = \frac{2k_1k_2}{k_1 + k_2}$

k_1 = fuel thermal conductivity (Btu/hr-ft-°F)

k_2 = cladding thermal conductivity (Btu/hr-ft-°F)

R_1 = mean fuel surface roughness (in.)

R_2 = mean cladding surface roughness (in.)

$\frac{P_{int}}{H_M}$ = the dimensionless ratio of the interface pressure to the Meyer hardness

$\frac{R_1}{\lambda_1}$ = the dimensionless ratio of the mean fuel surface roughness and wave length (distance between peaks).

The interfacial pressure, P_{int}, due to the differential fuel and cladding expansion, is calculated with the fuel deformation model and is nondimensionalized using the Meyer hardness calculated from MATPRO-11 (Revision 1) subroutine CMHARD (Ref. 38). The exponent, n, on the ratio of interfacial pressure to Meyer hardness is defined (Ref. 67) as

$n = 1.0$ $\quad (P_{int}/H_M > 0.01$

$n = 0.5$ $\quad (P_{int}/H_M) < 0.0001$

For the intermediate range, the ratio is held constant:

$$\left(\frac{P_{int}}{H_M}\right)^n = 0.01 \qquad 0.0001 < (P_{int}/H_M) < 0.01$$

The ratio of fuel surface roughness to wave length is estimated by GAPCON-2 as

$$\left(\frac{R_1}{\lambda_1}\right) = \exp\left[0.5285 * \ln\left(R_1 - 5.738\right)\right] \qquad (229)$$

where R_1 = the mean fuel surface roughness (microinches).

4.4.4 Deformation Model

The fuel rod deformation model is used to predict changes in the structural gap between the fuel pellet and cladding caused by elastic and thermal stresses. Deformation of the fuel pellet due to thermal expansion and relocation is considered. Fuel relocation is available as an option specified by the user through input. Deformation of the cladding due to mechanical and thermal stresses is considered. If the fuel/cladding gap is open, elastic deformation may be induced by the difference between the internal gas pressure and the system pressure. When the gap closes, elastic displacement of the cladding by radial expansion of the fuel in contact with it is calculated, but plastic deformation is neglected. Bending stresses or strains in the cladding or fuel are considered insignificant, and creep deformation of the cladding is ignored.

The phenomenon being modeled by the dynamic gap conductance model causes changes in the fuel rod geometry over a short time (i.e., during the blowdown and reflood stages of a LOCA). Changes in fuel rod conditions that take place over a long period (i.e., burnup-dependent quantities such as swelling, densification, and fission gas release) are not modeled and should be accounted for in the input. Most steady-state fuel rod conditions can be modeled with the dynamic gap conductance model by specifying the proper input values for cold state gap width, plenum volume, and internal gas pressure.

The axial and diametral thermal expansion of the fuel is calculated using the MATPRO-11 (Revision 1) (Ref. 38) FTHEXP subroutine correlation for thermally induced strain in UO_2. The correlation was simplified by omitting the corrections for molten fuel and mixed oxide (Pu).

In this model, the radial cracks in the fuel are assumed to relieve the hoop and radial stresses, allowing unrestrained radial movement of the fuel in each concentric radial node. The total radial movement at the fuel pellet exterior is the sum of the expansion in all the fuel nodes:

$$(\Delta r_{th})_{fuel} = \sum_{i=1}^{NFUEL} \epsilon_r(T_i)_j \Delta r_i \qquad (230)$$

where $\epsilon_r(T_i)_j$ = thermal strain at axial node j and radial node i

Δr_i = thickness of radial node i

NFUEL = number of radial nodes in the fuel.

The stress-free axial thermal expansion of the fuel pellet stack is calculated in an analogous manner. The fuel pellet stack length change due to the thermal expansion is

$$(\Delta \ell_{th})_{fuel} = \sum_{j=1}^{NDX} \epsilon_Z (\bar{T}_j) \Delta X_j \qquad (231)$$

where $\epsilon_Z(\bar{T}_j)$ = thermal strain at axial node j based on volume-averaged radial node temperatures

ΔX_j = height of axial node j

NDX = number of axial nodes.

The radial thermal expansion of the cladding is described by

$$(\Delta r_{tj})_{clad} = \epsilon_r(\bar{T}_j)\bar{r} \qquad (232)$$

where $\epsilon_r(\bar{T}_j)$ = radial thermal strain at axial node j based on the average cladding temperature

$\bar{r}$ = cladding mean radius.

The axial thermal expansion of the cladding is

$$(\Delta \ell_{th})_{clad} = \sum_{j=1}^{NDX} \epsilon_Z (\bar{T}_j) \Delta X_j \tag{233}$$

where $\epsilon_Z(\bar{T}_j)$ = radial thermal strain at axial node j based on the average cladding temperature

ΔX_j = height of axial node j.

When the fuel cladding gap is open, elastic deformation of the cladding is driven by the difference between the fill gas and system pressures. If the gap closes, the cladding deformation is caused by the radial motion of the fuel. In both models the cladding is assumed sufficiently thin for the stress, strain, and temperature to be uniform throughout the cladding thickness.

In the open gap elastic deformation model, the cladding is considered as a thin cylindrical shell loaded by internal and external pressures. (Axisymmetric loading and deformation are assumed.) The radial and axial elastic deformation is the result of hoop stress and axial stress caused by pressure difference. These stresses are given by the following equations:

$$\sigma_\theta = \frac{r_i P_i - r_o P_o}{t_c} \tag{234}$$

$$\sigma_Z = \frac{\pi r_i^2 P_i - \pi \rho_o^2 P_o}{\pi (r_o^2 - r_i^2)} \tag{235}$$

where r_o = cladding outside radius

r_i = cladding inside radius

t_c = cladding thickness

P_i = internal fill gas pressure (P_G if the gap is open, Equation 240; P_{int} if the gap is closed, Equation 244)

P_o = system pressure.

The radial stress component is neglected, yielding the following relationships from Hook's Law:

$$\epsilon_\theta = \frac{\Delta r}{\bar{r}} = \frac{1}{E}(\sigma_\theta - \nu\sigma_Z) \tag{236}$$

$$\epsilon_Z = \frac{\Delta \ell}{\ell} = \frac{1}{E}(\sigma_Z - \nu\sigma_T) \tag{237}$$

where ϵ_θ = hoop strain

ϵ_Z = axial strain

E = modulus of elasticity (Young's modulus)

ν = Poisson ratio, E/2G - 1 where G = shear modulus.

The relationships for the cladding radial and axial elastic deformations, then, are

$$(\Delta r_{el})_{clad} = \epsilon_\theta \bar{r} \tag{238}$$

$$(\Delta \ell_{el})_{clad} = \sum_{j=1}^{NDX} \epsilon_Z \Delta X_j \tag{239}$$

where ϵ_θ = hoop strain at axial node j

r = cladding mean radius

ϵ_Z = axial strain at axial node j

ΔX_j = height of axial node j.

The internal fill gas pressure used to determine the cladding elastic deformation when the gap is open is calculated from the relationship

$$P_G = \frac{MR}{\frac{V_p}{T_p} + \sum_{j=1}^{NDX} \pi \Delta X_j \left[\frac{(r_{ci}^2 - r_{fo}^2)}{T_G} + \frac{r_v^2}{T_V} + \frac{(r_{fo}^2 - r_f^2)}{T_F}\right]_j} \quad (240)$$

where M = gram-moles of gas in fuel rod

V_p = gas plenum volume, including effects of fuel and cladding axial expansion (ft^3) (from Equations 231, 233, and 239)

T_p = gas plenum temperature (°K) (defined as the outlet fluid temperature + 10 °K)

ΔX_j = computational cell length at axial level j (ft)

r_{ci} = cladding inside radius including thermal and elastic expansion (ft) (from Equations 232 and 238)

r_{fo} = fuel outside radius including thermal expansion and relocation (ft) (from Equations 230, 245 and 246)

r_f = fuel outside radius including thermal expansion (ft)

R = universal gas constant (6.1313 $\frac{\text{ft-lbf}}{\text{g-mole-°K}}$)

r_v = radius of central void (ft) (from input data)

T_G = gas gap temperature (°K)

T_V = central void temperature (°K)

T_F = average fuel pellet temperature (°K).

This is a static lumped pressure model, similar to those in FRAP or GAPCON. The pressure is assumed uniform throughout the fuel pin, with constant fission gas inventory.

The fuel cladding gap width is given by

$$t_g = t_{cold} - (\Delta r_{th})_{fuel} - (\Delta r_{rel})_{fuel} + (\Delta r_{el})_{clad} + (\Delta r_{th})_{clad} \quad (241)$$

where t_{cold} = input value for fuel cladding gap width (including burnup-dependent effects)

$(\Delta r_{th})_{fuel}$ = fuel radial thermal expansion (from Equation 176)

$(\Delta r_{th})_{clad}$ = cladding radial thermal expansion (from Equation 22)

$(\Delta r_{el})_{clad}$ = cladding radial elastic expansion (from Equation 235)

$(\Delta r_{rel})_{fuel}$ = fuel radial relocation (from Equation 243 or 242).

The value of t_g calculated in Equation 241 is used in Equation 227 to determine if the gap is open or closed. If the gap is open, the gap conductance is calculated with H_{solid} set to zero. If the gap is closed, the Mikic/Todreas model for H_{solid} must be evaluated. This requires the closed gap deformation model, which is used to determine the interfacial contact pressure needed in Equation 228.

In the closed gap deformation model, the cladding is considered as thin-wall tubing with a specified displacement at the inside and pressure loading at the outside surface. The radial fuel displacement that elastically deforms the cladding is applied directly to the cladding and can be calculated as

$$(\Delta r_{th})_{fuel} = (\Delta r_{th})_{clad} + t_g|_L = T_{cold} \qquad (242)$$

where $t_g|_L$ = fuel cladding gap width that defines the closed gap (i.e., 3.6 $(R_1 + R_2)$ as in Equation 227)

t_{cold} = user-input cold fuel cladding gap width (including burnup-dependent effects)

$(\Delta r_{th})_{fuel}$ = fuel radial thermal expansion (from Equation 230)

$(\Delta r_{th})_{clad}$ = cladding radial thermal expansion (from Equation 232).

Fuel deformation due to relocation does not displace the cladding and is therefore not included in Equation 242.

Displacement due to radial strain is assumed negligible, so the radial elastic deformation of the cladding must be equal to the applied fuel displacement on the inside surface,

$$(\Delta \dot{r}_{th})_{fuel} = (\Delta r_{th})_{fuel} - (\Delta r_{th})_{clad} + t_g|_L - T_{cold}$$

$$(\Delta r_{el})_{clad} = (\Delta \dot{r}_{th})_{fuel} \tag{243}$$

The fuel cladding interfacial pressure generated by the applied displacement can be computed using the equilibrium stress (Equations 234 and 235), Hook's Law (Equations 236 and 237), and the applied displacement, Δr_f. The interfacial pressure is

$$P_{int} = \frac{(\Delta \dot{r}_{th})_{fuel} E t_c (r_o^2 - r_i^2)}{\bar{r}[r_i (r_o^2 - r_i^2) - r_i^2 t_c \nu]} + P_o \frac{r_o(r_o^2 - r_i^2) - r_o^2 t_c \nu}{r_i(r_o^2 - r_i^2) - r_i^2 t_c \nu} \tag{244}$$

where $(\Delta r_{th})_{fuel}$ = applied fuel displacement in cladding (from Equation 243)

E = modulus of elasticity for the cladding

t_c = cladding thickness

r_o = cladding outside radius

r_i = cladding inside radius

$\bar{r}$ = cladding mean radius

ν = Poisson's ratio for the cladding

P_o = system pressure (on the outside surface of the cladding).

The cladding inside and outside radius (r_o and r_i) and the mean radius ($\bar{r}$) are evaluated with elastic and thermal expansion taken into account. The thermal expansion is evaluated using Equation 228, just as in the open gap model. The elastic deformation is evaluated using the relation in Equation 238, but the internal pressure P_i is defined as the interfacial pressure P_{int} from Equation 244 instead of the fill gas pressure P_G from Equation 240.

Fuel relocation is calculated using the FRACAS-I mechanics model from FRAPCON-2 (Ref. 72). FRACAS-I has been chosen for its simplicity and compatibility with the conduction solution. The model allows fuel fragments to move radially

into the pellet-cladding gap. Cracks formed in the pellet change the effective conductivity of the fuel. Figure 24 illustrates fuel relocation and how cracking changes heat conduction in the radial direction. Gap closure and conductivity degradation provide a more realistic radial temperature profile for nuclear fuel rods than is possible without relocation.

The amount of fuel relocation necessary for proper gap closure, according to Coleman (Ref. 73), can be expressed as a function of the cold state rod geometry:

$$(\Delta r_{rel})_{fuel} = \delta - 0.005 r_f \tag{245}$$

where $(\Delta r_{rel})_{fuel}$ = fuel radial relocation (ft)

δ = as-fabricated fuel-cladding gap size (ft)

r_f = as-fabricated pellet radius (ft).

The amount of relocation remains constant so long as the fuel- cladding gap is open. When the gap closes, radial displacement due to relocation remains large enough to keep the fuel and cladding in contact without radially displacing the cladding. Cladding is displaced by fuel thermal expansion only when the radial displacement of the fuel due to relocation is zero. The amount of fuel relocation in the closed gap case is defined as

$$(\Delta r_{rel})_{fuel} = \delta - (\Delta r_{th})_{fuel} + (\Delta r_{th})_{clad} + (\Delta r_{el})_{clad} \tag{246}$$

where $(\Delta \rho_{rel})_{fuel}$ = fuel radial relocation (ft)

δ = as-fabricated fuel-cladding gap size (ft)

$(\Delta r_{th})_{fuel}$ = fuel radial thermal expansion (ft)

$(\Delta r_{th})_{clad}$ = cladding radial thermal expansion (ft)

$(\Delta r_{el})_{clad}$ = cladding radial elastic expansion (ft).

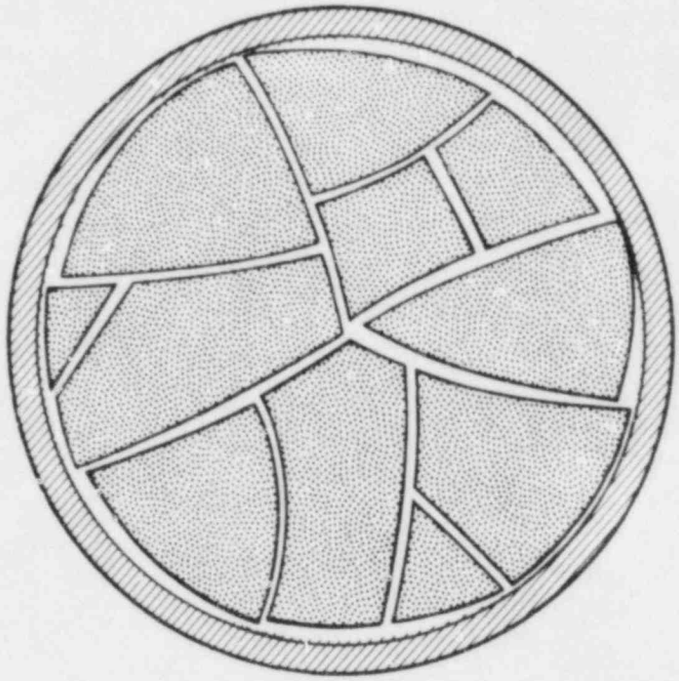

Figure 24 Illustration of fuel relocation

Gap closure is determined by a gap width of less than or equal to 3.6 times the sum of fuel and cladding mean surface roughness.

When fuel relocates into the pellet-cladding gap, cracks in the fuel reduce the effective conductivity of the fuel. FRACAS-I uses an empirical conductivity factor to calculate an effective fuel conductivity when cracks are present:

$$K_{EFF} = R\, K_{LAB} \tag{247}$$

where K_{EFF} = effective fuel thermal conductivity ($W/m\cdot^{\circ}K$)

K_{LAB} = uncracked fuel thermal conductivity ($W/m\cdot^{\circ}K$)

R = conductivity factor.

The conductivity factor is a function of gas conductivity and volume available for cracking and is given by[a]

$$R = 1.0 - C\,C_{rel}\,[1.0 - \frac{k_g}{K_{LAB}}] \qquad (248)$$

where $C_{rel} = \delta/0.8\times10^{-4}$

δ = as-fabricated fuel cladding gap size (m)

C = 0.30 (1/m)

K_g = thermal conductivity of gas in gap (W/m·°K)

K_{LAB} = uncracked fuel thermal conductivity (W/m·°K).

The factor $(1.0-k_g/K_{LAB})$ accounts for the fact that gas in the cracks has a lower thermal conductivity than the fuel and therefore decreases the effective conductivity of the fuel pellet. C_{rel} is a measure of the volume available for cracking. Since cracked fuel does not fully solidify when compressed, C_{rel} is never less than 0.25. Crack healing is assumed to occur instantly when the local fuel temperature exceeds nine-tenths of the fuel sintering temperature. The conductivity factor is set equal to 1.0 when the fuel temperature exceeds 4304.0°F.

4.5 Cladding Oxidation Model

When zircaloy cladding reaches sufficiently high temperatures in a steam environment, an exothermic reaction occurs that causes additional heating of the cladding and produces hydrogen gas. Zirconium and steam are consumed in the process. It has been assumed that the reaction equation

$$2H_2O + Z_r \rightarrow 2H_2 + ZrO_2 + Q \qquad (249)$$

(a) Equation 248 is derived by substituting the definition for V into Equation 51 of Reference 72: $(V = 3Uc/r_f = 3(\delta_S - \delta_T)/r_f)$.

adequately describes the metal/water reaction where $Q = 6.45 \times 10^6$ Joules/kilogram of zircaloy reacted. The reaction rate equation

$$w \frac{dw}{dt} = A\, e^{-B/T} \tag{250}$$

is assumed to be valid, provided that steam and zircaloy are available to sustain the reaction. Equation 250 is valid for both the Cathcart and the Baker-Just models; only the definitions of the variables and the value of the constant coefficients change. W is the total mass of oxygen consumed per unit area of cladding oxidized for the Cathcart model. W is the mass of zirconium reacted for the Baker-Just model. Both models are available in the code, and the user may select either option.

For the Cathcart model,

w = oxide weight gain (kg/m^2)

A = 16.8 $kg^2/m^4 s$ for $T < 1853.0$ K

= 5.426 $kg^2/m^4 s$ for $T \geq 1853.0$ K

B = 20070 K for $T < 1853.0$ K

= 16610 K for $T \geq 1853.0$ K

T = temperature (K)

dt = time differential (s)

For the Baker-Just model

W = mass of zirconium reactor (mg/cm^2)

A = 16.35 $\times 10^6$ m^2/cm^4 s

B = 22900 K

T = temperature (K)

dt = time differential (s)

Using the Cathcart model (Ref. 30), the mass fraction of oxygen in the zirconium dioxide is

$$m_{f_{O_2}} = 0.26 \tag{251}$$

Therefore,

$$w = 0.26\ \rho_{ZrO_2}\ \delta \tag{252}$$

where δ is the oxide thickness.

If it is assumed that ZrO_2 expands 50% above the volume of zirconium and that the expansion occurs in the radial direction, then

$$w = 0.26\ \rho_{ZrO_2}\ (R_o - r)\ 1.5 \tag{253}$$

where R_o is the original cladding outside radius and r is the reacting surface radius. The 50% volume expansion assumption gives

$$\rho_{ZrO_2} = 0.90\ \rho_{Zr} \tag{254}$$

Therefore, Equation 253 becomes

$$w = 0.351\ \rho_{Zr}\ (R_o - r). \tag{255}$$

The kinetic parameter w can then be converted into an effective ZrO_2 layer thickness:

$$w \frac{dw}{dt} = - C (R_o - r) \frac{dr}{dt} \quad (256)$$

where $C = (0.351 \rho_{Zr})^2$.

Substituting Equation 256 into Equation 250 produces a rate equation for the reacting surface radius:

$$- C (R_o - r) \frac{dr}{dt} = Ae^{(-B/T)} \quad (257)$$

This equation can be integrated between the limits of the old and new time values for r and t to yield an expression for the instantaneous reacting surface radius:

$$r^{n+1} = R_o - [(R_o - r^n)^2 + \frac{2A}{C} e^{-B/T} \Delta T] \quad (258)$$

The linear heat generation rate can then be given as

$$q' = 6.45 \times 10^6 * \pi \rho_{Zr} (r_n^2 - r_{n+1}^2)/\Delta t \quad (259)$$

where 6.45×10^6 J/kg is the energy released per kilogram of oxidized zirconium, assuming a one-region cladding. The density of zirconium is 6490 kg/m^3. Therefore, the above equation reduces to

$$q' = 1.2706 \times 10^{10} (r_n^2 - r_{n+1}^2)/\Delta t \frac{Btu}{hr-ft} \quad (260)$$

The mass ratio of hydrogen generated per unit mass of zirconium oxidized is, $m_{fH2} = 0.0442$. Therefore, the rate of hydrogen mass generated from the reaction is

$$\dot{m}_{H2} = 0.0442 * \pi\rho_{Zr} (r_n^2 - r_{n+1}^2)\Delta x/\Delta t \quad (261)$$

or

$$\dot{m}_{H2} = 56.26 [r_n^2 - r_{n+1}^2] \Delta x/\Delta t \ (\frac{lbm}{sec}) \quad (262)$$

Similarly, the mass ratio of steam consumed per unit mass of zirconium oxidized is $m_f = 0.395$. Therefore, the rate of steam mass consumed in the reaction is

$$\dot{m}_{H_2O} = - 502.1 [r_n^2 - r_{n+1}^2] \Delta x/\Delta t \ (\frac{lbm}{sec}) \quad (263)$$

Equations 260, 262, and 263 have been implemented into COBRA-NC to calculate the oxidation heat rate, hydrogen mass source, and steam mass sink, respectively. Appropriate limits have been placed on the above equations to account for the depletion of steam and zircaloy. The same equations are valid for the Baker-Just model; only the value of the constant coefficients change.

The parameter ratios 2A/C in Equation 258 is defined as AOX in the code and the parameter B as BOX. These coefficients have the following values.

For the Cathcart model,

$$AOX = 7.02 \times 10^{-5} \ (ft^2/sec) \quad T < 1853.0 \ K$$

$$= 2.251 \times 10^{-5} \ (ft^2/sec) \quad T \geq 1853.0 \ K$$

$$BOX = 20070.0 \ (K) \quad T < 1853.0 \ K$$

$$= 16610.0 \ (K) \quad T \geq 1853.0 \ K.$$

For the Baker-Just model,

$$AOX = 8.59 \times 10^{-4} \ (ft^2/sec)$$

$$BOX = 22900 \ (K).$$

REFERENCES

1. D. R. Liles et al. TRAC-PD2, An Advanced Best-Estimate Computer Program for Pressurized Water Reactor Loss-of-Coolant Accident Analysis, NUREG/CR-2054, U. S. Nuclear Regulatory Commission, Washington, D.C., 1981.

2. M. Ishii, Thermo-Field Dynamic Theory of Two-Phase Flow, Eyrolles. 1975.

3. C. W. Stewart, C. L. Wheeler, R. J. Cena, C. A. McMonagle, J. M. Cuta, and D. S. Trent, COBRA- IV: The Model and the Method, BNWL-2214, Pacific Northwest Laboratory, Richland, Washington, 1977.

4. D. R. Liles, Vessel Constitutive Package and Flow Regime Map, LA-NUREG-6924-PR, Los Alamos Scientific Laboratory, Los Alamos, New Mexico, August 1977.

5. S. LeKach, Development of a Computer Code for Thermal Hydraulics of Reactors (THOR), BNL-19978, Brookhaven National Laboratory, Long Island, New York.

6. A. E. Dukler, Flow Regime Transitions for Vertical Upward Gas Liquid Flow: A Preliminary Approach Through Physical Modeling, NUREG/CR-0162, U. S. Nuclear Regulatory Commission, Washington, D.C., January 1977.

7. T. W. Lovell, The Effect of Scale on Two-Phase Countercurrent Flow Flooding in Vertical Tubes, Masters Thesis, Thayer School of Engineering, Dartmouth College, 1977.

8. A. E. Dukler and L. Smith, Two-Phase Interactions in Countercurrent Flow Studies of the Flooding Mechanism, NUREG/CR-0617, U. S. Nuclear Regulatory Commission, Washington, D.C., January 1979.

9. M. Ishii," Drift Flux Model and Constitutive Equations for Relative Motion Between Phases in Various Two-Phase Flow Regimes," ANL-77-47, Argonne National Laboratory, Argonne, Illinois, October 1977.

10. P. N. Rowe, K. T. Claxton, and J. B. Lewis, "Heat Transfer from a Single Sphere in an Extensive Flowing Fluid," Transaction of the Institute of Chemical Engineers, 43, T14-T31, 1965.

11. Andersen, Jens G. Munthe, "Heat Transfer in a Spherical Droplet," REMI/HEAT COOL, A Model for Evaluation of Core Heat-up and Emergency Core Spray Cooling System Performance for Light-Water Cooled Nuclear Power Reactors, Report No. 296, RISO National Laboratory, Denmark, September 1973.

12. D. Moalem and S. Sideman, "The Effect of Motion on Bubble Collapse," International Journal of Heat and Mass Transfer, 16, 2331-2329, 1973.

13. G. A. Hughmark, "Film Thickness, Entrainment, and Pressure Drop in Upward Annular and Dispersed Flow," AIChE Journal, 14, 1062 1973.

14. G. B. Wallis, "Annular Two-Phase Flow, Part I: Simple Theory," Journal of Basic Engineering (March 1970).

15. F. W. Dittus and L. M. K. Boelter, University of California Engineering Publications, 2, 443, 1930.

16. P. Ihle, "Flooding Experiments in Blocked Arrays," paper presented at the Eighth Water Reactor Safety Research Information Meeting, Gaithersburg, Maryland, October 1980.

17. W. H. Henstock and T. J. Hanratty, "The Interfacial Drag and the Height of the Wall Layer in Annular Flows," AIChE Journal, 22 (6), 990-1000 November 1976.

18. D. A. Drew and R. T. Lahey, Jr., "Application of General Constitutive Principles to the Derivation of Multidimensional Two-Phase Flow Equations," International Journal of Multiphase Flow, 1979.

19. G. F. Hewitt and N. S. Hall-Taylor, Annular Two-Phase Flow, Pergamon Press, Oxford, Great Britian, 1970.

20. D. E. Woodmansee and T. J. Hanratty, "Mechanism for the Removal of Droplets from a Liquid Surface by a Parallel Air Flow," 24, 299-307, 1969.

21. M. Ishii and M. A. Grolmes, "Inception Criteria for Droplet Entrainment in Two-Phase Concurrent Film Flow," AIChE Journal, 21(2), 308, 1975.

22. P. B. Whalley, G. F. Hewitt, and P. Hutchinson, Experimental Wave and Entrainment Measurements in Vertical Annular Two- Phase Flow, AERE-R7521, Atomic Energy Research Establishment, Harwell, England, 1973.

23. J. Wurtz, An Experimental and Theoretical Investigation of Annular Steam-Water Flow in Tubes and Annuli at 30 to 90 Bar, Report No. 372, RISO National Laboratory, Denmark, April 1978.

24. I. I. Paleev and B. S. Filippovich, "Phenomena of Liquid Transfer in Two-Phase Dispersed Annular Flow," International Journal Heat Mass Transfer, 9, 1089-1093, 1966.

25. D. F. Tatterson and others, "Drop Sizes in Annular Gas-Liquid Flows," AIChE Journal, 23, (1), 68-76, January 1977.

26. L. B. Cousins, W. H. Denton, and G. F. Hewitt, "Liquid Mass Transfer in Annular Two-Phase Flow," Paper C4 presented at the Symposium on Two-Phase Flow Volume 2, Exeter, England, June 1965, pp. 401- 430.

27. P. B. Whalley, "The Calculation of Dryout in a Rod Bundle," International Journal of Multiphase Flow, 13, 501-515 1977.

28. NRC Steam Generator Workshop, Silver Spring, Maryland, April 1979.

29. J. C. Dallman and W. L. Kirchner, De-Entrainment Phenomena on Vertical Tubes in Droplet Cross Flow, NUREG/CR-1421, U. S. Nuclear Regulatory Commission, Washington, D. C., April 1980.

30. R. C. Hendricks et al., WASP - Flexible FORTRAN IV Computer Code for Calculating Water and Steam Properties, NASA TND-7391, Lewis Research Center, Cleveland, Ohio, 1973.

31. ASME Steam Tables, 1967, 2nd ed., American Society of Mechanical Engineers, New York, 1968.

32. J. H. McFadden et al. "RETRAN-02 A Program for Transient Thermal-Hydraulic Analysis of Complex Fluid Flow Systems, Volume 1: Equations and Numbers, NP-1850, Electric Power Research Institute, Palo Alto, California, May 1980.

33. J. H. Keenan and F. G. Keyes, Thermodynamic Properties of Steam, New York, John Wiley & Sons, 1936.

34. R. B. McClintock and G. J. Silvestri, Formulations and Iterative Procedures for the Calculation of Properties of Steam, American Society of Mechanical Engineers, New York, 1936.

35. C. W. Stewart et al., VIPRE-01 A Thermal-Hydraulics Analysis Code for Reactor Cores: Volume 1, Mathematical Modeling," NP-2511, Electric Power Research Institute, Palo Alto, California, December 1982.

36. J. A. Dearien et al., FRAP-S3: A Computer Code for the Steady-State Analysis of Oxide Fuel Rods-- Report I, Analytical Models and Input Manual, TFBP-TR-164, Idaho National Engineering Laboratory, Idaho Falls, Idaho, October 1977.

37. C. E. Beyer et al., GAPCON-THERMAL-2: A Computer Program for Calculating the Thermal Behavior of an Oxide Fuel Rod, BNWL-1898, Pacific Northwest Laboratory, Richland, Washington, November 1975.

38. D. L. Hagrman, G. A. Reymann, and R. E. Manson, MATPRO-Version 11 (Revision 1): A Handbook of Materials Properties for Use in the Analysis of Light Water Reactor Fuel Rod Behavior, NUREG/CR-0497, U. S. Nuclear Regulatory Commission, Washington, D. C., TREE-1290, Revision 1, February 1980.

39. D. D. Lanning et al. GAPCON-THERMAL-3 Code Description. PNL-2434, Pacific Northwest Laboratory, Richland, Washington.

40. L. J. Siefken et al., FRAP-T5: A Computer Code for Transient Analysis of Oxide Fuel Rods, NUREG/CR-0840, TREE-1281, U. S. Nuclear Regulatory Commission, Washington, D. C., June 1979.

41. G. A. Berna et al., FRAPCON-1: A Computer Code for the Steady-State Analysis of Oxide Fuel Rods, CDAP-TR-032-R1, Idaho National Engineering Laboratory, Idaho Falls, Idaho, November 1978.

42. C. L. Wheeler et al., COBRA-IV-I: An Interim Version of COBRA for Thermal-Hydraulic Analysis of Rod Bundle Nuclear Fuel Elements and Cores, BNWL-1962, Pacific Northwest Laboratory, Richland, Washington, March 1973.

43. D. S. Trent and J. R. Welty, "A Summary of Numerical Methods for Solving Transient Heat Conduction Problems," Bulletin No. 49, Engineering Experimental Station, Oregon State University, Corvallis, Oregon, 1974.

44. W. H. McAdams, Heat Transfer, McGraw-Hill, p. 378, New York, 1954.

45. E. M. Sparrow, A. L. Loeffler, and H. A. Hubbard, "Heat Transfer to Longitudinal Laminar Flow Between Cylinders," Journal of Heat Transfer, 83, 415, 1961.

46. J. C. Chen, "A Correlation for Boiling Heat Transfer to Saturated Fluids in Convective Flow," ASME 63-HT-34, American Society of Mechanical Engineers, 1963.

47. J. G. Collier, Convective Boiling and Condensation, McGraw-Hill Book Co., England, 1972.

48. F. D. Moles and J. F. G. Shaw, "Boiling Heat Transfer to Subcooled Liquids Under Conditions of Forced Convection," Transactions of the Institute of Chemical Engineers, 50, 1972.

49. W. T. Hancox and W. B. Nicoll, "A General Technique for the Prediction of Void Distributions in Non-Steady Two-Phased Forced Convection," International Journal of Heat and Mass Transfer, 14, 1971.

50. S. Z. Rouhani and E. Axelsson, "Calculation of Void Volume Fraction in Subcooled and Quality Boiling Regions," International Journal of Heat and Mass Transfer, 13, 1970.

51. C. W. Stewart et al., Improvements to the COBRA-TF(EPRI) Computer Code for Steam Generator Analysis, NP-1509, Electric Power Research Institute, Palo Alto, California, September 1980.

52. M. J. Thurgood et al., "COBRA-TF Development," paper presented at the Eighth Water Reactor Safety Information Meeting, Gaithersburg, Maryland, October 1980.

53. N. Zuber et al., "The Hydrodynamics Crisis in Pool Boiling of Saturated and Subcooled Liquids," International Developments in Heat Transfer. Part II, No. 27, p. 23-236. International Heat Transfer Conference, Boulder, Colorado, 1961.

54. L. Biasi et al., "Studies on Burnout, Part 3," Energia Nucleare, 14 (9), 530-536, 1967.

55. P. B. Whalley, P. Hutchinson, and G. F. Hewitt, The Calculation of Critical Heat Flux in Forced Convection Boiling, AERE-R7520, Atomic Energy Research Establishment, Harwell, England, 1973.

56. P. B. Whalley, The Calculation of Dryout in a Rod Bundle," AERE-R8319, Atomic Energy Research Establishment, Harwell, England, April 1976.

57. A. W. Bennett et al., Heat Transfer to Steam-Water Mixtures Flowing in Uniformly Heated Tubes in Which the Critical Heat Flux has been Exceeded, AERE- R5373, Atomic Energy Research Establishment, Harwell, England, 1967.

58. R. E. Henry, "A Correlation for the Minimum Film Boiling Temperature," AIChE Symposium Series, 70 (138), 81-90, 1974.

59. R. P. Forslund and W. M. Rohsenow, "Dispersed Flow Film Boiling," Journal of Heat Transfer, 90 (6), 399-407, 1968.

60. K. H. Sun et al., "Calculations of Combined Radiation and Convection Heat Transfer in Rod Bundles Under Emergency Cooling Conditions," ASME 75-HT-64, American Society of Mechanical Engineers, New York, 1975.

61. L. A. Bromley, "Heat Transfer in Stable Film Boiling," Chemical Engineering Progress, 46 (5), 221-226, 1950.

62. J. M. Kelly, "Quench Front Modeling and Reflood Heat Transfer in COBRA-TF," 79-WA/HT-63, ASME Winter Annual Meeting, New York, New York, 1979.

63. Idaho National Engineering Laboratory. RELAP4/MOD6: A Computer Program for Transient Thermal-Hydraulic Analysis of Nuclear Reactors and Related Systems, PG-R-77-06, Idaho Falls, Idaho, March 1977.

64. D. D. Lanning and C. R. Hann, Review of Methods Applicable to the Calculation of Gap Conductance in Zircaloy-Clad UO_2 Fuel Rods, BNWL-1894, Pacific Northwest Laboratory, Richland, Washington, April 1975.

65. W. R. Lloyd et al., "Heat Transfer in Multicomponent Monatomic Gases in the Low, Intermediate, and High Pressure Regime," paper presented at the Nuclear Thermionics Conference, 1973.

66. A. Ullman, R. Acharya, and D. R. Olander, "Thermal Accommodation Coefficients of Inert Gases on Stainless Steel and UO_2," Journal of Nuclear Materials, 51, 277-279, 1974.

67. L. B. Thomas, Fundamentals of Gas-Surfacing Interactions, pp. 346-369, H. Saltsburg et al., eds., New York, Academic Press, 1967.

68. C. R. Hann, C. E. Beyer, and L. J. Parchen, GAPCON-THERMAL-1: A Computer Program for Calculating the Gap Conductance in Oxide Fuel Pins, BNWL-1778, Pacific Northwest Laboratory, Richland, Washington, September 1973.

69. M. G. Cooper, B. B. Mikic, and M. M. Yavonovich, "Thermal Contact Conductance," Journal of Heat and Mass Transfer, 12, 1969.

70. N. Todreas and G. Jacobs, "Thermal Contact Conductance of Reactor Fuel Elements," Nuclear Science and Engineering, 50, 283, 1973.

71. J. E. Garnier and S. Begej, Ex-Reactor Determination of Thermal Gap and Contact Conductance Between Uranium Dioxide: Zircaloy Interfaces. Stage 1: Low Gas Pressure, NUREG/CR-0330, U. S. Nuclear Regulatory Commission, Washington, D. C., April 1979.

72. G. A. Berna et al. FRAPCON-2: A Computer Code for the Calculation of Steady-state Thermal-Mechanical Behavior of Oxide Fuel Rods, NUREG/CR-1845, U. S. Nuclear Regulatory Commission, Washington, D. C., January 1981.

73. D. R. Coleman and E. T. Laats, FRAP-T3, A Computer Code for the Transient Analysis of Oxide Fuel Rods - Model Assessment Report, NUREG/CR-0555, TREE-1320, U. S. Nuclear Regulatory Commission, Washington, D. C., February 1979.

74. T. A. Bjornard and P. Griffith, "PWR Blowdown Heat Transfer," Thermal and Hydraulic Aspects of Nuclear Reactor Safety, American Society of Mechanical Engineers, New York, Vol. 1, p 17-41, 1977.

75. V. P. Isachenko, "Heat Transfer in Condensation in Turbulent Jets," Teploenergetika, No. 2, pp. 7-10 (1976).

76. J. O. Hirschfelder, R. B. Bird, and E. L. Spotz, "The Transport Properties of Nonpolar Gases," J. Chem. Phys., 16, 968, 1948.

77. R. Bird, W. E. Stewart, and E. N. Lightfoot, Transport Phenomena, John Wiley & Sons, Inc., New York, 1960.

78. R. A. Shehla, Estimated Viscosities and Thermal Conductivites of Bases at High Temperatures, NASA Technical Report R-132, Lewis Research Center, 1962.

79. J. O. Hirshfelder, C. F. Curtiss, and R. B. Bird, Molecular Theory of Gases and Liquids, John Wiley & Sons, Inc., New York, 1954.

80. R. S. Brokaw, "Energy Transport in High Temperature and Reacting Gases", Air Force Office Scientific Research - General Electric Co., Conf. Phys. Chem. in Aerodynamics and Space Flight, Philadelphia, September 1- 3, 1959.

81. C. R. Wilke, "A Viscosity Equation for Gas Mixtures", J. Chem. Phys., 18, 517, 1950.

82. R. S. Brokaw, "Approximate Formulas for the Viscosity and Thermal Conductivity of Gas Mixtures," J. Chem. Phys., 29, 391, 1958.

83. J. O. Hirchfelder, Proc. Joint Conf. Thermodynamic and Transport Properties of Fluids, the Inst. Mech. Eng. (London), p. 133, 1958.

84. H. A. Uchida, A. Oyama, and Y. Togo, 1964. Evaluation of Post-Incident Cooling Systems of Light Water Power Reactors. 3rd Int. Conf. on Peaceful Uses of Atomic Energy. Vol. 13, p. 93.

85. Y. S. Touloukin and C. Y. Ho, 1970. Thermal Physical Properties of Matter, Thermophysical Properties Research Center (TPRL), Purdue University, Lafayette, Indiana.

NUREG/CR-3262
PNL-5515
Vol. 1
R4

DISTRIBUTION

No. of
Copies

OFFSITE

U. S. Nuclear Regulatory
Commission
Division of Technical
Information and Document
Control
7920 Norfolk Avenue
Bethesda, MD 20014

20 Tim Lee
Analytical Model Branch
Office of Nuclear Regulatory
Research
U. S. Nuclear Regulatory
Commission
7915 Eastern Avenue
MS-1130-SS
Washington, DC 20555

No. of
Copies

ONSITE

50 Pacific Northwest Laboratory

CL Wheeler (43)
Publishing Coordination (2)
Technical Information (5)

NRC FORM 335 (11-81)

U.S. NUCLEAR REGULATORY COMMISSION

BIBLIOGRAPHIC DATA SHEET

1. REPORT NUMBER (Assigned by DDC)
NUREG/CR-3262, Vol. 1
PNL-4718

4. TITLE AND SUBTITLE (Add Volume No., if appropriate)
COBRA-NC: A Thermal-Hydraulic Code for Transient Analysis of Nuclear Reactor Components
Volume 1: Equations and Constitutive Models

2. (Leave blank)

3. RECIPIENT'S ACCESSION NO.

7. AUTHOR(S)
C.L. Wheeler, M.J. Thurgood, T.E. Guidotti, D.E. DeBellis

5. DATE REPORT COMPLETED
MONTH: March | YEAR: 1986

9. PERFORMING ORGANIZATION NAME AND MAILING ADDRESS (Include Zip Code)
Pacific Northwest Laboratory
P.O. Box 999
Richland, WA 99352

DATE REPORT ISSUED
MONTH: May | YEAR: 1986

6. (Leave blank)

8. (Leave blank)

12. SPONSORING ORGANIZATION NAME AND MAILING ADDRESS (Include Zip Code)
Division of Accident Evaluation
Office of Nuclear Regulatory Research
U.S. Nuclear Regulatory Commission
Washington, DC 20555

10. PROJECT/TASK/WORK UNIT NO.

11. FIN NO.
B2466

13. TYPE OF REPORT
Technical

PERIOD COVERED (Inclusive dates)

15. SUPPLEMENTARY NOTES

14. (Leave blank)

16. ABSTRACT (200 words or less)

COBRA-NC is a digital computer program written in FORTRAN IV that simulates the response of nuclear reactor components and systems to thermal-hydraulic transients. The code solves the multicomponent, compressible, three-dimensional, two-fluid, three-field equations for two-phase flow. The three velocity fields are the vapor/gas field, the continuous liquid field, and the liquid drop field. The code has been used to model flow and heat transfer within the reactor core, the reactor vessel, the steam generators, and in the nuclear containment. The conservation equations, equations of state, and physical models that are common to all applications are presented in this volume of the code documentation.

17. KEY WORDS AND DOCUMENT ANALYSIS

17a. DESCRIPTORS

COBRA-NC computer code

17b. IDENTIFIERS/OPEN-ENDED TERMS

18. AVAILABILITY STATEMENT
Unlimited

19. SECURITY CLASS (This report)
Unclassified

21. NO. OF PAGES

20. SECURITY CLASS (This page)
Unclassified

22. PRICE
$

NRC FORM 335 (11-81)

NUCLEAR REACTOR COMPONENTS